

## INFORMATION TO USERS

This manuscript has been reproduced from the microfilm master. UMI films the text directly from the original or copy submitted. Thus, some thesis and dissertation copies are in typewriter face, while others may be from any type of computer printer.

**The quality of this reproduction is dependent upon the quality of the copy submitted.** Broken or indistinct print, colored or poor quality illustrations and photographs, print bleedthrough, substandard margins, and improper alignment can adversely affect reproduction.

In the unlikely event that the author did not send UMI a complete manuscript and there are missing pages, these will be noted. Also, if unauthorized copyright material had to be removed, a note will indicate the deletion.

Oversize materials (e.g., maps, drawings, charts) are reproduced by sectioning the original, beginning at the upper left-hand corner and continuing from left to right in equal sections with small overlaps. Each original is also photographed in one exposure and is included in reduced form at the back of the book.

Photographs included in the original manuscript have been reproduced xerographically in this copy. Higher quality 6" x 9" black and white photographic prints are available for any photographs or illustrations appearing in this copy for an additional charge. Contact UMI directly to order.

# UMI

A Bell & Howell Information Company  
300 North Zeeb Road, Ann Arbor MI 48106-1346 USA  
313/761-4700 800/521-0600



University of Alberta

**Shear Alfvén Waves and Shear Flow Instabilities  
in the Earth's Magnetosphere**

By  
Igor Voronkov



A dissertation  
presented to the Faculty of Graduate Studies and Research  
in partial fulfilment of the requirements for the degree  
of

Doctor of Philosophy

Department of Physics

Edmonton, Alberta

Fall 1998



National Library  
of Canada

Acquisitions and  
Bibliographic Services

395 Wellington Street  
Ottawa ON K1A 0N4  
Canada

Bibliothèque nationale  
du Canada

Acquisitions et  
services bibliographiques

395, rue Wellington  
Ottawa ON K1A 0N4  
Canada

*Your file Votre référence*

*Our file Notre référence*

The author has granted a non-exclusive licence allowing the National Library of Canada to reproduce, loan, distribute or sell copies of this thesis in microform, paper or electronic formats.

The author retains ownership of the copyright in this thesis. Neither the thesis nor substantial extracts from it may be printed or otherwise reproduced without the author's permission.

L'auteur a accordé une licence non exclusive permettant à la Bibliothèque nationale du Canada de reproduire, prêter, distribuer ou vendre des copies de cette thèse sous la forme de microfiche/film, de reproduction sur papier ou sur format électronique.

L'auteur conserve la propriété du droit d'auteur qui protège cette thèse. Ni la thèse ni des extraits substantiels de celle-ci ne doivent être imprimés ou autrement reproduits sans son autorisation.

0-612-34851-2

UNIVERSITY OF ALBERTA  
LIBRARY RELEASE FORM

NAME OF AUTHOR: Igor Voronkov  
TITLE OF THESIS: Shear Alfvén Waves and  
Shear Flow Instabilities  
in the Earth's Magnetosphere  
DEGREE: Doctor of Philosophy  
YEAR THE DEGREE GRANTED: 1998

Permission is hereby granted to the University of Alberta library to reproduce single copies of this thesis and to lend such copies for private, scholarly or scientific research purposes only.

The author reserves other publication rights, and neither the thesis or extensive extracts from it may be printed or otherwise reproduced without the author's written permission.




Igor Voronkov  
Department of Physics  
University of Alberta  
Edmonton, Alberta  
T6G 2J1

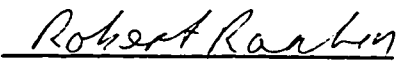
Date: *Aug 14, 1998*

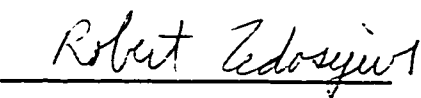
UNIVERSITY OF ALBERTA

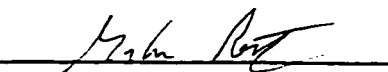
FACULTY OF GRADUATE STUDIES AND RESEARCH


The undersigned certify that they have read, and recommend to the Faculty of Graduate Studies and Research for acceptance, a thesis entitled "Shear Alfvén Waves and Shear Flow Instabilities in the Earth's Magnetosphere" submitted by Igor Voronkov in partial fulfilment of the requirements for the degree of Doctor of Philosophy.

  
Dr. J. C. Samson , Supervisor

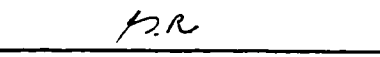
  
Dr. R. Rankin , Supervisor

  
Dr. R. Fedosejevs

  
Dr. G. Rostoker

  
Dr. R. Sydora

Date: May, 8, 1998

  
Dr. L. R. Lyons

# Abstract

The objective of this thesis is the theoretical and computational study of nonlinear shear Alfvén waves and shear flow instabilities in the Earth's magnetosphere. We have developed a computer code to solve the nonlinear set of magnetohydrodynamic (MHD) equations in curvilinear coordinates. This code has been used to simulate the excitation, growth, coupling of shear Alfvén waves and magneto-acoustic modes, and nonlinear saturation of standing shear Alfvén waves in the dipolar magnetosphere. The computational results were verified by comparing them with a nonlinear analytical model which was derived as part of this study.

Using computer simulations, we have shown that shear Alfvén waves in the field line resonance region develop into an azimuthally stretched and radially confined region of a large amplitude shear flow in the equatorial magnetosphere. This shear flow may become unstable with respect to a shear flow instability with characteristic  $e$ -folding time smaller than a half-period of the shear Alfvén wave. Therefore, we have used the computer model to study shear flow and shear flow ballooning instabilities which can arise in the association with field line resonance regions.

Initially, we used the MHD code to model the shear flow and ballooning instabilities in the equatorial plane of the Earth's magnetosphere. We have shown that a shear flow vortex couples effectively with a ballooning mode and grows with a characteristic time scale of tens of seconds extracting the potential energy from the ambient magnetic configuration. Therefore, the instability results in the generation and propagation of a large scale vortex structure which appears to be in agreement with observed scales of the vortices seen in auroral arcs.

Finally, the study of shear flow and ballooning instabilities was accomplished using a three-dimensional computer model. We discuss the structure of vortices,

magnetic field, and field-aligned currents obtained from the three-dimensional computer simulations and conclude that these instabilities may lead to vortices associated with discrete auroral arcs.



## Acknowledgements

I am grateful to my supervisors, Dr. John Samson and Dr. Robert Rankin for their support and assistance during the course of this research. They provided me with a unique opportunity to complete this project using sophisticated supercomputers which has given me great experience in both computational physics and programming. The project they suggested to me lays in the most controversial area of modern space physics which encouraged me to come up to speed on the newest ideas of the topic. I would also like to thank Dr. Gordon Rostoker who has supported my academic career.

I extend my thanks to all other committee members, Dr. Robert Fedosejevs, Dr. Rick Sydora, and my external examiner, Dr. Larry Lyons for their detailed examination of my thesis and useful comments.

All my friends and colleagues in the Space Physics Laboratory have made the past 5 years both pleasant and productive. I am highly grateful to Susan Skone, Francis Fenrich, Anna Belehaki, Christine Lesiak, Erena Friedrich, Sarah Derr, Karen Apps, Beth Tooley, Eric Donovan, Martin Connors, Colin Waters, Nozomu Nishitani, Przemek Frycz, Jean-Pierre DeVilliers, Sherwood Botsford, James MacKinnon, Hamid Al Nashi, Rafal Dymarz, Peter Damiano, Terry Kolber, Barry Harrold, William Liu, Sandy MacAuley, Vladimir Tikhonchuk, Ian Mann, James Wanliss, and Henry Sikkema. I give my special thanks to Vladimir and Przemek who challenged me to overcome my indolence with respect to analytics and to learn some scholar methods of solving problems. I also give my special thanks to the lab secretary, Sarah Derr and the graduate student secretary, Lynn Chandler for their invaluable help with all things.

My life in Edmonton has been exceedingly enriched by the people from my

home country. Igor Kolodkin, Yuri Leontiev, Marina Blekher, Oleg Verevka, Vika Lohvin, Yuri Novikov, Ilya Vodopianov, Valeria Dorokhova, and many others have helped me a great deal to overcome the threshold of living in a different country. I also would like to give my warmest thanks and wishes to my friends overseas: Misha Goodkov, Kiril Orlov, Dima Drachev, and Olya Glazova for their never ending friendship.

The completion of this work could hardly have been a success if I had not met the people whom I would dare to call my teachers in science. I express my gratitude to Dr. M. I. Pudovkin, Dr. N. A. Tsyganenko, Dr. V. A. Sergeev, Dr. A. M. Lyatskaya, Dr. I. V. Golovchanskaya, Dr. B. M. Kuznetsov, Dr. A. V. Shirochkov, and Dr. O. M. Troshichev. I give my special thanks to Dr. Oleg Troshichev who encouraged me to attempt studying abroad. I also take this opportunity to express my warmest thanks to all my colleagues from the Arctic and Antarctic Institute for all the wonderful memories.

My mother Alexandra, my father Oleg, my brother Vova, and my aunts, Tatyana and Natalia have always supported and encouraged me. I must particularly thank my daughter, Olga whose questions like 'have you got an idea why you had this noise instead of a wave?' have urged me to try again.

I acknowledge the University of Alberta and the Natural Sciences and Engineering Research Council of Canada for providing my financial support.

# Contents

**Abstract**

**Acknowledgements**

**Contents**

**List of Figures**

<b>1</b>	<b>Introduction</b>	<b>1</b>
1.1	Preamble . . . . .	1
1.2	Historical Remarks . . . . .	2
1.3	Essentials of Space Plasma Physics . . . . .	5
1.3.1	Basic definitions . . . . .	5
1.3.2	Magnetohydrodynamic Equations . . . . .	6
1.3.3	MHD Waves . . . . .	10
1.3.4	MHD theory of Field Line Resonances . . . . .	14
1.3.5	Shear Flow and Ballooning Instabilities . . . . .	16
1.4	Magnetosphere of the Earth . . . . .	22
1.4.1	Main Regions of the Earth's Magnetosphere . . . . .	22
1.4.2	Ionosphere . . . . .	27

1.4.3	Large-Scale Field Aligned Currents . . . . .	30
1.4.4	Magnetospheric Substorms . . . . .	31
1.4.5	Field Line Resonances in the Earth's Magnetosphere . . . . .	36
1.4.6	Auroral Arcs . . . . .	39
1.5	Thesis Outline . . . . .	42
<b>2</b>	<b>Alternative Direction Implicit (ADI) Method for MHD Equations</b>	<b>44</b>
2.1	MHD Equations in Curvilinear Coordinates . . . . .	44
2.2	Alternative Direction Implicit (ADI) Numerical Method for MHD Partial Differential Equations . . . . .	48
2.3	Boundary Conditions . . . . .	52
2.4	Numerical Diffusion . . . . .	53
2.5	ADI Code in Parallel and Vector Computers . . . . .	54
<b>3</b>	<b>Shear Alfvén Waves and Field Line Resonances in the Dipolar Mag- netosphere</b>	<b>58</b>
3.1	Preliminary Remarks . . . . .	58
3.2	Dipolar Model of the Earth's Magnetosphere . . . . .	61
3.2.1	Dipolar Coordinates . . . . .	62
3.2.2	Representation of the Earth's Dipolar Magnetic Field in the Dipolar Coordinates . . . . .	64
3.2.3	Equilibrium of the Dipolar Magnetosphere . . . . .	66

3.3	Linear Shear Alfvén Waves in the Dipolar Magnetosphere . . . . .	67
3.3.1	Dispersion Relation for Linear SAWs . . . . .	67
3.3.2	Eigenproblem for a Standing SAW in the Dipolar Magnetosphere	69
3.4	Nonlinear Model of Field Line Resonances in a Dipolar Field . . . . .	74
3.4.1	Nonlinear Model of FLRs . . . . .	74
3.4.2	Linear Growth of SAWs . . . . .	75
3.4.3	Slow Magnetosonic Wave Response . . . . .	76
3.4.4	Numerical Solution and Analysis . . . . .	79
3.5	Three Dimensional Evolution of SAWs . . . . .	85
3.6	Discussion . . . . .	91
<b>4</b>	<b>Shear Flow and Shear Flow Ballooning Instabilities in the Equato- rial Plane of the Earth's Magnetosphere</b>	<b>94</b>
4.1	Preliminary Remarks . . . . .	94
4.2	Theoretical Model . . . . .	97
4.2.1	Basic Equations . . . . .	97
4.2.2	Qualitative Analysis of the Hybrid Mode Instability . . . . .	100
4.2.3	Linear Theory of the Hybrid Instability . . . . .	102
4.3	Numerical Results . . . . .	106
4.3.1	Vortex Evolution . . . . .	106

4.3.2	Wavelength Dependence . . . . .	116
4.3.3	Bi-directional (Antisymmetric) Flow . . . . .	117
4.4	Validity of the “Effective Gravity” Approach and Energy Balance in the System . . . . .	120
4.5	Discussion . . . . .	123
<b>5</b>	<b>Three Dimensional Evolution of Shear Flow and Ballooning Vor- tices</b>	<b>129</b>
5.1	Introductory Remarks . . . . .	129
5.2	Shear Flow Instability in the Dipolar Magnetosphere . . . . .	132
5.3	3D Ballooning Instability in the Plasma Sheet . . . . .	148
5.3.1	The Ballooning Equilibrium Problem . . . . .	148
5.3.2	Ballooning Instability . . . . .	149
5.4	Summary . . . . .	156
<b>6</b>	<b>Conclusions</b>	<b>159</b>
	<b>Bibliography</b>	<b>164</b>

## List of Figures

1.1	The phase (a) and group (b) velocities of the Alfvén wave (solid line), slow mode (dashed line), and fast mode (dotted line) as a function between the ambient magnetic field and wave vectors. . . . .	12
1.2	Shear Alfvén wave (a) and compressional mode (b). . . . .	13
1.3	Radial ( $x$ ) distribution of normalized $E_x$ component around the FLR point.	15
1.4	Dependence of the growth rate (solid line) and frequency (dashed line) on the wave number for a Gaussian uni-directional flow. . . . .	18
1.5	Schematic of the ballooning instability. . . . .	20
1.6	Dependence of the growth rate of ballooning modes on $k_y$ for different $k_x$ labelled in the plot. . . . .	21
1.7	The 3D diagram of the Earth's magnetosphere from <i>Eastman et al.</i> [1985].	25
1.8	Dependence of the Alfvén wave reflection on the ionospheric conductivity.	29
1.9	Schematic of FLRs in the Earth's magnetosphere. . . . .	38
2.1	The schematic of a computational cell used in ADI. . . . .	50
2.2	A schematic of the parallelization and vectorization of ADI. . . . .	55
2.3	A diagram of the parallelization and vectorization in a FORTRAN ver- sion of ADI. . . . .	56
2.4	The normalized performance time as a function of the number of mesh points in a parallel chunk. . . . .	57

3.1	Magnetic field in the equatorial midnight magnetotail as predicted by the T96 model [Tsyganenko, 1996] (solid line) and dipolar magnetic field of the Earth (dashed line). . . . .	62
3.2	Elements of the dipolar topology. . . . .	63
3.3	An $L$ -shell of the Earth's dipolar magnetic field. . . . .	65
3.4	Variation of the dipolar magnetic field along the $L = 10$ magnetic shell computed from $B_0 = M/h_\mu$ . Here, $Z$ is distance along magnetic field lines from the southern ionosphere to the northern ionosphere . . . .	66
3.5	Distribution of (a) density and (b) Alfvén velocity along the $L = 10$ magnetic field line. . . . .	70
3.6	Distribution of (a) $h_\phi B_\phi$ and (b) $V_\phi$ fields of the first (solid line), second (dashed line), and third (dotted line) SAW modes along the $L = 10$ magnetic field line. $h_\phi B_\phi$ is normalized by the boundary value and $V_\phi$ is normalized by the $V_\phi$ in the equatorial point. . . . .	72
3.7	$L$ -shell dependance of $\omega$ for the first (solid line), second (dashed line), and third (dotted line) SAW modes. . . . .	73
3.8	The growth of the amplitude of the SAW as predicted by the analytical model (solid line) and obtained numerically from the full set of MHD equations using the ADI code (dashed line). $\beta$ is $2.65 \cdot 10^{-2}$ in the equatorial plane. . . . .	80
3.9	The evolution of the SAW amplitude (a) and phase (b) for $\beta = 2.65 \cdot 10^{-4}$ (solid line); $2.65 \cdot 10^{-3}$ (dashed line); $2.65 \cdot 10^{-2}$ (dotted line) and 0.88 (dash-dotted line). . . . .	82



3.10	Normalized spectra of acoustic waves, generated by the FLR at time $T$ (solid line), $4T$ (dashed line), $10T$ (dotted line), and $20T$ (dash-dotted line); $\beta = 2.65 \cdot 10^{-2}$ in the equatorial plane. . . . .	83
3.11	Pressure perturbation distribution along the field line at $t = 30T$ . $\beta = 2.65 \cdot 10^{-2}$ in the equatorial plane. The distance $Z$ along the field line is normalized by the Earth's radius $R_E$ . . . . .	84
3.12	SAW amplitudes as a function of the frequency shift between the driver and SAW at time $5T$ (solid line), $20T$ (dashed line), $35T$ (dotted line). $\beta = 2.65 \cdot 10^{-2}$ in the equatorial plane. . . . .	85
3.13	Radial distribution of the driver velocity in the equatorial plane. . . . .	86
3.14	Radial distribution of the SAW velocity in the equatorial plane for different phases of the SAW. . . . .	87
3.15	Dependence of the KH instability e-folding time on the time of FLR evolution. . . . .	88
3.16	Meridional profile of FACs at the ionospheric level. . . . .	89
3.17	Poleward motion of FACs in the FLR region at the ionosphere level. Here, $r$ is the distance in the meridional direction at the ionospheric level. . . . .	90
3.18	Photometer data for the $6300 \text{ \AA}$ emission associated with a FLR. . . . .	91
4.1	Variations of the azimuthal velocity of a SAW in the equatorial plane for one period. . . . .	95

4.2	A schematic of the inner plasma sheet: a shear flow is embedded in a region of pressure gradient and stretched magnetic field lines. . . . .	98
4.3	A schematic showing the interaction of a shear flow vortex with a pressure gradient cell. A Gaussian shaped shear flow is assumed. . . . .	101
4.4	Growth rate $\gamma = \text{Im}(\omega)\delta/V_0$ of the hybrid mode (solid line), KH instability (dashed line), and noninteractive ballooning mode (dotted line) as a function of $k\delta$ . The growth rates for the hybrid and noninteractive modes are computed for $W^2(\delta/V_0)^2 = -0.01$ . . . . .	104
4.5	A model of the interaction of a shear flow vortex with ballooning modes of different radial scales: (a) $k_x \sim 1/L$ and (b) $k_x \sim 2/L$ . Arrows show the direction of the plasma motion due to the KH vortex (solid arrows) and ballooning cells (empty arrows) formation. . . . .	105
4.6	Growth of (a) amplitude of the radial velocity $V_x$ and (b) the integrated kinetic energy of the hybrid mode (solid line), KH mode (dashed line) and ballooning mode (dotted line), respectively. . . . .	108
4.7	Time slices of the vorticity as obtained from the computer simulations for (a) the hybrid mode and (b) the KH instability, for $t/t_a = 5, 7$ , and 10. . . . .	109
4.8	Linear growth of $V_x$ obtained from the ADI code simulations . . . . .	111
4.9	Contour plots of (a) $V_x$ , (b) density and (c) plasma pressure for $t/t_a = 6$ and 7, respectively, illustrating the transformation of the hybrid eigenmode from KH-like to ballooning-like. . . . .	113

4.10	The vorticity of the hybrid mode for $t/t_a = 10$ , demonstrating the generation of secondary shear flows which elongate the vortices in the direction opposite to the initial shear flow. Three wavelengths are combined in order to show a whole vortex structure. . . . .	114
4.11	Radial distribution of the integrated radial kinetic energy $\langle V_x^2 \rangle$ , at time $t / t_a = 8.8$ (solid line), 9.8 (dashed line), 10.7 (dotted line), and 11.6 (dash-dotted line). . . . .	115
4.12	The vorticity for (a) small ( $k = 1.8/\delta$ ) and (b) large ( $k = 0.2/\delta$ ) wavelength perturbations. . . . .	117
4.13	Time slices of the vorticity obtained from the computer simulations for the hybrid mode driven by a bi-directional shear flow with (a) $k = 1/\delta$ ( $t/t_a = 10.1, 13.1$ ), and (b) $k = 0.5/\delta$ ( $t/t_a = 14.1, 18.2$ ). . . . .	119
4.14	Growth of amplitude of the radial velocity $V_x$ for two models: effective gravity (solid line) and curvature (dashed line). . . . .	122
4.15	(a) Growth of the radial velocity amplitude of the hybrid mode (solid line) and KH mode (dashed line), respectively. (b) Evolution of kinetic energy (solid line), and potential energy due to the work done by the plasma pressure (dashed line), magnetic pressure (dotted line), and magnetic curvature (dash-dotted line) in the system with the hybrid vortex. . . . .	124
4.16	Spatial distribution of the kinetic energy and the velocity field associated with the hybrid vortex at $t/t_a = 14$ . . . . .	125
5.1	Distribution of the azimuthal shear flow velocity. . . . .	134

5.2	Time slices of vorticity in the equatorial plane for $t = 20, 40, 60$ , and $70$ s obtained using (a) 3D and (b) 2D models. . . . .	135
5.3	Growth of the $V_\nu$ amplitude at the equatorial plane as obtained from the 3D (solid line) and 2D (dashed line) models. . . . .	136
5.4	Radial ( $\nu$ ) and azimuthal ( $\phi$ ) distribution of $V_\nu$ at (a) $3.1R_E$ , (b) $8.3R_E$ , and (c) $13.5R_E$ along the field line and (d) a KH eigenmode predicted by the 2D theory. . . . .	137
5.5	Dependence of the growth rate (solid line) and frequency (dashed line) on the coupling coefficient $\alpha$ . The growth rate and frequency are normalized by $\delta/V_0$ . . . . .	139
5.6	Field-aligned distribution of the phase velocity obtained from the 3D simulations (solid lines) and as predicted by the 2D theory (dashed lines). . . . .	140
5.7	Field-aligned ( $\mu$ ) and azimuthal ( $\phi$ ) distribution of (a) $V_\nu$ and (b) $V_\mu$ perturbations (main harmonic) at $t = 10$ s. . . . .	141
5.8	Velocity field distribution in (a) the ionosphere and (b) at $\sim 3R_E$ above the ionosphere at $t = 50$ s. . . . .	141
5.9	Temporal evolution of the $B_{\nu, norm}$ perturbation amplitude as predicted by equation (5.9) for $C_1/C_2 = 30$ (solid line) and $10$ (dashed line). . .	143
5.10	Growth of $[B_\nu]_{MAX}$ at the ionosphere (solid line), $0.5R_E$ (dashed line), and $1R_E$ (dotted line) along the field line. . . . .	144
5.11	Time slices of the field-aligned current distribution at the ionosphere illustrating the formation and dissipation of the fold-like structure. . .	145

5.12	Field-aligned distribution of the $B_\phi$ amplitude at $t=70$ sec (solid line) and the $B_\phi$ eigenfunction of the main SAW harmonic (dashed line).	146
5.13	Temporal evolution of the shear flow in the equatorial plane as obtained from (a) 2D and (b) 3D models.	147
5.14	Initial equilibrium conditions for the 3D simulations of the ballooning instability: (a) $P_{[\nu,\phi]}$ and (b) $B_\mu$ in the equatorial plane, and (c) $P_{[\nu,\phi]}$ and (d) $B_\nu$ in the $\mu, \nu$ plane. Field-aligned coordinate $\mu$ starts at $5R_E$ above the southern hemisphere and ends at $5R_E$ above the northern hemisphere. Coordinate $\nu$ covers the fraction from $L = 8.5$ till $L = 11.5$ . $\phi$ is azimuthal corresponding to 2432 km in the equatorial plane.	150
5.15	Growth of the initial perturbation $V_\nu$ at $7.8R_E$ (solid line), $5.4R_E$ (dashed line), $2.8R_E$ (dotted line), and $0.7R_E$ (dash-dotted line) from the boundary along field lines. $7.8R_E$ corresponds to the equatorial plane.	151
5.16	Evolution of the ballooning cell in the equatorial plane. Time slices correspond to the initial time ( $t = 0$ s), linear stage ( $t = 75$ s), and nonlinear stage ( $t = 100$ s).	153
5.17	Changes of the kinetic energy (dashed line) and the work produced by the magnetic field line curvature force (solid line) in the equatorial region.	154
5.18	Equatorial $B_\mu$ averaged over the azimuthal wavelength as a function of the radial distance at $t = 0$ s (solid line) and $t = 130$ s (dashed line), and dipolar magnetic field (dotted line).	155
5.19	Field-aligned distribution of the amplitudes of the magnetic components (a) $B_\nu$ and (b) $B_\phi$ at $t = 100$ s.	155

# CHAPTER 1

## Introduction

### 1.1 Preamble

In general, Solar-Terrestrial physics deals with processes which couple the solar wind to the geospace environment. Plasma disturbances which originate in the Sun travel with a plasma flow called the solar wind, penetrate the magnetic field of the Earth (the Earth's magnetosphere), and finally affect the near-Earth regions - ionosphere and atmosphere. It is generally accepted that energy from the solar wind can enter the magnetosphere via several major mechanisms - magnetic reconnection, plasma viscous interaction of the solar wind with the magnetospheric boundary, and excitation of magnetohydrodynamic (MHD) waves on the solar wind - magnetosphere boundary. All these mechanisms can initiate large-scale magnetohydrodynamic waves which propagate inside the magnetosphere.

One major problem in Solar-Terrestrial physics is how energy propagates within the magnetosphere and how it is subsequently stored and released into the ionosphere. Observations show that this energy becomes stored in particular magnetospheric regions where strong electric currents and accelerated particles flow along the Earth's magnetic field lines. These field-aligned currents and particles produce strong ionospheric currents and the luminosity which is seen as the aurora.

In this work, we concentrate on the theoretical study of some nonlinear processes which can lead to the energy storage in the magnetosphere and its release into the ionosphere through MHD wave processes, particularly ultra low frequency shear Alfvén waves. One mechanism which allows for energy accumulation at  $\sim 8$ -10 Earth radii ( $R_E$ ) and along magnetic field lines threading the auroral ionosphere, is called a field line resonance (FLR). We study this mechanism in both linear and nonlinear stages using analytical theory and computer simulations. Our results indicate that FLRs produce large field-aligned currents and high amplitude magneto-acoustic waves which may also accelerate particles. This provides the magnetosphere-ionosphere coupling in the FLR region. We consider two distinct nonlinear mechanisms in FLRs: ponderomotive forces and fluid instabilities. An important feature of FLRs is that they initiate large amplitude shear flows which can eventually excite shear flow instabilities. If the shear flow instability is initiated in a region of a strong pressure gradient, it may couple with a ballooning mode. The resulting hybrid mode can cause some of the large scale vortex structuring in auroral arcs.

## 1.2 Historical Remarks

The physics of auroral phenomena originated more than two centuries ago when O. Hiorter, a Swedish scientist-magnetometrist, discovered that perturbations of the Earth's magnetic field registered in the Uppsala observatory correlated with visual auroral activity. His observations implied that auroras were more complex phenomena than had been thought earlier. For example, some theories explained auroras as a result of purely optical reflection of star light, particularly of the bright Milky Way, from the polar ice. It was not until the late nineteenth century when the

Norwegian physicist Kristian Birkeland attempted to explain the phenomenon in terms of strong electrical currents flowing along the Earth's magnetic field lines. Birkeland [1896] showed that these currents were able to produce magnetic perturbations as well as visual luminosity similar to that observed in experiments with vacuum tubes and cathode rays. Birkeland's ideas were strongly supported by his observations made during three polar expeditions and experiments with "terella", the coil system which produced a dipolar magnetic field. Birkeland showed that electrons moved along the field lines and produced luminosity patterns similar to some auroral forms.

In 1881, H. Fritz statistically studied the latitude dependance of auroral activity. He showed that auroral activity has a maximum at approximately  $23^\circ$  equatorward from the pole and decreases both equatorward and poleward from this maximum [Fritz, 1881]. This region of enhanced auroral activity was called the Fritz zone or auroral zone.

In an attempt to explain the occurrence of the Fritz zone, Størmer [1927] constructed a quantitative model of auroras based on the calculations of particle trajectories in a dipolar magnetic field. Størmer's theory showed that electrons entering the Earth's dipolar magnetic field produce a circular precipitation zone at  $2 - 4^\circ$  from the pole whereas helium ions and protons would enter the Earth's atmosphere at  $16 - 19^\circ$  and  $4 - 6^\circ$ , respectively.

Even though the theory by Birkeland and Størmer was in agreement with some optical and magnetic observations and with laboratory experiments, it could not explain several details of the aurora's origin and was based on seemingly contradictory assumptions. Therefore, it instigated numerous debates amongst physicists. Some points of their arguments were:



1. Electrons entering the Earth's magnetic field and initiating auroras were assumed to be released by the Sun during solar flares. It was not clear how an electron beam could hold together against electric repulsion and propagate over these large distances.
2. In order to explain magnetic perturbations, Birkeland suggested that auroral rays are excited by electrons. Størmer's theory predicted a precipitating zone  $2 - 4^\circ$  from the pole whereas observations showed that the Fritz zone lies  $23^\circ$  from the pole. This disagreement could have been resolved if one had assumed that the real Earth's magnetic field diverges from a dipole. However, it was not until the theoretical study by *Chapman and Ferraro* [1931] and after further investigations of the Earth's magnetic field structure [*Gringauz*, 1962; *Fairfield*, 1968] which showed that the magnetic field lines at high latitudes are strongly deviated from a dipolar topology.
3. Even though Birkeland proposed a system of field aligned currents which could explain the observed magnetic variations, the origin of these currents was not clear. Their existence was the subject of vigorous scientific battles up to the seventies, when these currents were finally observed during the spacecraft experiment Triad [*Zmuda and Armstrong*, 1974; *Iijima and Potemra*, 1978].
4. The theory by Birkeland and Størmer was extremely simplified and could not explain the diversity of auroral forms, colors and scales, nor their dependence on local time. These questions required further study of the structure of the magnetic field, properties of the ionized gases (or plasmas), features of the magnetosphere - upper atmosphere interactions, etc. Many of these problems remain still unresolved.

Thus, auroral activity results from diverse physical processes in the chain

“Sun - solar wind - magnetosphere - ionosphere”. All these components of the Solar-Terrestrial interaction manifest different properties, so let us begin with a short description of each of them. Not aiming to cover all topics of Solar-Terrestrial physics, we shall concentrate on the processes which lead to or have an influence on auroral phenomena.

## 1.3 Essentials of Space Plasma Physics

### 1.3.1 Basic definitions

An ensemble of charged particles forms a plasma if it satisfies the requirement of quasineutrality and demonstrates collective properties. In most cases, space plasmas consists of positive ions and electrons which are coupled by their mutual attraction. The electric field of this attraction oscillates with the plasma frequency  $(4\pi ne^2/m_e)^{1/2}$ , where  $n$  is plasma number density,  $e$  and  $m_e$  are the electron charge and mass, respectively. The characteristic scale of this electric field is defined by the Debye radius  $\lambda_D = [KT_e/(4\pi ne^2)]^{1/2}$ , where  $K$  is the Boltzmann constant and  $T_e$  is electron temperature. Providing there is a sufficient number of particles within a sphere of the radius  $\lambda_D$ , the internal electric field which exists between electrons and ions is shielded on scale lengths larger than  $\lambda_D$ .

In the external magnetic field  $\mathbf{B}$ , motion of charged particles is defined by the Lorentz force  $\mathbf{F}_L = (q/c)\mathbf{V} \times \mathbf{B}$  which results in the cyclotron motion of the particle with a gyrofrequency  $\omega_c = (qB)/(mc)$ . Here  $q$  is the particle charge and  $c$  is the speed of light. The radius of the motion is called the Larmor radius  $R_L = mV_\perp c/(qB)$  where  $V_\perp$  is a velocity component perpendicular to the magnetic field. An external force  $\mathbf{F}$  causes periodic acceleration and deceleration of the particle within one

gyroperiod. This results in a drift with the velocity  $\mathbf{V}_d = [c/(qB^2)]\mathbf{F} \times \mathbf{B}$ . This means that for spatial scales larger than the Larmor radius, the motion of particles can be described as the motion of a guiding centre with the velocity  $\mathbf{V}_d$  directed perpendicular to  $\mathbf{B}$  and  $\mathbf{F}$ . For an ensemble of particles, this allows us to consider plasma as a fluid of particles' guiding centers and use the magnetohydrodynamic (MHD) method to describe plasmas.

### 1.3.2 Magnetohydrodynamic Equations

Providing the characteristic scale is larger than the Larmor radius and Debye length, and the characteristic evolution time is greater than the period of plasma and gyro oscillations, the plasma density and velocity can be described by fluid equations:

$$\frac{\partial n_{i,e}}{\partial t} + \nabla \cdot (n_{i,e} \mathbf{V}_{i,e}) = 0, \quad (1.1)$$

$$\rho_{i,e} \frac{\partial \mathbf{V}_{i,e}}{\partial t} + \rho_{i,e} (\mathbf{V}_{i,e} \cdot \nabla) \mathbf{V}_{i,e} = \frac{1}{n_{i,e}} \mathbf{F}_{i,e}, \quad (1.2)$$

where  $\rho = mn$  is density. Equations (1.1) and (1.2) should be self-consistent with the plasma neutrality equation

$$\nabla \cdot (n_e \mathbf{V}_e) = \nabla \cdot (n_i \mathbf{V}_i). \quad (1.3)$$

In most problems, electrons can be considered massless when compared to the much heavier ions. In this case, the ion motion is described by (1.2) whereas the electrons simply follow the motion of ions. Then the neutrality equation can be reduced to  $n_e = n_i$  and plasma can be described by the one fluid (ion) equations.

If  $\mathbf{F}$  in (1.2) includes a pressure gradient term, an additional equation of state prescribing the pressure as a function of density  $\rho$  and temperature  $T$  is required. For an ideal gas, an equation of state is:  $P = nKT$ . For an adiabatic case, temperature can be excluded and the equation of state becomes  $P/\rho^\gamma = C$ , where  $C$  is a constant and  $\gamma$  is a ratio of specific heat, also called the adiabatic constant. In space plasmas, we typically consider particles with three degrees of freedom, so that  $\gamma = 5/3$ . For a nonadiabatic process, pressure can be obtained from the equation of state and the energy continuity equation:

$$\frac{\partial W}{\partial t} + \nabla \cdot \mathbf{Q} = \Lambda, \quad (1.4)$$

where  $W$  is total energy in the system,  $Q$  is an energy flux and  $\Lambda$  is an operator describing internal gains and losses of energy.

If we neglect the thermoconductivity and viscosity tensors and assume that resistivity  $\eta$  is uniformly distributed in the media, we can derive the following energy equation [Landau and Lifshitz, 1984]:

$$\frac{\partial P}{\partial t} + \nabla \cdot (\gamma P \mathbf{V}) - (\gamma - 1) \left( \mathbf{V} \cdot \nabla P + \frac{c^2 \eta}{16\pi^2} |\nabla \times \mathbf{B}|^2 \right) = 0, \quad (1.5)$$

In order to complete the MHD set of equations, an equation describing the connection between the magnetic field and plasma flow should be added. This equation can be obtained from Maxwell's equations and Ohm's law.

$$\nabla \times \mathbf{B} = \frac{4\pi}{c} \mathbf{j} + \frac{1}{c} \frac{\partial \mathbf{E}}{\partial t}, \quad (1.6)$$

$$\nabla \cdot \mathbf{B} = 0, \quad (1.7)$$

$$\nabla \times \mathbf{E} = -\frac{1}{c} \frac{\partial \mathbf{B}}{\partial t}, \quad (1.8)$$

$$\nabla \cdot \mathbf{E} = 4\pi \rho_q, \quad (1.9)$$

where  $\mathbf{B}$  and  $\mathbf{E}$  are magnetic and electric fields, respectively,  $\mathbf{j}$  is the current density, and  $\rho_q = n_i - n_e$  is the charge density.

The current density can be found from the generalized Ohm's law as

$$\mathbf{j} = \sigma \left[ \left( \mathbf{E} + \frac{1}{c} \mathbf{V} \times \mathbf{B} \right) + \frac{1}{ne} \nabla P_e - \frac{1}{cne} \mathbf{j} \times \mathbf{B} - \frac{m_e}{ne^2} \left( \frac{\partial \mathbf{j}}{\partial t} + \nabla(\mathbf{j} \cdot \mathbf{V}) \right) \right], \quad (1.10)$$

where  $\sigma$  is the electrical conductivity. If electrons can be assumed cold and massless, the electron pressure  $((1/ne) \nabla P_e)$  and electron inertia  $((m_e/ne^2)(\partial \mathbf{j}/\partial t) + \nabla(\mathbf{j} \cdot \mathbf{V}))$  terms can be omitted. In some problems dealing with magnetospheric plasmas, the Hall term in the right hand side of (1.10) can also be neglected. In this case, Ohm's law becomes:

$$\eta \mathbf{j} = \mathbf{E} + \frac{1}{c} \mathbf{V} \times \mathbf{B}. \quad (1.11)$$

where  $\eta = \sigma^{-1}$  is resistivity.

When analysing processes in plasmas with small resistivity, we obtain the ideal MHD equation  $\mathbf{E} = -(1/c) \mathbf{V} \times \mathbf{B}$ , also called the ideal Ohm's law. For this case, Alfvén derived an important equation which connects the motion of plasma and magnetic field lines [*Alfvén and Fälthammar, 1963*]:

$$\frac{d}{dt} \frac{\mathbf{B}}{\rho} = \left( \frac{\mathbf{B}}{\rho} \cdot \nabla \right) \mathbf{V}. \quad (1.12)$$

Let us consider a line of fluid with plasma particles on it. If  $\mathbf{V}$  is a speed of the line at one point, it will be  $\mathbf{V} + (d\mathbf{l} \cdot \nabla)\mathbf{V}$  at the distance  $d\mathbf{l}$  from this point along the line. Therefore, the distance  $d\mathbf{l}$  will change with time as  $dt(d\mathbf{l} \cdot \nabla)\mathbf{V}$  or

$$\frac{d}{dt}d\mathbf{l} = (d\mathbf{l} \cdot \nabla)\mathbf{V}. \quad (1.13)$$

As seen from (1.12) and (1.13), time evolution of vectors  $d\mathbf{l}$  and  $\mathbf{B}/\rho$  is defined by the same equation. For example, if these vectors are initially parallel to each other they will remain parallel and their lengths will change at the same rate. Therefore, if two particles are initially on the same magnetic field line they will move with this field line. This means that if plasma is nonresistive, magnetic field lines are frozen to the plasma. In the case when the magnetic field is transverse and plasma is uniform along the magnetic field lines, equation (1.12) becomes  $d(B/\rho)/dt = 0$ . In some problems, this allows us to replace the motion of magnetic field lines by the motion of plasma and consider a two-dimensional (2D) problem instead of a three-dimensional (3D) one. The ratio of the magnetic force and density is called the “effective gravity” in such problems.

We shall be considering non-relativistic velocities  $V_0 = L_0/t_0 \ll c$ , where  $V_0$ ,  $L_0$ , and  $t_0$  are the characteristic velocity, scale length, and time, respectively. In this case, we can compare the term  $\partial\mathbf{E}/\partial t$  with  $c \nabla \times \mathbf{B}$  as follows:

$$\frac{|\partial\mathbf{E}/\partial t|}{c|\nabla \times \mathbf{B}|} \sim \frac{V_0 B_0/t_0}{c^2 B_0/L_0} \sim \frac{V_0^2}{c^2}, \quad (1.14)$$

where  $B_0$  and  $E_0$  are the characteristic values of the magnetic and electric fields, respectively, and  $E_0 = (1/c)V_0 B_0$  from the ideal Ohm’s law.

Therefore, the term  $\partial\mathbf{E}/\partial t$  can be neglected in a nonrelativistic plasma which

results in

$$4\pi\mathbf{j} = c \nabla \times \mathbf{B}. \quad (1.15)$$

Combining this equation with (1.11) and  $\partial\mathbf{B}/\partial t = -c \nabla \times \mathbf{E}$ , one arrives at:

$$\frac{1}{c} \frac{\partial \mathbf{B}}{\partial t} = \nabla \times \left( \frac{1}{c} \mathbf{V} \times \mathbf{B} - \frac{c\eta}{4\pi} \nabla \times \mathbf{B} \right). \quad (1.16)$$

The first term on the right-hand side of (1.16) represents the motion of the magnetic field lines with the plasma, whereas the second term describes the diffusion of the magnetic field through the plasma. However, this resistive diffusion should be small in order to justify the assumptions we made to derive (1.15). In this study, we shall consider only ideal MHD problems and use this small resistive diffusion in (1.16) only for a numerical stability purpose.

Equations (1.1), (1.2), (1.5), and (1.16) form the entire set of one-fluid MHD equations which allow us to describe numerous processes in the magnetospheric plasma.

### 1.3.3 MHD Waves

The MHD equations allow for the existence and propagation of three basic wave modes. These are the shear Alfvén wave (SAW), and compressional fast and slow modes. In a homogeneous plasma, these modes are linearly decoupled from each other. However, coupling between them occurs if we consider nonlinear processes or if these waves propagate in a nonuniform media.

An equation describing the wave vector  $\mathbf{k}$  as a function of a frequency  $\omega$  is

called a dispersion relation. In Cartesian geometry  $(x, y, z)$ , a dispersion relation for the shear Alfvén wave in the homogeneous ideal plasma can be derived using equations (1.2) and (1.16):

$$\frac{\partial^2 \mathbf{V}}{\partial t^2} = V_A^2 \frac{\partial^2 \mathbf{V}}{\partial z^2}, \quad (1.17)$$

where  $V_A = B/(4\pi\rho)^{1/2}$  is the Alfvén speed and the  $z$  axis is chosen in the direction of the ambient magnetic field  $\mathbf{B}_0$ .

If we assume a SAW in the form  $\mathbf{V} = \mathbf{V}_0 \exp[-i(\omega t - \mathbf{k} \cdot \mathbf{r})]$ , where  $\mathbf{V}_0$  is the wave amplitude and  $\mathbf{r}$  is a position vector, we obtain a dispersion relation of the SAW:

$$\frac{\omega^2}{k^2} = V_A^2 \cos^2 \vartheta, \quad (1.18)$$

where  $\vartheta$  is an angle between the ambient magnetic field  $\mathbf{B}_0$  and the wave vector  $\mathbf{k}$ .

The group velocity of a SAW which is defined as  $\partial\omega/\partial\mathbf{k}$  is collinear with the direction of the ambient magnetic field. Therefore, these waves can transport energy only along magnetic field lines.

The dispersion relation for the slow and fast modes is

$$\frac{\omega^2}{k^2} = \frac{1}{2} \left( V_A^2 + C_S^2 \pm \left[ (V_A^2 + C_S^2)^2 - 4V_A^2 C_S^2 \cos^2 \vartheta \right]^{\frac{1}{2}} \right), \quad (1.19)$$

where  $C_S = (\gamma KT/m_i)^{1/2}$  is the speed of sound in a plasma. In cold plasmas,  $C_S$  is zero and the compressional fast mode is described by  $\omega^2/k^2 = V_A^2$ . This wave transports energy isotropically with the group velocity equal to the Alfvén speed.



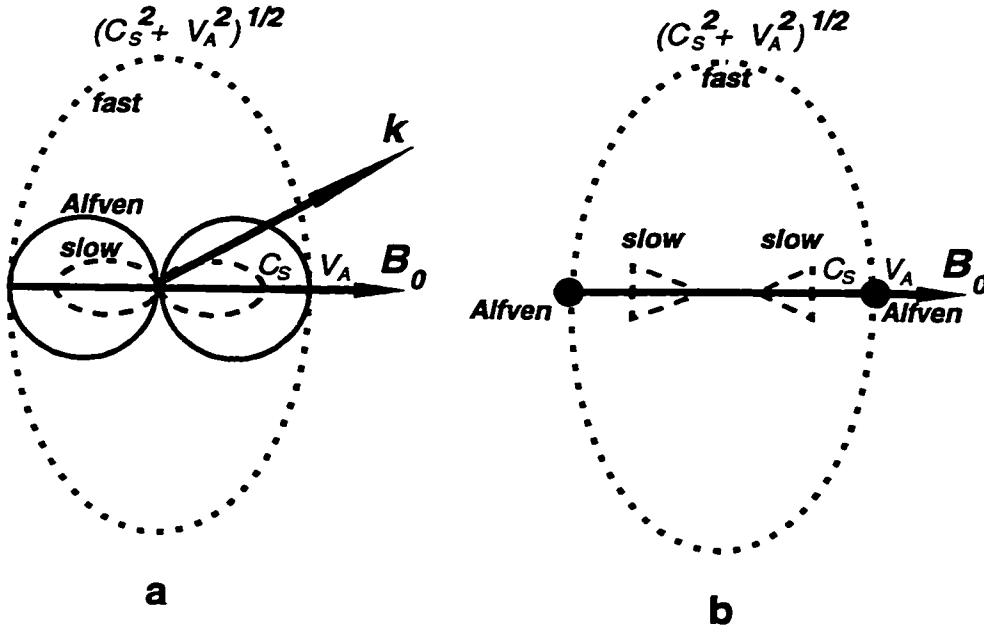


Figure 1.1: The phase (a) and group (b) velocities of the Alfvén wave (solid line), slow mode (dashed line), and fast mode (dotted line) as a function between the ambient magnetic field and wave vectors.

The slow mode does not propagate in cold plasmas where  $C_s = 0$  and hence the slow mode frequency is zero.

If the plasma temperature is nonzero, the fast and slow modes are driven by both magnetic tension and thermal pressure. However, oscillations of the magnetic field and plasma density occur in phase in the fast mode and out of phase in the slow mode. This feature is often used to distinguish these modes in experiments.

A diagram of the MHD mode propagation and energy transport is presented in Figure 1.1. In this example,  $C_s < V_A$  which is typical for magnetospheric plasmas. As seen from the diagram, the fast mode propagates in all directions. The fastest propagation occurs in the direction perpendicular to the ambient magnetic field. This wave transports energy in all directions. The slow mode propagates and transports energy mainly along the ambient magnetic field. The SAW has reciprocal

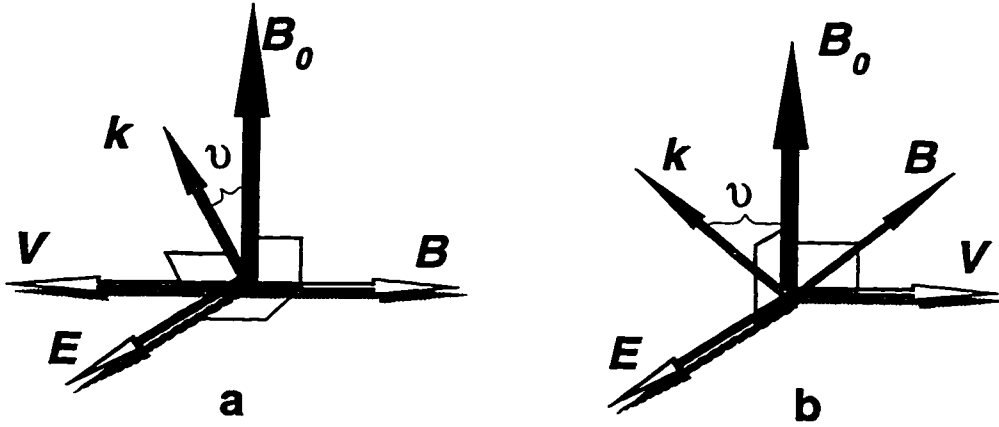


Figure 1.2: Shear Alfvén wave (a) and compressional mode (b).

fronts. The energy transport occurs only along the ambient magnetic field lines with the group velocity  $V_A$ .

Vector diagrams for the shear Alfvén wave and compressional fast mode in a cold plasma are shown in Figure 1.2. In this diagram, vectors  $\mathbf{B}$  and  $\mathbf{V}$  show the direction of the magnetic field and velocity perturbations, respectively. For a SAW, vectors  $\mathbf{B}$  and  $\mathbf{V}$  are parallel (or antiparallel) to each other and perpendicular to the ambient magnetic field  $\mathbf{B}_0$ . Vector  $\mathbf{k}$  is perpendicular to  $\mathbf{V}$  which means that SAWs are incompressible. The magnetic perturbation of the fast mode lies in the plane  $[\mathbf{B}_0, \mathbf{V}]$ , however  $\mathbf{B} \cdot \mathbf{B}_0 \neq 0$  and  $\mathbf{k} \cdot \mathbf{V} \neq 0$ . This means that the fast mode involves a compression of plasma and magnetic field.

In non-uniform dispersive media, the behavior of these modes becomes more complex and the clear distinction between them disappears. Also, these modes can couple to each other via resonances. One type of resonant interaction, namely coupling of fast and SAW modes, is called the field line resonance (FLR). Below, we introduce a brief theory of FLR while its applicability to the magnetospheric processes and magnetosphere-ionosphere interaction will be discussed later in the

Introduction and in Chapter 3.

### 1.3.4 MHD theory of Field Line Resonances

The linear theory of field line resonances (FLR) was developed by *Chen and Hasegawa* [1974] and *Southwood* [1974]. They studied coupling between the fast compressional mode and the SAW in the presence of a radial gradient of the Alfvén velocity. A brief outline of this theory is presented below.

Let us assume that the Alfvén velocity distribution is nonuniform in the  $x$ -direction and that the electric field perturbation is in the form of a monochromatic wave:  $\mathbf{E} = \mathbf{E}_{x,y} \exp(-i(\omega t - k_y y - k_z z))$ . Then the linearized set of MHD equations can be reduced to the wave equation

$$\frac{\partial^2 E_y}{\partial x^2} - \frac{k_y^2}{[(\omega/V_A)^2 - k_z^2]\kappa^2} \frac{\partial}{\partial x} \left( \frac{\omega}{V_A} \right)^2 \frac{\partial E_y}{\partial x} + \kappa^2 E_y = 0, \quad (1.20)$$

where  $\kappa^2 = \frac{\omega^2}{V_A^2} - k_y^2 - k_z^2$ .

Equation (1.20) has two singularities. The first point corresponds to  $\kappa^2 = 0$  and was defined as the turning point where the compressional wave changes from propagating to evanescent. The second singularity occurs when  $\omega^2/V_A^2 = k_z^2$ . This point relates to the resonant position where the wave equation can be approximated by

$$\frac{\partial^2 E_y}{\partial x^2} + \frac{1}{x - x_0} \frac{\partial E_y}{\partial x} + \kappa^2 E_y = 0,$$

and

$$E_x = \frac{-ik_y(\partial E_y / \partial x)}{\frac{\omega^2}{V_A^2} - k_z^2 - k_y^2}, \quad (1.21)$$

where  $x_0$  is the resonant point position.

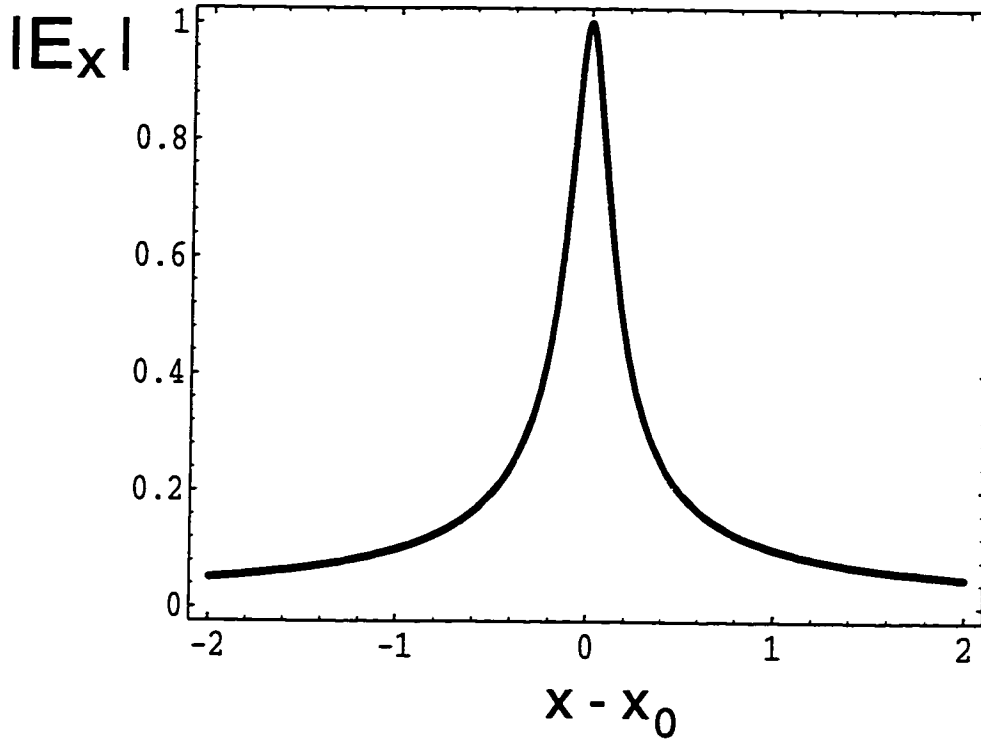


Figure 1.3: Radial ( $x$ ) distribution of normalized  $E_x$  component around the FLR point.

The solution to (1.21) goes to infinity at the resonant point. However, *Chen and Hasegawa* [1974] and *Southwood* [1974] showed that the singularity can be avoided if there is small amount of dissipation in the system. Then the solution for  $E_x$  normalized by the  $E_{x,max}$  is:

$$E_x = \frac{-[\varepsilon + i(x - x_0)]}{k_y[(x - x_0)^2 + \varepsilon^2]}, \quad (1.22)$$

where  $\varepsilon$  is a coefficient which depends on damping.

The form of solution for (1.21) is shown in Figure 1.3. As seen from this figure, electric field has a strong peak around the resonant point where the SAW

is driven by the fast compressional mode. This suggests that SAWs can grow to large amplitudes and accumulate energy at resonant points. Note that the solution shown in Figure 1.3 presumes a monochromatic compressional wave driver. The general existence of such waves in the Earth's magnetosphere will be discussed later in Chapter 1.

### 1.3.5 Shear Flow and Ballooning Instabilities

The theory of FLRs predicts that the velocity field of SAWs grows in the FLR region and is radially structured around the resonant point. The fundamental SAW harmonic has nodes of the azimuthal velocity field in the ionosphere and antinodes in the equatorial plane. This implies that SAWs in the equatorial magnetosphere may eventually become unstable with respect to the shear flow instability. Moreover, equation (1.22) predicts a  $180^\circ$  SAW phase shift across the resonant region. This shift may also result in strong shears of the velocity. Therefore, the FLR theory suggests that the FLR region may become unstable with respect to shear flow instabilities.

In this project, we study the evolution of the shear flow instability and its interaction with ballooning modes which can develop in the presence of pressure gradients and stretched magnetic field lines. Therefore, let us briefly describe the origin of these modes.

#### Shear Flow (Kelvin-Helmholtz, KH) Instability

The physical process responsible for driving the KH instability can be understood as follows. Let us assume that plasma density is constant in the region where the

shear in the flow exists. Suppose that a small perturbation of the perpendicular component of the velocity appears in the shear flow. This involves motion of plasma from a region of higher velocity to a region of lower velocity (perpendicular to the ambient flow), and leads to a reduction of the velocity in the direction of the shear flow. However, if the plasma is incompressible, this reduction of velocity should be compensated by a gain in the perpendicular component in order to keep the velocity field divergence free. Therefore, the flow deviates from its initial direction. This initiates a shear flow vortex. The instability saturates when the kinetic energy of the shear flow is transferred into the kinetic energy of the vortex.

The simplest case of a shear flow instability arises when a plane two-dimensional perturbation is embedded into a shear flow which is perpendicular to the ambient magnetic field, and the wave vector is parallel to the shear flow. Assuming the ambient plasma density, pressure and magnetic field are uniform, the linear growth is defined by the dispersion relation

$$V_{\perp}'' = k^2 V_{\perp} \left[ 1 - \frac{V_0''}{k(\omega - kV_0)} \right], \quad (1.23)$$

where  $V_0$  is the ambient shear flow velocity,  $V_{\perp}$  is a velocity perturbation perpendicular to  $V_0$ ,  $k$  is the wave number, and  $\omega$  is the angular frequency. The second derivative is taken with respect to the direction perpendicular to the shear flow.

A solution for the dispersion relation (1.23) provides us with the KH mode eigenfrequencies and eigenfunctions (e.g., [Miura and Pritchett, 1982], see also Chapter 4 of this thesis). If  $\text{Im}\omega$  is positive, the corresponding mode is unstable and grows exponentially with the growth rate  $\gamma = \text{Im}\omega$ . Figure 1.4 illustrates dependance of the growth rate and frequency  $\text{Re}\omega$  on the wave number  $k$  for a Gaussian flow  $V(x) = V_0 \exp(-x^2/\delta^2)$ . Here  $\delta$  is a half-width of the shear. As seen from Figure

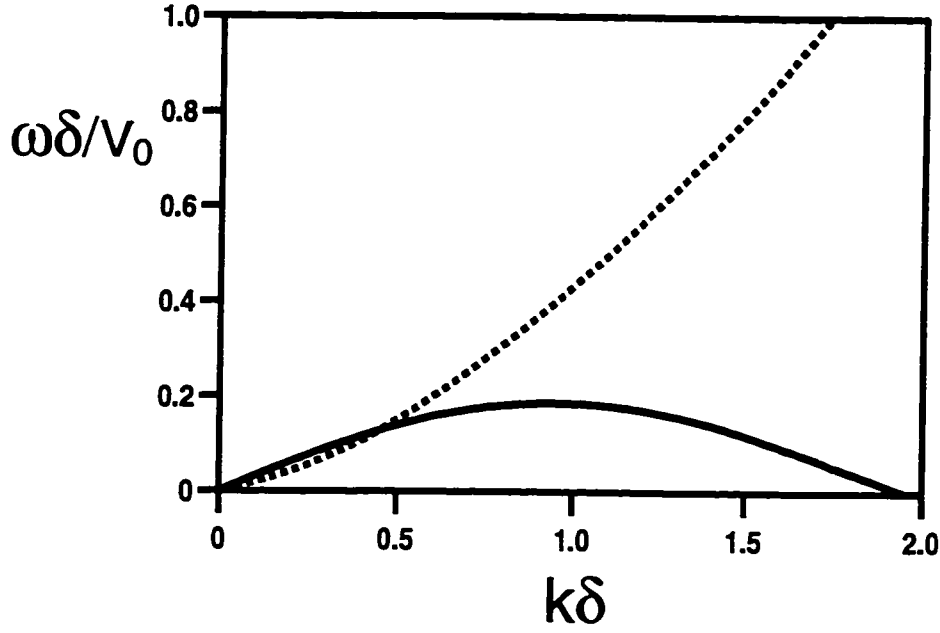


Figure 1.4: Dependence of the growth rate (solid line) and frequency (dashed line) on the wave number for a Gaussian uni-directional flow.

1.4, the most unstable modes correspond to the wavenumbers  $k \sim 1/\delta$ .

When the ambient magnetic field has a component which is directed parallel (or antiparallel) to the wave vector, the growth rate decreases and the magnetic field can completely stabilize KH modes [Miura and Pritchett, 1982]. However, the magnetic field can stabilize the instability even when it is totally transverse. It happens in the presence of the magnetic shear or magnetic curvature [Miura and Pritchett, 1982; Tajima et al., 1991].

In the three-dimensional (3D) case, the finite field-aligned wave length and magnetic field line bending at the boundaries also stabilize the growth of the perturbation [Miura and Pritchett, 1982; Miura and Kan, 1992; Galinsky and Sonnerup, 1994]. These effects will be discussed in chapter 5 where we study evolution of the

KH instability on dipolar magnetic field lines.

### Ballooning Instabilities

If a pressure gradient is in equilibrium with another force, this equilibrium can be unstable with respect to plasma motion in the direction of the pressure gradient. The physical scenario of the instability can be described as follows (Figure 1.5). Let us consider a simple example in which plasma pressure is initially in equilibrium with the gravitational force  $\rho g$ . An imposed initial velocity perturbation moves plasma from the higher pressure region A to the lower pressure region B. Increased pressure in region B moves plasma in the direction perpendicular to the initial pressure gradient. As a result, plasma density in cell C grows. An increased gravitational force  $\rho g$  in cell C causes plasma to move from cell C to cell D, contributing to the initial perturbation. This instability is called ballooning.

If the length scale of the pressure gradient is much larger than the scale of the initial perturbation, this initial perturbation can be assumed in the form  $V_x = V_{x0} \exp[-i(\omega t - k_x x - k_y y)]$ . Then the linear dispersion relation for the ballooning instability has a simple form

$$\omega^2 = \frac{k_y^2}{k^2} W^2, \quad (1.24)$$

where  $k^2 = k_x^2 + k_y^2$ , and  $W$  is called Brunt-Väisälä frequency:

$$W^2 = -\frac{g\rho'}{\rho} - \frac{g^2}{V_f^2}, \quad (1.25)$$

$V_f^2 = C_s^2 + V_A^2$  is the square of the fast mode velocity in the direction perpendicular



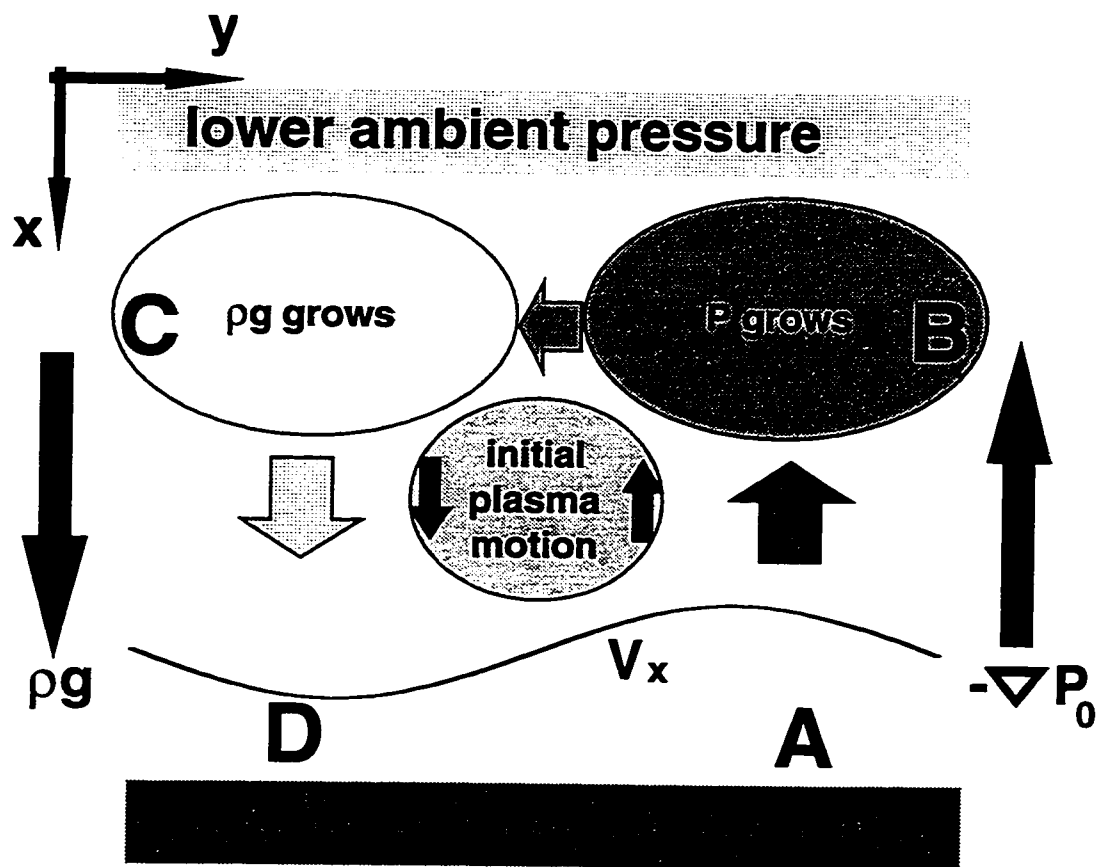


Figure 1.5: Schematic of the ballooning instability.

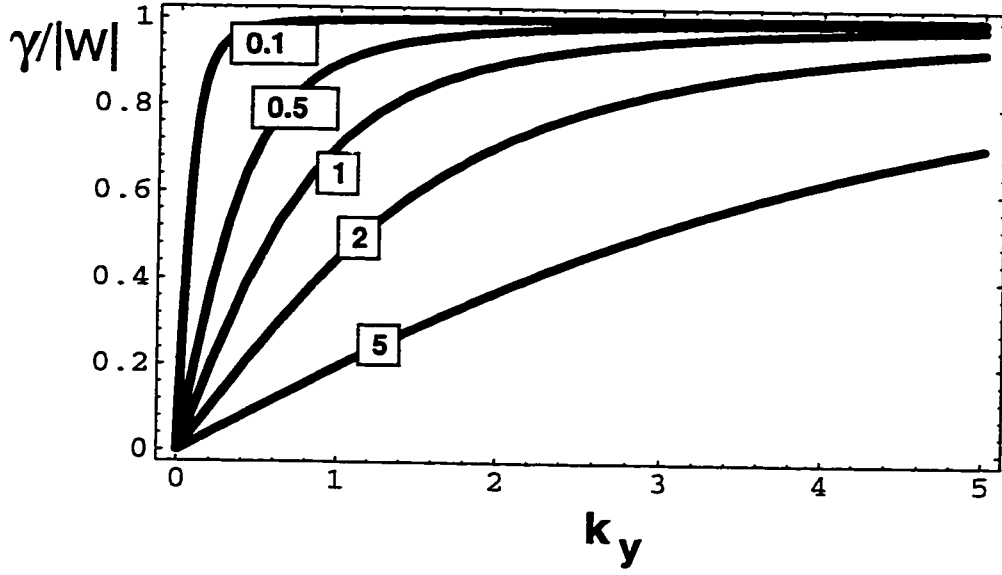


Figure 1.6: Dependence of the growth rate of ballooning modes on  $k_y$  for different  $k_x$  labelled in the plot.

to the ambient magnetic field, and  $\rho'$  is the density gradient in the  $x$ -direction.

If the plasma temperature is uniform, the dispersion relation (1.25) describes the well known Rayleigh-Taylor instability, which is unstable if the gravity and pressure gradients are antiparallel. However, the configuration shown in Figure 1.5 is stable with respect to the Rayleigh-Taylor instability. Therefore, the ballooning mode can be destabilized only if there is a nonzero temperature gradient. The marginal stability occurs when  $P' = V_f^2 \rho'$ . In the particular case when density is uniform, the configuration shown in Figure 1.5 is always unstable with respect to the ballooning instability. Note that a ballooning unstable mode has the frequency  $\text{Re} \omega$  equal zero.

The dependence of the growth rate on the wavenumber  $k_y$  is shown in Figure 1.6 for different  $k_x$ . As seen from the figure, the growth rate grows when  $k_x$  decreases and  $k_y$  increases. When  $k_y/k_x \gg 1$ , the growth rate becomes approximately

independent of  $k_y$ .

In this section, we have briefly described the basics of MHD waves, FLRs, and KH and ballooning instabilities. These physical processes play an important role in the dynamics of the magnetosphere as mechanisms which allow for energy storage and release. Now, let us give a brief description of the Earth's magnetosphere and discuss the applicability of the above mentioned processes to magnetospheric plasmas.

## 1.4 Magnetosphere of the Earth

### 1.4.1 Main Regions of the Earth's Magnetosphere

The Earth's magnetosphere is a result of the coupling of the solar wind with the Earth's magnetic field. The solar wind is in fact an extension of the upper atmosphere of the Sun - the solar corona. This magnetized plasma outflow reaches the position of the Earth at speeds of 300-700 km/sec depending on solar activity. The typical parameters of the solar wind near the Earth's orbit are: a plasma of mainly protons and electrons with density  $\sim 10 \text{ cm}^{-3}$ ; a proton temperature of the order of  $10^5 \text{ K}$  with an electron temperature 2-3 times higher. The magnetic field of the solar wind (or IMF - interplanetary magnetic field) is typically  $\sim 5\text{-}10 \text{ nT}$ . The speed of sound and Alfvén speed for these parameters are of the order of tens of km/s. Therefore, the solar wind represents a supersonic and super Alfvénic flow.

Perhaps, the first idea that the solar wind is an expansion of the solar corona belongs to Chapman who was inspired by the discovery of the very high temperature regions in the solar corona. Following this idea, *Parker* [1958] suggested a

quantitative theory of the plasma outflow and gave it the name solar wind. The first satellite measurements confirmed Parker's theory and experimentally proved that the solar wind plays an essential part in transporting plasma energy from the Sun to the near Earth space environment [*Brandt, 1970*].

In the vicinity of the Earth (at  $\sim 10R_E$  on the dayside), the dynamical pressure of the solar wind is approximately equal to the pressure of the Earth's magnetic field, which causes solar wind to deviate and flow around the Earth. Because of the supersonic speed of the solar wind, a collisionless bow shock forms in front of the Earth (see review by *Russell and Hoppe [1983]*). In turn, the solar wind compresses the Earth's magnetic field on the dayside and stretches magnetic field lines on the nightside forming the magnetosphere of the Earth with the boundary called the magnetopause. The current responsible for the magnetic field deformation was theoretically predicted by *Chapman and Ferraro [1931]* and called the DCF (Disturbance of Corpuscular Flux) or CF (Chapman-Ferraro) current. The space between the bow shock and the magnetopause is called the magnetosheath which comprises the shocked and heated plasma from the solar wind.

*Axford and Hines [1961]* suggested that the viscous coupling of the solar wind with the Earth's magnetosphere may produce an electric field within the magnetosphere. They called this process "quasiviscosity". Inside the magnetosphere, this electric field is directed mainly from dawn to dusk which is in agreement with observations of steady state magnetospheric convection.

Another way to transport energy from the solar wind into the Earth's magnetosphere was proposed by *Dungey [1961]*. If the Earth's magnetic field and the IMF are oppositely directed, they may interact via merging. On the day side, the Earth's magnetic field is directed approximately northward and therefore can be

merged with a southward component of the IMF. This process results in tearing of the magnetopause, the outer surface of the magnetosphere, which may provide a direct input of energy into the magnetosphere. The resulting global electric field was found to be in the same direction as the “quasiviscous” electric field. Further observations showed that this electric field can be much higher in amplitude than the “quasiviscous” electric field and therefore, it may initiate plasma convection of larger velocity [Reiff *et al.*, 1981].

A third possible mechanism for energy transport through the magnetopause was proposed by Verzariu [1973]. MHD waves excited in the solar wind or in the magnetosheath due to fluctuations in pressure and velocity can be partially transmitted into the magnetosphere. It is important to note that this mechanism does not require mass and momentum transport through the boundary and therefore does not involve any boundary layer processes.

The velocity shear in the magnetosheath implies that the shear flow instability may develop on the magnetopause [Miura, 1984]. This mechanism involves the momentum transport through the magnetopause and may initiate propagation of MHD waves from the unstable region to the inner magnetosphere. Chen and Hasegawa [1974] and Southwood [1974] suggested that this mechanism may lead to the excitation of fast compressional modes which excite FLRs inside the magnetosphere.

A schematic of the Earth’s magnetosphere is presented in Figure 1.7. Let us briefly describe the main regions shown in this figure.

The magnetic field due to the magnetopause CF currents is responsible for the formation of the magnetotail in the night side of the magnetosphere. The CF current consists of two current loops at the magnetopause. The sum of the Earth’s

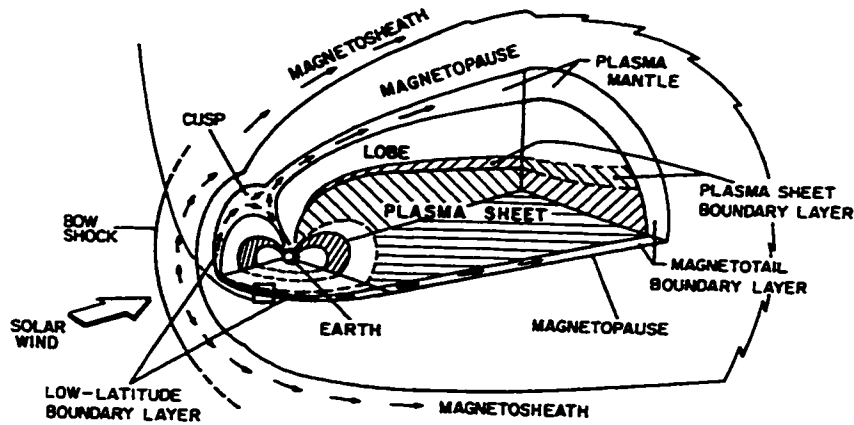


Figure 1.7: The 3D diagram of the Earth's magnetosphere from *Eastman et al.* [1985].

dipolar field and CF field forms two open regions in the dayside magnetosphere called the dayside cusps. During perturbations in the solar wind, the cusps may become azimuthally stretched (so called “clefts”) and maintain a direct intrusion of the electric field from the solar wind into the magnetosphere. This results in the spectacular dayside break-up - the fast azimuthal motion of auroral structures [Sandholt and Egeland, 1989]. Earthward of the magnetopause, there is a low latitude boundary layer (LLBL) - a magnetosphere boundary transition layer filled with plasmas from both the magnetosphere and magnetosheath. A region adjacent to the cusp on the tailward side is the high latitude boundary layer or plasma mantle. This region is also open for the solar wind. Inside the magnetosphere, there are regions of stretched tailward magnetic tubes filled with cold and low-density plasmas. These regions are called the tail lobes. The tail lobes map into the so-called polar caps above the Earth - the areas extending equatorward to  $\sim 75 - 80^\circ$  and expanding

during geomagnetic disturbances. There is evidence that the tail lobes lie on open magnetic field lines.

Typically, the polar caps have distinct boundaries formed by the poleward edges of the auroral oval. In the magnetosphere, these boundaries map into the plasma sheet boundary layer (PSBL) - the boundary between closed and open magnetic field lines. Inward from the PSBL, there is a region of hot plasmas called the plasma sheet (PS). The plasma in the PS flows earthward and onto the day-side from the magnetotail driven by the dawn-dusk electric field. This electric field results from the solar wind - magnetosphere interaction, as discussed above. In the neutral sheet, the central part of the magnetotail, stretched magnetic field lines change direction from tailward to Earthward. In this region, the dawn-dusk electric field accelerates protons in the dawn-dusk direction and electrons in the dusk-dawn direction, which forms a part of the crosstail magnetotail current.

PS plasmas flow earthward until the dipolar magnetic field deviates them from the sunward motion. PS electrons, which are normally cooler than protons, tend to move closer to the Earth. However, this motion is limited by plasma quasineutrality which causes electrons to escape along the magnetic field lines. This mechanism forms the inner edge of the PS at distances of  $\sim 6 - 10R_E$  from the Earth [Kavanagh *et al.*, 1968]. The inner plasma sheet is of particular interest in this study as a region where large amplitude FLRs are observed [Walker and Greenwald, 1981; Tian *et al.*, 1991; Potemra and Blomberg, 1996; Samson *et al.*, 1996a; 1998].

Earthward from the PS, there is the region of the westward ring current, also called DR-current (Disturbance of Ring current), formed due to the drift of particles in nonuniform magnetic field. This current may produce significant magnetic perturbations which are directed approximately along the Earth's axis from

the north to the south poles. This magnetic perturbation is a major mechanism responsible for the magnetic storms. The region of the DR-currents consists of high-temperature particles. These particles are trapped by the Earth's magnetic field [*Smith and Hoffman*, 1973]. Therefore, the region of the ring current is also called the trapped radiation belts or Van Allen belts. Occasional electron precipitations from this region may cause a dim luminosity called subauroral red (SAR) arcs.

The region of the magnetosphere closest to the Earth, the plasmasphere, consists mainly of cold plasmas which escape from the ionosphere and rotates with the Earth. Even though its shape can be slightly affected by the convection electric field, the influence of the solar wind - magnetosphere interaction is rather minor in this region.

#### 1.4.2 Ionosphere

The interaction of the ultra-violet radiation and precipitating particles with atmospheric gases causes the excitation and ionization of molecules. Ionized components can live sufficiently long for them to manifest collective electric properties, i.e., to behave as plasmas. This region of ionized atmosphere which extends from 80 to 1000 km is called the ionosphere.

The ionospheric E-region which is most important for this study extends from 100 to 180 km of altitude. This region represents a transition region between the gas and plasma states of the ionized components. For electrons, the gyrofrequency becomes larger than the collision frequency at  $\sim 90$  km which means that in the E-region, electrons are "frozen" into the magnetic field. For ions, this altitude is higher (around 180 km). In the presence of an external electric field  $\mathbf{E}$ , electrons



drift in the  $\mathbf{E} \times \mathbf{B}$  direction whereas the ion motion is defined by both gyrorotation and collisions. On average, this results in the separate motion of electrons and ions which manifests as a current system. This current system consists of an electron Hall current in the  $-\mathbf{E} \times \mathbf{B}$  direction and an ion Pedersen current in the  $\mathbf{E}$  direction. Therefore, the ionospheric E-region behaves as a conductive boundary for incident magnetospheric waves. The typical height integrated conductivity of the ionosphere is  $\sim 3 - 10 \text{ Ohm}^{-1}$ .

Reflection of Alfvén waves from the ionosphere is defined by the reflection coefficient  $R$  [Southwood and Hughes, 1983]. Assuming that  $V_A$  is uniform in the ionosphere, this coefficient is:

$$R = \frac{\Sigma_P - \Sigma_A}{\Sigma_P + \Sigma_A}, \quad (1.26)$$

where  $\Sigma_A = c^2/(4\pi V_A)$  is the wave conductivity and  $\Sigma_P$  is the height integrated Pedersen conductivity in the ionosphere. Dependence of reflection on the Pedersen conductivity is illustrated by Figure 1.8. If  $\Sigma_P \gg \Sigma_A$ , which means that the ionosphere is highly conductive,  $R \sim 1$ . This corresponds to the perfect reflection of Alfvén waves from the ionosphere. In this case, incident and reflected electric fields cancel each other providing nodes of the resulting electric field. Currents of the incident and reflected waves add which means that the wave magnetic field has antinodes in the ionosphere. Finite ionospheric conductivity  $\Sigma_P > \Sigma_A$  results in the partial absorption of the wave energy. The case  $\Sigma_P = \Sigma_A$  corresponds to total absorption. When  $\Sigma_P < \Sigma_A$ , currents due to the incident and reflected waves tend to cancel each other whereas electric fields add. In this study, we shall consider an extreme case when  $\Sigma_P \gg \Sigma_A$  ("super-conductive" ionosphere). However, the finite ionospheric conductivity may significantly modify magnetospheric waves [Allan and

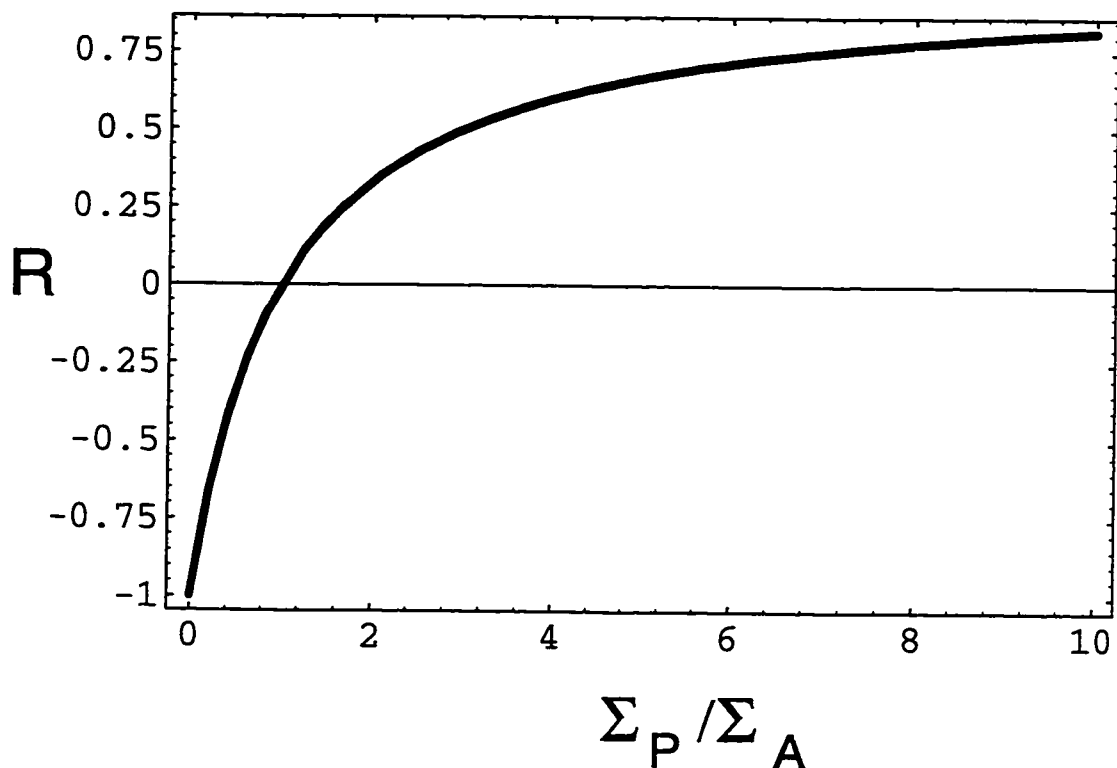


Figure 1.8: Dependence of the Alfvén wave reflection on the ionospheric conductivity.

*Knox*, 1979; *Miura*, 1996]. We shall discuss these effects in chapters 3-5.

At higher altitudes (so called the ionospheric F-region), both electrons and ions are “frozen” to the Earth’s magnetic field and therefore, the motion of plasmas is defined by the  $\mathbf{E} \times \mathbf{B}$  drift. Observations of the velocity of this drift are extremely important because they allow one to obtain the value of the electric field at the ionospheric level and to map it to the magnetosphere along the magnetic field lines. High latitude ionospheric electric fields due to the magnetosphere-ionosphere interaction are typically of the order of 10 mV/m and can grow up to in excess of 100 mV/m during auroral disturbances.

### 1.4.3 Large-Scale Field Aligned Currents

During intense magnetospheric disturbances, the total ionospheric current reaches  $10^6$  A and the total dissipated power may be as high as  $10^8$  kW. This power release is provided by the magnetosphere - ionosphere coupling via field aligned currents (FACs).

Traditionally, large-scale FACs are classified according to the spatial regions where they are observed. Region 1 is generated by the interaction of the solar wind with the Earth's magnetosphere. The solar wind flow polarizes the magnetosphere resulting in an electric field directed from dawn to dusk. This electric field is closed through the polar ionosphere by two sheets of FACs flowing downwards in the morning side and upwards in the evening. The poleward border of these current sheets corresponds to the boundary of the polar cap.

The origin of region 2 FACs is still the subject of study. These currents are driven in the plasmasheet. They are projected into the ionosphere in the equatorial portion of the auroral oval.

Here, we have only mentioned large-scale FACs and do not describe the generation of FACs in the midnight sector, where the currents of region 1 and 2 seem to overlap with one another. This region is also seen in the convection patterns as a reversal of the plasma flow and called the Harang discontinuity [*Baumjohann et al.*, 1981; *Robinson and Vondrak*, 1990]. FACs in this region, as well as small-scale FACs, play a significant role in auroral disturbances and we shall consider them separately below.

#### 1.4.4 Magnetospheric Substorms

A magnetospheric substorm is a sudden release of energy derived from the solar wind via the solar wind - magnetosphere interaction and stored in the nightside magnetosphere. According to *Rostoker et al.* [1980], “the term magnetospheric substorm describes an interval of increased energy dissipation confined, for the most part, to the region of the auroral oval. The onset of this process is signaled by explosive increases in auroral luminosity in the midnight sector, and the entire process encompasses an interval during which the strength of the current in the auroral electrojets increases from and returns to the background level from which the substorm arose.”

*Akasofu* [1977] proposed the separation of a substorm into three stages which are characterized by different physical processes in the magnetosphere - ionosphere system.

For most substorms, the first stage, called the growth phase, typically starts after IMF becomes more southward. During this stage, which lasts for approximately 1 hour, a significant amount of energy becomes stored in the magnetotail. As discussed in previous sections, a southward turning of the IMF leads to growth of the cross-tail magnetospheric electric field. An increased cross-tail electric field initiates particle energization within the neutral sheet. The protons are accelerated across the magnetotail and move earthward. This generates an earthward pressure gradient at the inner edge of the plasmasheet [*Roux, et al.* 1991; *Kistler et al.*, 1992]. Both the cross-tail particle acceleration and the pressure gradient in the inner plasmasheet increase the cross-tail current in the equatorial plane of the magnetosphere. As a result, the magnetic field lines gradually stretch tailward which leads to the narrowing of the plasma sheet and equatorward motion of the auroral arcs. Such a magnetic field topology appears to provide the main reservoir for the energy stored

during the substorm growth phase.

Using simultaneous data from a ground based photometer array and DMSP satellite particle detectors, *Samson et al.* [1992b] found intense precipitation of protons with an average energy around 30 keV at the beginning of the substorm growth phase. The energy of the precipitating protons is higher than the average energy of plasma sheet protons which is typically below 10 keV. The precipitation is structured within a band of  $\sim 2^\circ$  of latitude and creates proton aurora ( $H\beta$  emissions) seen by photometers at wavelengths of 5577 and 4861 Å. Both satellite and photometer data presented by *Samson et al.* [1992b] indicate that the maximum of the proton precipitation appears  $\sim 1 - 2^\circ$  equatorward of the boundary of the intense electron precipitation. *Samson et al.* [1992b] and *Lyons and Samson* [1992] suggested that this precipitation is the signature of a population of hot protons at the inner edge of the plasmashet, which in turn indicates a significant Earthward pressure gradient in the region. On the other hand, recent observations [*Samson et al.* 1996a] indicate that large amplitude FLRs appear in this region during the growth phase. This suggests that growing SAWs may be important in the destabilization of this region.

The energy loading and topological changes which occur in the nightside magnetosphere during the growth phase can bring the magnetosphere into an unstable state. This triggers the sudden release of energy called substorm expansive phase onset. An onset can be determined using ground based magnetometers from an abrupt decrease in the H-component of the Earth's magnetic field and the growth of magnetic pulsations in the frequency range 6-25 mHz (called Pi2 pulsations). At the same time, discrete aurora intensifies and evolves in a large scale (of the order of hundred kilometers) surge. This process occurs within a few minutes and is called auroral breakup. The auroral surge is produced by energetic ( $\sim 5-10$  keV) electrons

with maximum intensity at the front of the surge. These electrons feed an upward FAC which is closed by an ionospheric current flowing in the westward direction along the surge. The surge expands westward (so called the westward travelling surge) and poleward. At the same time, ionospheric currents grow and form a large scale westward electrojet (which is part of the substorm current wedge). The whole process, from the substorm triggering to the motion of auroras and formation of the intense westward electrojet, is called the substorm expansion phase.

Satellite observations in the vicinity of the substorm onset have revealed a reduction in the cross tail current and further expansion of the reduced current region westward and tailward [*Jacquey et al.*, 1991, 1993; *Ohtani et al.*, 1992]. The field lines from the reduced current region have a footprint at the location of the active auroras in the ionosphere. Therefore, the spacecraft observations are consistent with the ground based observations of the westward and poleward motion of the substorm current wedge.

During the expansion phase, the topology of the magnetic field in the magnetotail changes back to dipole-like. This corresponds to the global release of energy which was previously stored in the stretched magnetic field lines. The dipolarization of the magnetic field and decay of auroral activity brings the magnetosphere into its initial state. Usually, this takes 1-2 hours and is called the recovery phase of the substorm.

Several models have been proposed to explain substorm onset. Let us briefly cite some of them. Detailed descriptions and comparisons of different substorm models can be found, for example, in the recent review by *Elphinstone et al.* [1996]

There are models in which the substorm onset origin is placed at the PSBL or in the LLBL/PS interface region. *Rostoker and Eastman* [1987] proposed that

substorm onset is driven by the KH instability at the PSBL as a result of ions streaming along the boundary. Recently, *Rostoker* [1996] developed a model in which the KH instability occurs in the LLBL/PS interface region as a result of inner PS disturbances. A similar boundary layer model was proposed by *Maltsev and Lyatsky* [1984]. They suggested surface waves on the PSBL as a source for the initial perturbation. This model suggests that substorm onset occurs due to the growth of waves on the PSBL surface and their subsequent interaction with the plasma sheet.

KH instability as a possible mechanism for substorm triggering was proposed also by *Lui et al.* [1982]. *Lui et al.* [1982] suggested that the strong large scale ( $\sim 100$  km) shear flows may be responsible for the undulations of the diffuse aurora edge. These flows appear and grow during the substorm growth stage [*Kelley*, 1986].

Some other models propose reconnection in the distant magnetotail ( $\sim 30 R_E$ ) as the origin of substorm onset. These models are motivated by observations of the splitting of poleward arcs which were interpreted as signatures of the reconnection [*Hones et al.*, 1985; *Atkinson et al.*, 1989]. These models suggest that the source is situated far from the Earth and that the perturbation streams Earthward, carrying magnetic field lines, ion fluxes, and field aligned currents.

Ionosphere - magnetosphere coupling models [*Rothwell et al.*, 1984; *Kan and Sun*, 1985; *Lysak*, 1991] suggest that enhanced convection and the intensification of a pre-existing discrete arc are sufficient conditions for resonance between bouncing Alfvén waves and convection perturbations imposed by the ionospheric electric field in the vicinity of arcs.

The idea that onset is located at the inner edge of the plasmashet has a long history (see for example [*Atkinson*, 1967; *Lui*, 1991]) but the lack of information

about the processes and plasma parameters in this region did not allow to construct any quantitative models. However, the first spacecraft measurements at  $\sim 10 R_E$  magnetotail [*Roux et al.*, 1991; *Kistler et al.*, 1992; *Sergeev et al.*, 1993] supported by observations from geostationary orbits [*Lopez and Lui*, 1990; *Lui et al.*, 1992] revived these ideas and provoked the series of near-Earth onset substorm models.

Near-earth reconnection or tearing mode mechanisms were proposed to explain the dipolarization of the near-earth magnetotail and tailward ion fluxes [*Shindler*, 1974; *Buchner and Zelenyi*, 1987; *Baker and McPherron*, 1990]. These models assume that a local plasma resistivity may initiate a local tearing mode which would subsequently couple to a global mode (for example drift modes or SAWs) and activate large scale reconnection [*Jacquey et al.*, 1991; *Ohtani et al.*, 1992; *Baker et al.*, 1993].

Another group of models propose an initial disruption of the cross-tail current [*Lui et al.*, 1988; *Lui et al.*, 1992] as a necessary and sufficient condition of a substorm onset. The reduction of the current or electric field may be caused by external factors (for example, the turning of IMF to the north or sudden change in  $B_y$  of IMF) as well as due to the local turbulence or the waves discussed above.

Recently, *Lyons* [1995] showed that even a reduction in the large scale magnetotail electric field, caused for instance by a decrease in the  $B_z$  component of the IMF, may lead to a disruption of the magnetotail current and the initiation of active auroras. Some other observations and theories also suggest that a reduction of the southward IMF (or northward revers of the IMF  $B_z$  component) can initiate an onset [*Forster et al.*, 1971; *Kokubun et al.*, 1977; *Rostoker*, 1983; *Sergeev et al.*, 1986; *Lui et al.*, 1991; *Lyatsky*, 1996].

*Roux et al.* [1991] and *Holter et al.* [1995] interpreted the perturbations



observed by the geostationary satellite GEOS 2 as a ballooning mode which can arise from the instability of the equilibrium between pressure gradient and magnetic curvature. This idea launched various arguments as to whether the ballooning instability can develop in the inner plasma sheet despite the global stability of this region with respect to pressure perturbations [*Ohtani and Tamao*, 1993] and whether the pressure anisotropy is required for the instability to develop [*Chan et al.*, 1994]. We shall discuss these problems in more detail in chapters 4 and 5.

We should mention, that substorm onset is the subject of intense debates among physicists. Therefore, none of the above cited models can be considered to be generally accepted or rejected by the scientific community.

As seen from this brief review of different substorm onset models, some of them suggest that SAWs, shear flow instabilities and modes which can grow due to the stretched magnetic field line topology can play important role in substorm onset triggering. Therefore, understanding of linear and nonlinear evolution of these modes is relevant to the problem of substorm onset. Theoretical study of these modes and their coupling is the subject of this work.

#### **1.4.5 Field Line Resonances in the Earth's Magnetosphere**

As mentioned in section 1.3.4, FLRs can play an important role in energy storage in the inner magnetosphere. The scenario of FLRs in the Earth's magnetosphere was proposed by *Chen and Hasegawa* [1974] and *Southwood* [1974]. They suggested that initial perturbations in the form of surface waves driven by the KH instability may appear on the magnetopause. If surface waves are monochromatic, they

excite a monochromatic compressional fast mode which propagates inside the magnetosphere. Because of the Earthward gradient of Alfvén velocity, this wave becomes evanescent at the turning point and excites SAWs at the resonant point. The schematic of the FLRs is shown in Figure 1.9.

Observations of SAWs in the resonant regions show that FLRs repeatedly occur with the same discrete set of frequencies. These frequencies appear to be independent on local time, solar and magnetospheric activity, etc. Resonances are most commonly observed at 1.3, 1.9, 2.6, and 3.3 mHz which are called the “magic” frequencies. Results of ground-based and satellite observation can be found in [Walker and Greenwald, 1981; Tian *et al.*, 1991; Ruohoniemi *et al.*, 1991; Samson *et al.*, 1992a; Fenrich *et al.*, 1995; Potemra and Blomberg, 1996].

In order to explain the discrete set of FLR frequencies, Kivelson *et al.* [1984] suggested a magnetospheric cavity model. In this model, fast compressional waves propagate in a cavity bounded by the inner turning point and the magnetopause. This model was further developed by Samson *et al.* [1992a] and Wright [1994] who suggested a wave-guide mode with open azimuthal boundaries. This model takes into account azimuthal propagation of fast modes.

Recently, Xu *et al.* [1993] and Samson *et al.* [1996a] discovered that the discrete arc (see the next section) emissions are modulated with the same frequencies as large amplitude SAW in the regions of FLRs. Indeed large amplitude Alfvén waves have been observed above discrete arcs. These results suggest that discrete arcs may result from Alfvén resonances. Samson *et al.* [1996a,b; 1998] proposed a model which can lead to the generation and intensification of discrete auroral arcs in FLR regions. The overall scenario of the energy transfer in the Earth’s magnetosphere according to Samson *et al.* [1996a,b; 1998] is as follows: perturbations in the solar

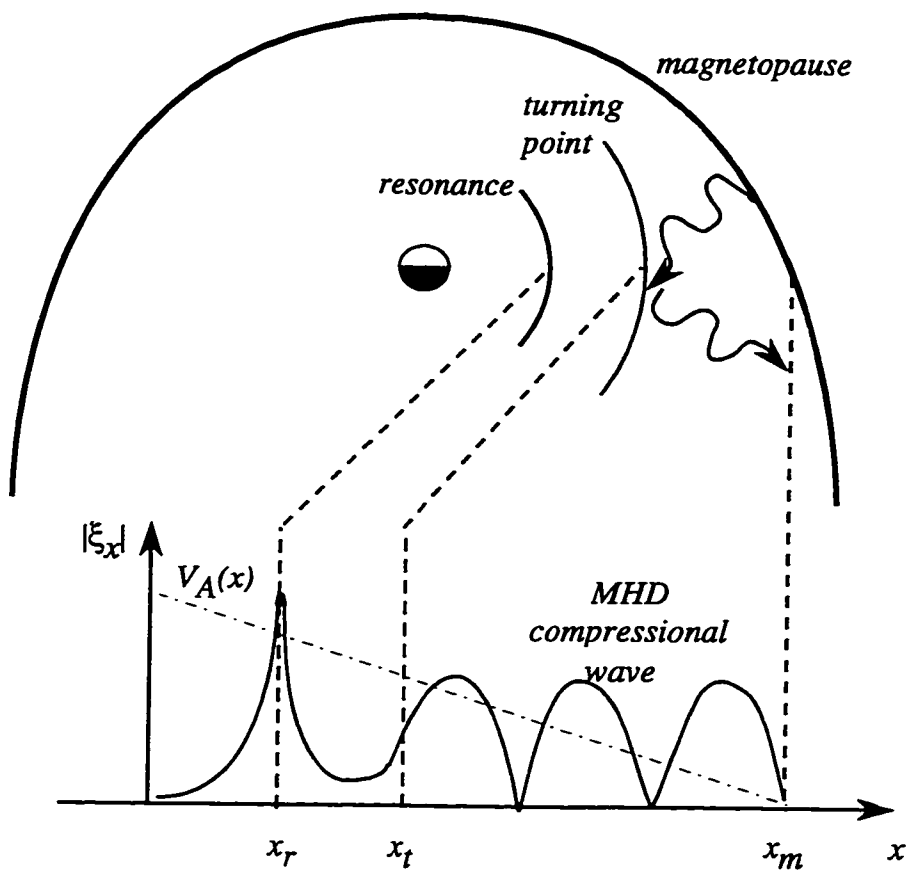


Figure 1.9: Schematic of FLRs in the Earth's magnetosphere.

wind pressure and magnetic field excite global quasi-monochromatic oscillations corresponding to compressional wave eigenmodes trapped in the magnetospheric waveguide. Because of very rare particle collisions, these waves may persist for long time periods so that the main mechanism for their dissipation will involve their resonant transformation into a SAW. The excited FLRs are localized near particular magnetic L-shells at which there will appear a spatial concentration of the SAW energy. The further structuring of the FLR region may occur due to the electron inertia effect. *Streltsov and Lotko* [1996; 1997] showed that the electron inertia leads to the appearance of narrow structures with the radial width of the order of the electron skin depth which is comparable with the discrete arc thickness.

In this work, the model of FLRs was further developed to study the nonlinear evolution of FLRs in the dipolar magnetosphere. The results of this study are presented in chapter 3.

#### 1.4.6 Auroral Arcs

An auroral arc is usually visible with the naked eye as an azimuthally extended green band with a width of about a few kilometers. The brightest arcs are typically observed in the evening and midnight sectors of the auroral oval.

Rocket experiments have shown that the luminosity is caused by electron beams accelerated to 1-10 keV (e.g., [*McIlwain*, 1960; *Evans*, 1968; *Frank and Ackerson*, 1971; *Arnoldy*, 1974]). Many experiments suggest that the beams are produced by field-aligned potential drops above the ionosphere [*Gurnett and Frank*, 1973; *Evans*, 1974; *Lyons et al.*, 1979], although the origin of these drops is not yet established (see review by *Lysak* [1990]). In order to obtain the observed electron spectra, the potential difference should be of the order of thousands of volts. Such

potential drops have been observed above arcs [*Gurnett and Frank*, 1973; *Evans et al.*, 1977; *Maynard et al.*, 1977]. Most experiments suggest that this accelerating region takes place at  $\sim 1R_E$  above the ionosphere [e.g., *Mozer et al.*, 1977]. However, the similar electrostatic shocks were also observed at altitudes of  $2 - 3R_E$  as well as at  $\sim 1000$  km above the ionosphere [*Mozer*, 1981; *Heppner et al.*, 1981]. The meridional thickness of the potential drops (named inverted V structures) is typically of the order of tens of kilometers.

*Lysak and Carlson* [1981] suggested that near the ionosphere, Alfvén velocity decreases due to the significant growth of plasma density. This forms a cavity which can play a role of an Alfvénic resonator for short Alfvén waves [*Trakhtengerts and Feldstein*, 1984, 1991; *Lysak*, 1988, 1991]. These waves are able to accelerate both electrons and ions, however different mechanisms of wave-particle interactions in this region have been suggested, and it is not yet clear which one dominates [*Goertz and Boswell*, 1979; *Tiwari and Rostoker*, 1984; *Trakhtengerts and Feldstein*, 1991; *Lysak*, 1991; *Li and Temerin*, 1993; *Mishin and Förster*, 1995; *Knudsen*, 1996].

Recent progress in the techniques for measuring arc thicknesses has demonstrated that the most narrow auroral structure (small scale arc) has a width of only about 100 m [*Borovsky*, 1993; *Trondsen and Cogger*, 1997; 1998; *Trondsen et al.*, 1997]. According to *Borovsky* [1993], several narrow arcs can appear in a group to form a system of arcs with a thickness of the order of kilometers. This group is typically embedded in an area of weaker emissions ( $\geq 10$  km) which is a manifestation of an electron accelerating region.

Electrodynamical features of large scale (several kilometers wide) arcs have been studied in numerous rocket and ground based experiments and may be summarized as follows. A region of auroral luminosity is associated with an upward

FAC sheet. Part of this current is carried by accelerated electrons. Within the arc, the electric field is extremely small. However this electric field can be significantly increased at the edges of the arc where the upward FAC sheet is replaced by a downward FAC [Lyons, 1981; Bruning and Goertz, 1986]. The structure of the FACs and electric fields suggests that the upward and downward FACs form a current circuit which is closed by Pedersen currents flowing across the arc. Since the conductivity is high in the region of the upward FAC the total ionospheric electric field is reduced within the arc and enhanced in the region of the downward FAC. These electric fields can modify convective flows and initiate shear flows along arcs. Such shear flows of the thickness of tens of kilometers have been repeatedly observed in association with discrete arcs [Carlson and Kelley, 1977; Bruning and Goertz, 1986; Haerendel et al., 1996]. These flows can be unstable with respect to the KH instability which results in the vortex formation [Haerendel et al., 1996; Miura, 1996]. Such vortex streets (called curls, folds and spirals according to Hallinan [1976]) are often seen in association with discrete arcs during the periods of enhanced auroral activity [Hallinan and Davis, 1970; Hallinan, 1976; Haerendel et al., 1996].

Another source for the shear flow instability in the auroral region was suggested by Rankin et al. [1993a] and Samson et al. [1996a]. Samson et al. [1996a] showed that some discrete auroral arcs are modulated with frequencies corresponding to field line resonances (FLRs). This implies that large amplitude shear Alfvén waves which grow in the FLR regions may be responsible for arc formation. On the other hand, FLRs evolve into a narrow channel which may eventually become unstable with respect to the shear flow mode. In this case, vortices should periodically change the direction of rotation. Such vortices have been recently observed in the midnight sector in association with high- $m$  FLRs [Fenrich, 1997].

Optical observations of the auroral curls have revealed that the motion of optical images does not agree with the  $\mathbf{E} \times \mathbf{B}$  plasma drift in the ionosphere [*Haerendel et al.*, 1993, 1996; *Frey et al.*, 1996]. According to the idea by *Davis* [1978], the motion of the auroral images may reflect a plasma motion above the ionosphere at the altitude of the electron acceleration region. However this difference between the convection patterns at different altitudes has not yet been explained.

The mechanism responsible for the generation of discrete arcs is still not known. A comparative review of different theories can be found in *Borovsky* [1993]. The key problem in the study of discrete arcs is to determine what source of energy drives the process. The most intriguing fact is that arcs do not appear to be the footprints of any well defined magnetospheric boundaries or discontinuities. This means that the energy must be extracted from ambient plasmas and then concentrated in the narrow region.

## 1.5 Thesis Outline

In this study, we shall develop the theory of nonlinear evolution and coupling of MHD waves and modes associated with discrete arcs. A computer code has been developed which allowed us to solve the entire set of one-fluid MHD equations in dipolar coordinates. Governing equations, the numerical method, and essentials of the computer program are described in chapter 2. The computer code was used to study the nonlinear evolution of SAWs in FLR regions. We show that FLRs provide high energy concentration in a radially narrow region. Also, we have found that FLRs on dipolar magnetic field lines lead to nonlinear coupling of SAW and slow magnetosonic modes. In the nonlinear stage, this coupling is responsible for the FLR saturation. Owing to the nonuniform field-aligned distribution of the plasma

density and magnetic field, nonlinear SAWs excite a wide spectrum of slow magnetosonic modes which can be proposed as a candidate mechanism for plasma heating. All these results are described in chapter 3. FLRs and field-aligned currents associated with discrete arcs lead to appearance of shear flows which have been repeatedly observed. Therefore, we have considered the evolution of the KH mode as an origin of vortices seen in auroral arc structures. As a possible source of additional potential energy, we propose the coupling of shear flows with ballooning modes. These problems are the subject of chapters 4 and 5. Chapter 6 gives a summary of the thesis.



## CHAPTER 2

### Alternative Direction Implicit (ADI) Method for MHD Equations

#### 2.1 MHD Equations in Curvilinear Coordinates

In magnetospheric plasmas, there are two major forces acting on ions: thermodynamic pressure  $-\nabla P$  and the Lorentz force  $(1/c)\mathbf{j} \times \mathbf{B}$ . Providing  $(4\pi/c)\mathbf{j} = \nabla \times \mathbf{B}$  is valid in the low frequency approximation, a set of one fluid MHD equations can be derived in the form:

$$\frac{1}{c} \frac{\partial \mathbf{B}}{\partial t} + \nabla \times \left( -\frac{1}{c} \mathbf{V} \times \mathbf{B} + \frac{c\eta}{4\pi} \nabla \times \mathbf{B} \right) = 0, \quad (2.1)$$

$$\rho \frac{d\mathbf{V}}{dt} + \nabla P - \frac{1}{4\pi} (\nabla \times \mathbf{B}) \times \mathbf{B} = 0, \quad (2.2)$$

$$\frac{\partial \rho}{\partial t} + \nabla \cdot (\rho \mathbf{V}) = 0, \quad (2.3)$$

$$\frac{\partial P}{\partial t} + \nabla \cdot (\gamma P \mathbf{V}) - (\gamma - 1) \left( \mathbf{V} \cdot \nabla P + \frac{c^2 \eta}{16\pi^2} |\nabla \times \mathbf{B}|^2 \right) = 0. \quad (2.4)$$

As discussed in chapter 1, for these equations, we used Ohm's law in the form  $\eta \mathbf{j} = \mathbf{E} + (1/c)\mathbf{V} \times \mathbf{B}$  neglecting Hall term, electron pressure and electron inertia.

In numerical procedures, it is more convenient to solve a momentum flux equation instead of the equation of motion (2.2). A flux equation is obtained if we combine the equation of motion (2.2) and the continuity equation (2.3), leading to:

$$\frac{\partial \rho \mathbf{V}}{\partial t} + \nabla \cdot (\rho \mathbf{V} \wedge \mathbf{V}) = -\nabla P + \frac{1}{4\pi} (\nabla \times \mathbf{B}) \times \mathbf{B}, \quad (2.5)$$

where  $\wedge$  is a dyadic product.

In order to normalize the set of MHD equations (2.1), (2.3)-(2.5), let us introduce nondimensional variables:

$$\mathbf{r}' = \frac{\mathbf{r}}{a}; \quad t' = \frac{t}{t_a}; \quad \mathbf{B}' = \frac{\mathbf{B}}{B_0}; \quad \mathbf{V}' = \frac{\mathbf{V}}{V_{A0}}; \quad \rho' = \frac{\rho}{\rho_0}; \quad P' = \frac{P}{P_0}; \quad \eta' = \frac{\eta}{\eta_0},$$

where  $a$  is a characteristic size of the system,  $B_0$  is a characteristic ambient magnetic field,  $\rho_0$  is a characteristic ambient density,  $V_{A0} = [B_0^2/(4\pi\rho_0)]^{1/2}$  is the characteristic Alfvén speed,  $t_a = a/V_{A0}$  is the Alfvén transit time,  $P_0 = B_0^2/(8\pi)$ , and  $\eta_0$  is an ambient resistivity.

In nondimensional variables, the set of MHD equations becomes

$$\frac{\partial \mathbf{B}}{\partial t} + \nabla \times \left( -\mathbf{V} \times \mathbf{B} + \frac{\eta}{\Re} \nabla \times \mathbf{B} \right) = 0, \quad (2.6)$$

$$\frac{\partial \rho \mathbf{V}}{\partial t} + \nabla \cdot (\rho \mathbf{V} \wedge \mathbf{V}) + \frac{1}{2} \nabla P + \mathbf{B} \times (\nabla \times \mathbf{B}) = 0, \quad (2.7)$$

$$\frac{\partial \rho}{\partial t} + \nabla \cdot (\rho \mathbf{V}) = 0, \quad (2.8)$$

$$\frac{\partial P}{\partial t} + \nabla \cdot (\gamma P \mathbf{V}) - (\gamma - 1) \left( \mathbf{V} \cdot \nabla P + \frac{2\eta}{\Re} (\nabla \times \mathbf{B})^2 \right) = 0, \quad (2.9)$$

where  $\Re = 4\pi a V_A / (c^2 \eta_0)$  is the magnetic Reynolds number. Here, the prime symbols are omitted for simplicity.

In the curvilinear orthogonal coordinates  $(x_1, x_2, x_3)$ , an element of a line is  $dl^2 = \sum_n h_n^2 (dx_n)^2$ , where  $h_1, h_2, h_3$  are the scale factors or metric. They can be found using the relations between the curvilinear  $(x_n)$  and cartesian  $(X_m)$  coordinates:

$$h_n^2 = \sum_m \left( \frac{\partial X_m}{\partial x_n} \right)^2. \quad (2.10)$$

In the curvilinear orthogonal coordinate system, the MHD equations can be written as follows:

$$\begin{aligned} & \frac{\partial B_1}{\partial t} + \frac{1}{h_2 h_3} \left( \frac{\partial}{\partial x_2} \left\{ h_3 \left[ B_1 V_2 - B_2 V_1 - \frac{\eta}{\Re} \frac{1}{h_1 h_2} \left( \frac{\partial}{\partial x_2} (h_1 B_1) - \frac{\partial}{\partial x_1} (h_2 B_2) \right) \right] \right\} \right. \\ & \left. + \frac{\partial}{\partial x_3} \left\{ h_2 \left[ B_1 V_3 - B_3 V_1 - \frac{\eta}{\Re} \frac{1}{h_1 h_3} \left( \frac{\partial}{\partial x_3} (h_1 B_1) - \frac{\partial}{\partial x_1} (h_3 B_3) \right) \right] \right\} \right) = 0; \quad (2.11) \end{aligned}$$

$$\begin{aligned} & \frac{\partial B_2}{\partial t} + \frac{1}{h_1 h_3} \left( \frac{\partial}{\partial x_1} \left\{ h_3 \left[ B_2 V_1 - B_1 V_2 - \frac{\eta}{\Re} \frac{1}{h_1 h_2} \left( \frac{\partial}{\partial x_1} (h_2 B_2) - \frac{\partial}{\partial x_2} (h_1 B_1) \right) \right] \right\} \right. \\ & \left. + \frac{\partial}{\partial x_3} \left\{ h_1 \left[ B_2 V_3 - B_3 V_2 - \frac{\eta}{\Re} \frac{1}{h_2 h_3} \left( \frac{\partial}{\partial x_3} (h_2 B_2) - \frac{\partial}{\partial x_2} (h_3 B_3) \right) \right] \right\} \right) = 0; \quad (2.12) \end{aligned}$$

$$\frac{\partial B_3}{\partial t} + \frac{1}{h_1 h_2} \left( \frac{\partial}{\partial x_1} \left\{ h_2 \left[ B_3 V_1 - B_1 V_3 - \frac{\eta}{\Re} \frac{1}{h_1 h_3} \left( \frac{\partial}{\partial x_1} (h_3 B_3) - \frac{\partial}{\partial x_3} (h_1 B_1) \right) \right] \right\} \right.$$

$$+\frac{\partial}{\partial x_2} \left\{ h_1 \left[ B_3 V_2 - B_2 V_3 - \frac{\eta}{\Re} \frac{1}{h_2 h_3} \left( \frac{\partial}{\partial x_2} (h_3 B_3) - \frac{\partial}{\partial x_3} (h_2 B_2) \right) \right] \right\} = 0; \quad (2.13)$$

$$\begin{aligned} \frac{\partial \rho V_1}{\partial t} + \frac{1}{h_1 h_2 h_3} \left\{ \frac{\partial}{\partial x_1} (h_2 h_3 \rho V_1^2) + \frac{\partial}{\partial x_2} (h_1 h_3 \rho V_1 V_2) + \frac{\partial}{\partial x_3} (h_1 h_2 \rho V_1 V_3) + h_3 \rho V_1 V_2 \frac{\partial h_1}{\partial x_2} \right. \\ \left. + h_2 \rho V_1 V_3 \frac{\partial h_1}{\partial x_3} - \left( h_3 \rho V_2^2 \frac{\partial h_2}{\partial x_1} + h_2 \rho V_3^2 \frac{\partial h_3}{\partial x_1} \right) \right\} + \frac{1}{2 h_1} \frac{\partial P}{\partial x_1} \\ + \left\{ \frac{B_2}{h_1 h_2} \left[ \frac{\partial}{\partial x_1} (h_2 B_2) - \frac{\partial}{\partial x_2} (h_1 B_1) \right] + \frac{B_3}{h_1 h_3} \left[ -\frac{\partial}{\partial x_3} (h_1 B_1) + \frac{\partial}{\partial x_1} (h_3 B_3) \right] \right\} = 0; \end{aligned} \quad (2.14)$$

$$\begin{aligned} \frac{\partial \rho V_2}{\partial t} + \frac{1}{h_1 h_2 h_3} \left\{ \frac{\partial}{\partial x_1} (h_2 h_3 \rho V_1 V_2) + \frac{\partial}{\partial x_2} (h_1 h_3 \rho V_2^2) + \frac{\partial}{\partial x_3} (h_1 h_2 \rho V_2 V_3) + h_3 \rho V_1 V_2 \frac{\partial h_2}{\partial x_1} \right. \\ \left. + h_1 \rho V_2 V_3 \frac{\partial h_2}{\partial x_3} - \left( h_3 \rho V_1^2 \frac{\partial h_1}{\partial x_2} + h_1 \rho V_3^2 \frac{\partial h_3}{\partial x_2} \right) \right\} + \frac{1}{2 h_2} \frac{\partial P}{\partial x_2} \\ + \left\{ \frac{B_3}{h_2 h_3} \left[ \frac{\partial}{\partial x_2} (h_3 B_3) - \frac{\partial}{\partial x_3} (h_2 B_2) \right] + \frac{B_1}{h_1 h_2} \left[ -\frac{\partial}{\partial x_1} (h_2 B_2) + \frac{\partial}{\partial x_2} (h_1 B_1) \right] \right\} = 0; \end{aligned} \quad (2.15)$$

$$\begin{aligned} \frac{\partial \rho V_3}{\partial t} + \frac{1}{h_1 h_2 h_3} \left\{ \frac{\partial}{\partial x_1} (h_2 h_3 \rho V_1 V_3) + \frac{\partial}{\partial x_2} (h_1 h_3 \rho V_2 V_3) + \frac{\partial}{\partial x_3} (h_1 h_2 \rho V_3^2) + h_2 \rho V_1 V_3 \frac{\partial h_3}{\partial x_1} \right. \\ \left. + h_1 \rho V_2 V_3 \frac{\partial h_3}{\partial x_2} - \left( h_2 \rho V_1^2 \frac{\partial h_1}{\partial x_3} + h_1 \rho V_2^2 \frac{\partial h_2}{\partial x_3} \right) \right\} + \frac{1}{2 h_3} \frac{\partial P}{\partial x_3} \\ + \left\{ \frac{B_1}{h_1 h_3} \left[ \frac{\partial}{\partial x_3} (h_1 B_1) - \frac{\partial}{\partial x_1} (h_3 B_3) \right] + \frac{B_2}{h_2 h_3} \left[ -\frac{\partial}{\partial x_2} (h_3 B_3) + \frac{\partial}{\partial x_3} (h_2 B_2) \right] \right\} = 0; \end{aligned} \quad (2.16)$$

$$\frac{\partial \rho}{\partial t} + \frac{1}{h_1 h_2 h_3} \left\{ \frac{\partial}{\partial x_1} (h_2 h_3 \rho V_1) + \frac{\partial}{\partial x_2} (h_1 h_3 \rho V_2) + \frac{\partial}{\partial x_3} (h_1 h_2 \rho V_3) \right\} = 0; \quad (2.17)$$

$$\begin{aligned}
& \frac{\partial P}{\partial t} + \frac{\gamma}{h_1 h_2 h_3} \left\{ \frac{\partial}{\partial x_1} (h_2 h_3 P V_1) + \frac{\partial}{\partial x_2} (h_1 h_3 P V_2) + \frac{\partial}{\partial x_3} (h_1 h_2 P V_3) \right\} - \\
& (\gamma - 1) \left( \left[ \frac{V_1}{h_1} \frac{\partial P}{\partial x_1} + \frac{V_2}{h_2} \frac{\partial P}{\partial x_2} + \frac{V_3}{h_3} \frac{\partial P}{\partial x_3} \right] + \frac{2\eta}{\Re} \left\{ \frac{1}{(h_2 h_3)^2} \left[ \frac{\partial}{\partial x_2} (h_3 B_3) - \frac{\partial}{\partial x_3} (h_2 B_2) \right]^2 + \right. \right. \\
& \left. \left. \frac{1}{(h_1 h_3)^2} \left[ \frac{\partial}{\partial x_3} (h_1 B_1) - \frac{\partial}{\partial x_1} (h_3 B_3) \right]^2 + \frac{1}{(h_1 h_2)^2} \left[ \frac{\partial}{\partial x_1} (h_2 B_2) - \frac{\partial}{\partial x_2} (h_1 B_1) \right]^2 \right\} \right) = 0.
\end{aligned} \tag{2.18}$$

## 2.2 Alternative Direction Implicit (ADI) Numerical Method for MHD Partial Differential Equations

The Alternative Direction Implicit (ADI) method is a finite difference numerical algorithm for two and three dimensional problems. The main idea of this method is to solve equations consecutively in each coordinate direction and to approach the solution using an iteration procedure.

In order to compute a solution using the ADI method, all terms involving spatial derivatives are sorted into three groups ( $F$ ,  $G$ ,  $H$ ) according to the direction of their leading derivatives. This allows us to divide a 3D spatial problem into a set of one-dimensional problems with the dependence between directions accounted for via an iterative procedure.

The evolution of the solution vector in time is computed using the Douglas-Gunn method [Douglas and Gunn, 1964; Finan and Killeen, 1981]. The time advance from time-step  $n$  to time-step  $n + 1$  can be achieved using two intermediate

temporal points  $n^*$  and  $n^{**}$  defined according to the following equations:

$$\frac{\mathbf{U}^{n^*} - \mathbf{U}^n}{\Delta t} + \frac{F(\mathbf{u}^{n^*}) + F(\mathbf{u}^n)}{2} + G(\mathbf{u}^n) + H(\mathbf{u}^n) = 0; \quad (2.19)$$

$$\frac{\mathbf{U}^{n^{**}} - \mathbf{U}^{n^*}}{\Delta t} + \frac{G(\mathbf{u}^{n^{**}}) + G(\mathbf{u}^n)}{2} = 0; \quad (2.20)$$

$$\frac{\mathbf{U}^{n+1} - \mathbf{U}^{n^{**}}}{\Delta t} + \frac{H(\mathbf{u}^{n+1}) + H(\mathbf{u}^n)}{2} = 0, \quad (2.21)$$

where  $\mathbf{u} \equiv \{\mathbf{B}, \mathbf{V}, \rho, P\}$  is a vector of dependant variables;  $\mathbf{U} \equiv \{\mathbf{B}, \rho\mathbf{V}, \rho, P\}$ ;  $\Delta t$  is the time step; and  $F$ ,  $G$ , and  $H$  include all terms with leading spatial derivatives in  $x_1$ ,  $x_2$ , and  $x_3$  directions, respectively. These derivatives are approximated using spatial finite differences which depend on the specific form of the terms. Such terms as  $\partial\alpha F/\partial x_1$  are called “flux” terms which can be approximated as  $\partial\alpha F/\partial x|_i = (\alpha_{i+1/2}F_{i+1/2} - \alpha_{i-1/2}F_{i-1/2})/(x_{i+1/2} - x_{i-1/2})$ , where all values at midpoints are defined as  $F_{i+1/2} = (F_{i+1} + F_i)/2$  and  $F_{i-1/2} = (F_{i-1} + F_i)/2$ . Terms which appear in the form  $\alpha\partial F/\partial x$  are called “force” terms. For them, the following approximation is applied:  $\alpha\partial F/\partial x|_i = (\alpha_{i+1/2}\delta F_{i+1/2} + \alpha_{i-1/2}\delta F_{i-1/2})/2$ , where  $\delta F_{i+1/2} = (F_{i+1} - F_i)/(x_{i+1} - x_i)$  and  $\delta F_{i-1/2} = (F_i - F_{i-1})/(x_i - x_{i-1})$  as illustrated by Figure 2.1.

Nonlinear terms in (2.11)-(2.18) can be calculated using a Taylor expansion (the so called Newton-Raphson method). If  $\mathbf{f} = \mathbf{f}(\mathbf{u})$  is a nonlinear term, its value at the  $l+1$  iteration can be computed using the value of  $\mathbf{f}$  from the previous iteration  $l$  and its Jacobians:

$$\mathbf{f}^{l+1} = \mathbf{f}^l + \left. \frac{\partial \mathbf{f}}{\partial \mathbf{u}} \right|_{\mathbf{u}^l} (\mathbf{u}^{l+1} - \mathbf{u}^l). \quad (2.22)$$

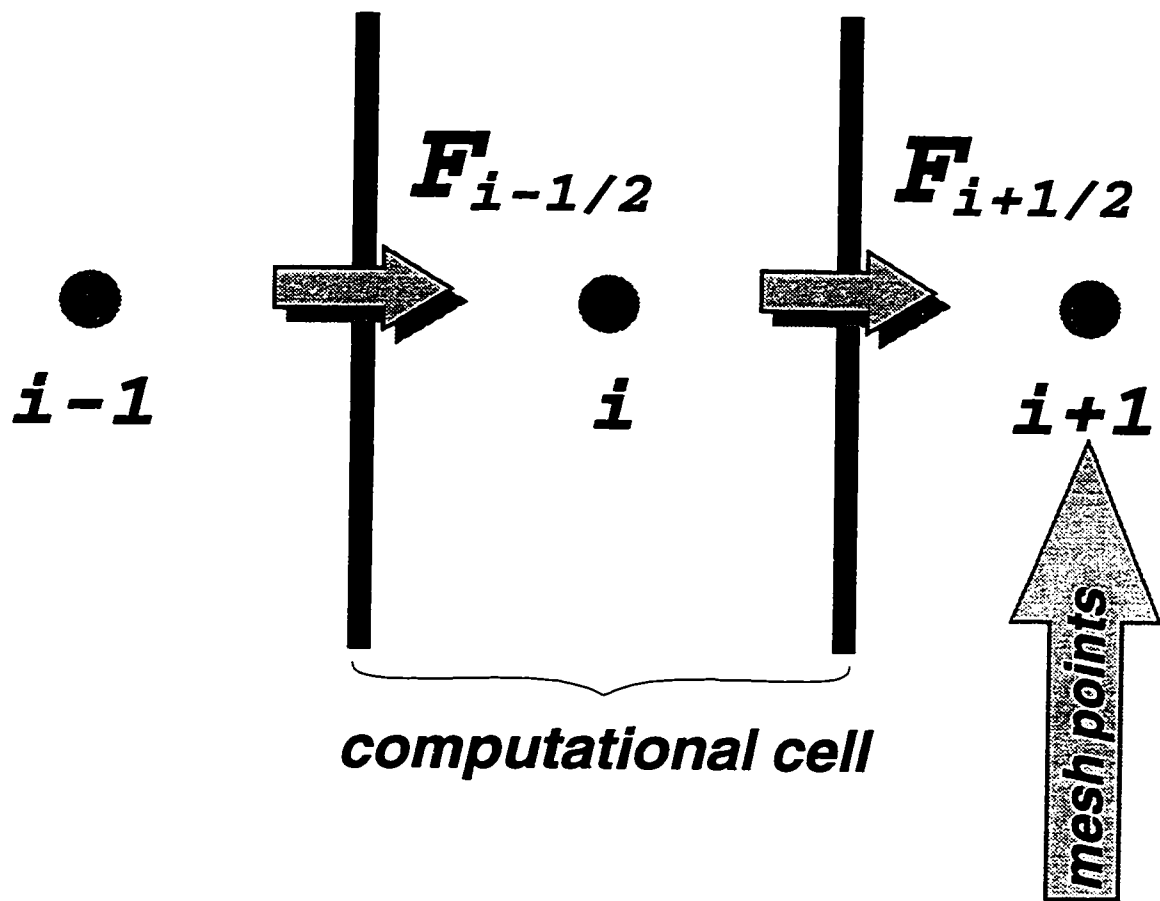


Figure 2.1: The schematic of a computational cell used in ADI.

Using the finite differences and the Newton-Raphson method (2.22) for non-linear terms and substituting  $F$ ,  $G$ , and  $H$  into (2.19), one can arrive at the set of equations in block-tridiagonal form:

$$\mathbf{D}_i = A_i \delta \mathbf{u}_{i-1} + B_i \delta \mathbf{u}_i + C_i \delta \mathbf{u}_{i+1}, \quad (2.23)$$

where  $\delta \mathbf{u}_i$  is an advance of  $\mathbf{u}_i^*$  at  $l + 1$  iteration:  $\mathbf{u}_i^* = \mathbf{u}_i^l + \delta \mathbf{u}_i$ . The  $8 \times 8$  matrices in (2.23) are formed from Jacobians as:

$$A_i = \frac{\Delta t}{2} \frac{\partial \mathbf{F}^m}{\partial \mathbf{u}_{i-1}^*}; \quad (2.24)$$

$$B_i = \frac{\Delta t}{2} \frac{\partial \mathbf{F}^m}{\partial \mathbf{u}_i^*} + \frac{\partial \mathbf{U}}{\partial \mathbf{u}_i^*}; \quad (2.25)$$

$$C_i = \frac{\Delta t}{2} \frac{\partial \mathbf{F}^m}{\partial \mathbf{u}_{i+1}^*}. \quad (2.26)$$

Vector  $\mathbf{D}$  can be found from:

$$\mathbf{D}_i = \mathbf{U}(\mathbf{u}_i) - \mathbf{U}(\mathbf{u}_i^l) - \frac{\Delta t}{2} [\mathbf{F}^m(\mathbf{u}_i^l) + 2\mathbf{F}^e(\mathbf{u}_i^l) + \mathbf{F}^m(\mathbf{u}_i)] - \Delta t [\mathbf{G}(\mathbf{u}_i) + \mathbf{H}(\mathbf{u}_i)], \quad (2.27)$$

where  $m$  and  $e$  indexes stand for implicit and explicit parts, respectively. In order to compute Jacobians for equations (2.11)-(2.18), we have developed a Mathematica routine that computes the  $8 \times 8$   $A, B, C$  matrices and generates output in Fortran form.

Equations (2.23) should be supplemented with boundary conditions. Then, they can be solved using a block-tridiagonal solver routine.



## 2.3 Boundary Conditions

In order to complete the matrix of coefficients  $A, B, C$  and the vector  $D$ , these coefficients must be defined at the boundary points. Below, we present three examples of the boundary conditions most often used in the ADI method.

1. Zero gradient of  $\mathbf{u}$  leads to the following equation at the boundary:  $B_1\delta\mathbf{u}_1 + A_1\delta\mathbf{u}_2 = 0$  and  $\delta\mathbf{u}_1 = \delta\mathbf{u}_2$ . Hence,  $B_1 = 1, A_1 = -1, D_1 = 0$ . The boundary condition for the last mesh point “ $n$ ” is  $B_n = 1, C_n = -1, D_n = 0$ .
2. Zero value condition at the boundary gives:  $B_1\delta\mathbf{u}_1 + A_1\delta\mathbf{u}_2 = 0$  with  $\delta\mathbf{u}_1 = -\delta\mathbf{u}_2$ . This requires:  $B_1 = 1, A_1 = 1, D_1 = 0$  and  $B_n = 1, C_n = 1, D_n = 0$ .
3. Periodic boundary conditions are:  $\delta\mathbf{u}_1 = \delta\mathbf{u}_{n+1}$ .

In the ADI code, usually we use a combination of different boundary conditions. For example, if a boundary is formed by a superconductive wall, it requires a zero value condition for the velocity and zero gradient condition for the tangential component of the magnetic field [Southwood and Hughes, 1983]. For non-conductive boundaries, the tangential magnetic field is zero at the boundary and the tangential components of velocity are defined by the zero gradient boundary conditions. Normal components of the magnetic field perturbation and velocity are zero at boundaries. In the azimuthal direction  $\phi$ , we assume the periodic boundary conditions for all problems considered in this thesis.

## 2.4 Numerical Diffusion

Even though the ADI method provides stability for the numerical linear solution, it may become unstable with respect to high frequency nonlinear modes. The stability of the nonlinear solution can be achieved if we add a small numerical viscosity term (also called numerical diffusion or advection) into the governing equations. The stability of the magnetic field terms can be ensured by using a small value of the resistivity exactly as it appears in (2.1). Numerical viscosity is added to the continuity, momentum, and energy equations. For example, a second order diffusion in the  $x_1$ -direction can be introduced as follows:

$$\frac{\partial \mathbf{u}}{\partial t} + \nabla \cdot [\mathbf{F}(\mathbf{u}) - C_{adv} \cdot \nabla \wedge \mathbf{u}] = 0, \quad (2.28)$$

where  $\wedge$  is a dyadic product for the momentum equations or a simple multiplication for the continuity and energy equations, and  $C_{adv}$  is a diffusion coefficient. This advection term is a “flux” term for the finite difference approximation.

When numerical diffusion coefficients and resistivity are chosen larger than is necessary to achieve stability, they can affect not only nonlinear but also linear solutions. In order to avoid this influence, the linear solutions can be tested using zero advection. In addition, test of energy conservation and estimates of the ratio of the advection terms to other terms are essential steps in order to obtain accurate solutions.

## 2.5 ADI Code in Parallel and Vector Computers

The ADI method applied to the MHD equations has the advantage that when the equations are being solved in one direction, say  $x_1$ , the solution depends on the  $x_2$  and  $x_3$  coordinates only explicitly. This means that the equations may be solved simultaneously for several or all  $x_2$  and  $x_3$  mesh points. This allows us to use parallel and vector computers quite efficiently for the ADI code.

The results presented in this thesis were obtained using the ADI code implemented on two machine architectures: the parallel-vector Stardent 3000 computer and the parallel Silicon Graphics, Inc. (SGI) Power CHALLENGE 10000 computer.

The parallelization and vectorization of the ADI code on the Stardent computer are illustrated in Figure 2.2. In this example, the equations are solved as a set of 1D problems in the  $x_1$  direction. Mesh points in the  $x_2$  and  $x_3$  directions are arranged into several groups (called "chunks") for parallel performance on different processors. Within each chunk, all mesh points are divided into subgroups called vector arrays. The number of mesh points supported by a vector array is 32 in the Stardent 3000 computer. The entire vector array is supplied for continuous performance.

The entire procedure can be further illustrated by Figure 2.3. In the example shown in this figure, the equations are solved in the  $x_1$ -direction whereas the total number of mesh points supplied for the parallel task is  $n_j \times n_k$ . Here  $n_j$  and  $n_k$  are the numbers of points in  $x_2$  and  $x_3$  directions, respectively. The entire mesh is divided into  $n_{cpu}$  groups which are assigned to different processors for parallel performance. During calculations, every processor specifies lower and upper mesh points of the entire task and divides it into vectoral units ( $n_{vect}$ ). Then, every

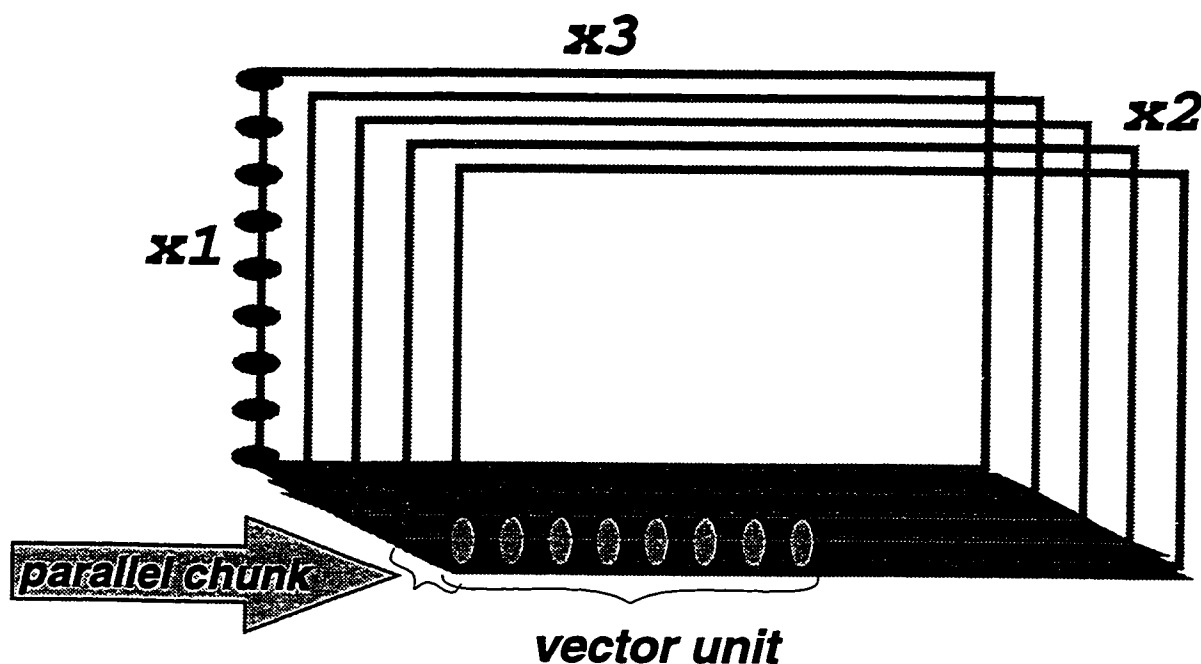


Figure 2.2: A schematic of the parallelization and vectorization of ADI.

routine uses these groups to compute them as continuous series (or in “pipelines”), which significantly increases performance.

The number of chunks should be chosen optimally for the criteria of achieving high performance and moderate memory consumption. This is illustrated in Figure 2.4 where the net processor time required for program completion is presented as a function of the number of points in a chunk. This test was completed using 4 processors in the Stardent 3000 computer. As seen from Figure 2.4, an increase of the number of mesh points in a chunk from 1 to 8 significantly improves the performance because it allows us to reduce the wall time by a factor of 5-6. The further increase of a chunk size is not justified because it barely reduces the performance time but raises the memory consumption.

There are no vector units in the SGI computer, so that the ADI code is

```

*
* The size of a chunk:
* nj*nk is the total number of mesh points in x2 and x3
* directions;
* ncpu is a number of chunks specified by a user
*
C$DOIT PPROC solvex
  isize = (nj*nk+ncpu-1)/ncpu
*
* Parallel task for all CPUs to run all chunks:
*
  do k = 1, ncpu
    call solvex((k-1)* isize, min(isize, nj*nk-(k-1)* isize))
  enddo
*

```

```

* Number of the element in the whole nj*nk sequence:
* note that "low" is the lower index of a chunk (0, isize, 2*isize, etc.)
* whereas "num" is the length of a chunk (either isize or "the remainder")
  do m = 1, num
    inx(m) = m + low
  enddo
*

```

```

* Call a subroutine for a vector performance:
* nvect is a vectoral length.
  do lm = 1, m, nvect
    lng = min(nvect, m-lm+1)
    call AAAAA(lng, inx(lm))
  end do
*

```

Figure 2.3: A diagram of the parallelization and vectorization in a FORTRAN version of ADI.

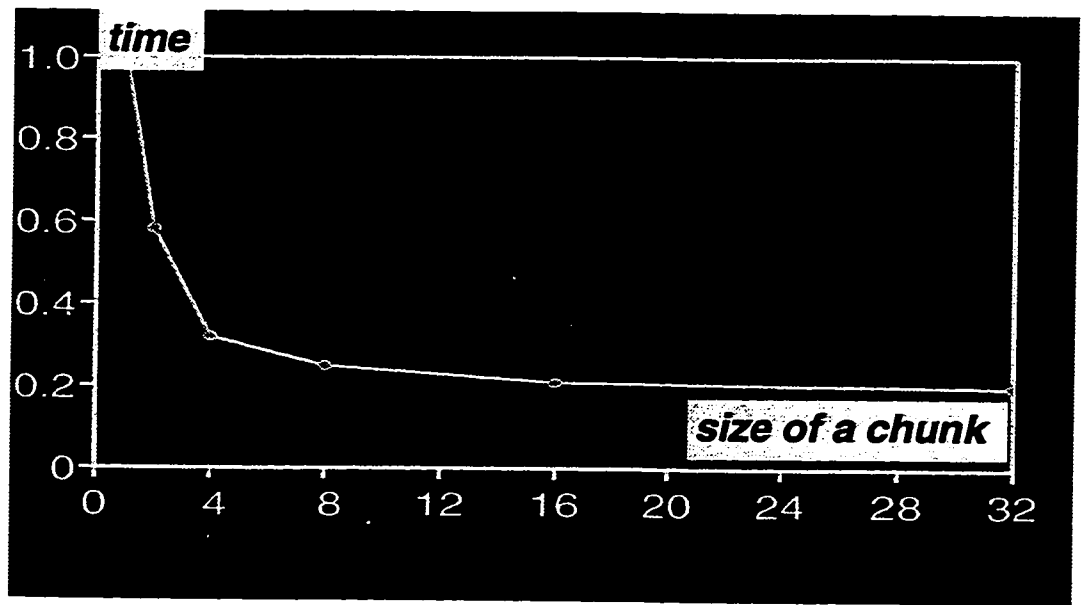


Figure 2.4: The normalized performance time as a function of the number of mesh points in a parallel chunk.

implemented only for parallel performance using the same parallel techniques as for the Stardent computer.

## CHAPTER 3

# Shear Alfvén Waves and Field Line Resonances in the Dipolar Magnetosphere

### 3.1 Preliminary Remarks

As discussed in chapter 1, standing SAWs play an important role in magnetospheric dynamics and provide a mechanism for energy transport from the magnetosphere to the ionosphere. These waves lead to a variety of geophysical phenomena. In particular, they are responsible for magnetic pulsations in the frequency range 0.5-5 mHz, called Pc5 pulsations [*Walker and Greenwald*, 1981; *Tian et al.*, 1991; *Potemra and Blomberg*, 1996]. Also, large amplitude SAWs are observed in association with discrete auroral arcs and substorm onsets [*Samson et al.*, 1996a; 1998].

Standing SAWs can be excited on closed magnetic field lines by localized velocity shear in the magnetosphere (as for example at the dayside LLBL), by ionospheric current perturbations, or due to field line resonances (FLRs) which couple SAW and fast modes. Standing SAWs involve oscillations of the entire magnetic field line and appear as fundamental modes of magnetic shells. If a SAW is excited by a fast mode driver with a frequency close to the SAW eigenfrequency on a particular L-shell, the growth of the SAW amplitude is referred to as an FLR.

As mentioned in chapter 1, the idea of FLRs was proposed by [*Southwood* 1974; *Chen and Hasegawa* 1974] who realized that FLRs can play an important

role in energy storage near a particular resonant magnetic  $L$ -shell in the Earth's magnetosphere. The interaction of the solar wind with the magnetopause initiates compressional fast modes, also called compressional Alfvén waves (CAWs), which propagate antisunward in a magnetospheric cavity. This cavity is produced by the reflecting magnetopause and turning points on dipole field lines close to the Earth [Samson *et al.*, 1992a]. CAWs couple to SAWs on dipole magnetic field lines just Earthward of the turning point. In the equatorial plane, these SAWs have nodes of the magnetic field perturbation and antinodes of the velocity and electric fields. Owing to large radial gradients in the Earth's magnetic field, SAWs are concentrated within an azimuthally stretched channel near the resonant point. This allows for energy accumulation in particular regions of the inner magnetosphere.

A particular class of large amplitude oscillations in the corresponding frequency range is often observed by satellites and by ground-based magnetometers and radars [Walker and Greenwald, 1981; Mitchell *et al.*, 1990; Tian *et al.*, 1991; Fenrich *et al.*, 1995; Potemra and Blomberg, 1996]. For example, velocities as large as 150-200 km/s were registered by satellites in the equatorial magnetosphere in association with large amplitude SAWs [Mitchell *et al.*, 1990].

A nonlinear FLR model has been proposed recently by Rankin *et al.* [1994, 1995]. In this model, the ponderomotive force in standing SAWs results in a redistribution of the background plasma density along the geomagnetic field line [Allan *et al.*, 1991; Allan, 1992, 1993a, b; Rankin *et al.*, 1994, 1995; Tikhonchuk *et al.*, 1995; Guglielmi, 1997; Voronkov *et al.*, 1997b]. This plasma density redistribution changes the SAW eigenfrequency, detunes the resonance, and periodically decouples the SAW from the CAW driver. The density perturbations along the magnetic field line can be considered as radially localized slow magnetosonic waves (SMWs) that are driven by the ponderomotive force. Therefore, the FLR saturation is a result



of the nonlinear coupling between SAWs, CAWs and SMWs. As demonstrated by *Rankin et al.* [1995], the SAW nonlinear frequency shift also results in latitudinal motion and narrowing of the FLR.

The nonlinear FLR model was originally developed using the geometry of straight magnetic field lines (box model) [*Rankin et al.*, 1994, 1995]. However, this model neglects the effects of plasma parallel inhomogeneity (and hence variations in plasma  $\beta$ ) and magnetic field line curvature, both of which might be expected to produce significant modifications to the FLR dynamics [*Allan*, 1993a].

In this chapter, we study the structure of SAWs and FLRs in the dipolar magnetosphere. A dipolar model of the Earth's magnetosphere with nonuniform density distribution is introduced in section 3.2. Structure of linear SAWs in the dipolar topology is described in section 3.3. We have developed a routine to find eigenfunctions and eigenfrequencies of linear SAW harmonics. These linear harmonics were used to test the ADI code with respect to steady oscillations. Further, the linear analysis of SAWs allowed us to study nonlinear effects of SAWs and their nonlinear evolution in FLR regions. The theory and numerical simulation results for the nonlinear evolution of FLRs in dipolar coordinates are presented in section 3.4. Our model describes the nonlinear coupling between driven SAW and SMW modes and accounts for several features that are not included in the previous box models: (1) We define the region of the most efficient coupling between the CAW and SAW and derive an analytical expression for the FLR amplitude which depends on the driver strength and shift between the driver oscillation frequency and SAW eigenfrequency. (2) In the box model, the field-aligned structure of SAW and SMW modes is identical. Therefore, the SAW couples only to the second spatial SMW harmonic. Conversely, in the dipolar model, the ponderomotive force drives

a wide spectrum of SMW eigenmodes which change the dynamics of the FLR saturation. (3) The dipolar model predicts such measurable quantities as spatial FLR structure, the period of pulsations, and the location and magnitude of the density perturbations. These results can be proposed as a guideline for experimental data analysis. The radial distribution of the velocity and field-aligned currents in the FLR region obtained using the ADI code is described in section 3.5. We show that in the equatorial plane, SAWs become radially structured within a narrow channel which allows for exciting of the KH instability with  $e$ -folding time smaller than a half period of SAWs. The radial distribution of the field-aligned currents above the ionosphere is compared with optical photometer data. The similarity in theoretical and observational patterns suggests that FLRs may be responsible for the excitation and poleward motion of discrete arcs.

## 3.2 Dipolar Model of the Earth's Magnetosphere

The dipolar magnetic field component is the main part of the total magnetic field of the Earth at distances less than approximately  $8 R_E$ , as illustrated by Figure 3.1. In this figure, the dipolar magnetic field is compared with the model magnetic field in the equatorial midnight magnetotail predicted by the T96 model [Tsyganenko, 1996] for low magnetic activity. At distances larger than  $8$ - $10 R_E$  from the Earth, the dipolar magnetic field becomes comparable with the magnetic field due to magnetospheric currents. However, for a large class of problems in magnetospheric physics, the dipolar topology remains a good approximation of the real topology.

In this section, we shall describe the dipolar model of the Earth's magnetosphere constructed on the basis of the ADI code and designated to solve the one fluid MHD equations in curvilinear dipolar coordinates.

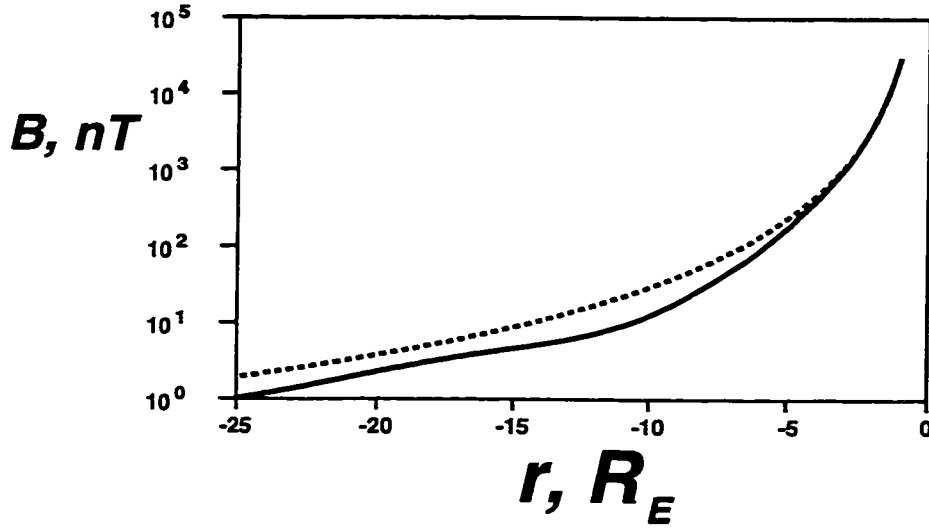


Figure 3.1: Magnetic field in the equatorial midnight magnetotail as predicted by the T96 model [Tsyganenko, 1996] (solid line) and dipolar magnetic field of the Earth (dashed line).

### 3.2.1 Dipolar Coordinates

Let us consider an equation for a dipolar field line:

$$r = r_0 \cos^2 \lambda, \quad (3.1)$$

where  $r$  is the distance from the centre of the Earth to the field line,  $r_0$  is the distance to the field line in the equatorial plane, and  $\lambda$  is latitude. The main elements of the dipolar topology are shown in Figure 3.2.

The length of the field line element  $dl$  is

$$dl^2 = dr^2 + r^2 d\lambda^2. \quad (3.2)$$

Integration gives a useful dependance for the field line length  $l$  as a function

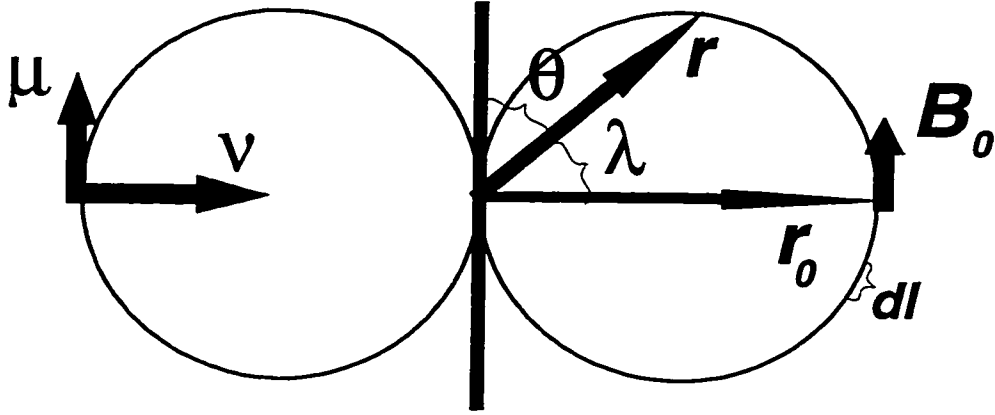


Figure 3.2: Elements of the dipolar topology.

of  $r_0$ :

$$l = \left(2 + \frac{\sqrt{3} \sinh^{-1}(\sqrt{3})}{3}\right) r_0 \approx 2.76 r_0. \quad (3.3)$$

Now let us introduce a coordinate system  $(\mu, \nu, \phi)$  where  $x_1 \equiv \mu$  is the field-aligned coordinate,  $x_2 \equiv \nu$  numerates magnetic shells in the direction perpendicular to the field line, and  $x_3 \equiv \phi$  is azimuthal. These coordinates can be described using relations between the dipolar topology and spherical  $(r, \theta, \phi)$  or cartesian  $(x, y, z)$  coordinates:

$$\mu = \cos\theta/r^2 = \frac{z}{\sqrt{(x^2 + y^2 + z^2)^3}}, \quad (3.4)$$

$$\nu = \sin^2\theta/r = \frac{x^2 + y^2}{\sqrt{(x^2 + y^2 + z^2)^3}}, \quad (3.5)$$

$$\phi = \tan^{-1} \frac{y}{x}. \quad (3.6)$$

The corresponding scale factors (metric) describe the transition between the dipolar and spherical or cartesian coordinate systems:

$$h_\mu = \frac{r^3}{(1 + 3\cos^2\theta)^{\frac{1}{2}}} = \frac{(x^2 + y^2 + z^2)^2}{(x^2 + y^2 + 4z^2)^{\frac{1}{2}}}, \quad (3.7)$$

$$h_\nu = \frac{r^2}{\sin\theta(1 + 3\cos^2\theta)^{\frac{1}{2}}} = \frac{(x^2 + y^2 + z^2)^2}{(x^2 + y^2)^{\frac{1}{2}}(x^2 + y^2 + 4z^2)^{\frac{1}{2}}}, \quad (3.8)$$

$$h_\phi = r \sin\theta = \sqrt{x^2 + y^2}. \quad (3.9)$$

### 3.2.2 Representation of the Earth's Dipolar Magnetic Field in the Dipolar Coordinates

The scale factor  $h_\mu$  allows a convenient representation of the dipolar magnetic field in the form  $B = M/h_\mu$ , where  $M$  is the magnetic dipole moment of the Earth which magnitude is  $8.02 \cdot 10^{25} \text{ G} \cdot \text{cm}^3$ .

When dealing with the dipolar geometry of the Earth's magnetic field, it is more convenient to express all lengths normalized by the Earth's radius. The value  $L = r_0/R_E$  is called McIlwain parameter which characterizes a shell of identical dipolar field lines called an  $L$ -shell. A graphical presentation of an  $L$ -shell is illustrated in Figure 3.3.

The total magnetic field can be represented in dipolar coordinates as  $\mathbf{B} = M/h_\mu \cdot \mathbf{e}_\mu + \mathbf{B}'$ , where  $\mathbf{e}_\mu$  is a unit vector of  $\mu$  and  $\mathbf{B}'$  is the deviation of the magnetic field from a purely dipolar one. In this work, we deal with cases for which  $\mathbf{B}'$  is oscillatory (as for the case of the Shear Alfvén Wave considered later in this

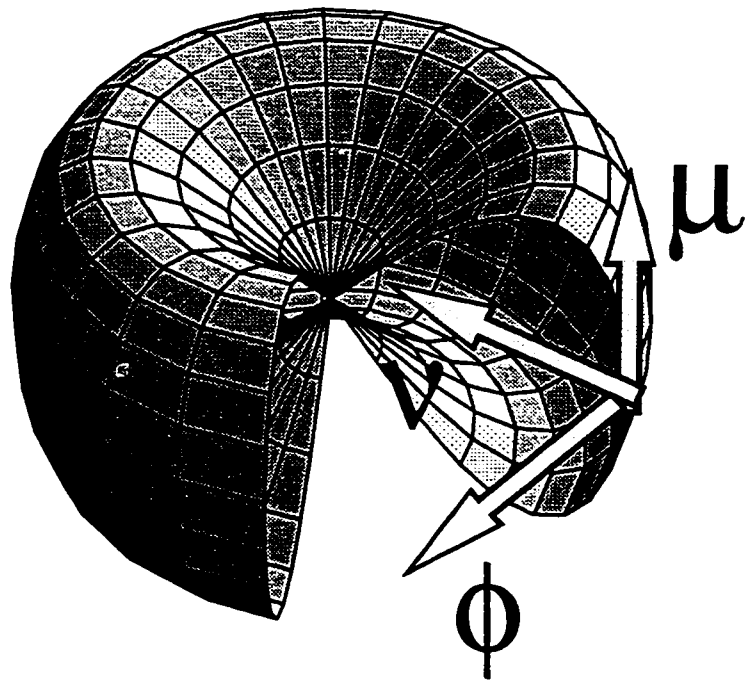


Figure 3.3: An  $L$ -shell of the Earth's dipolar magnetic field.

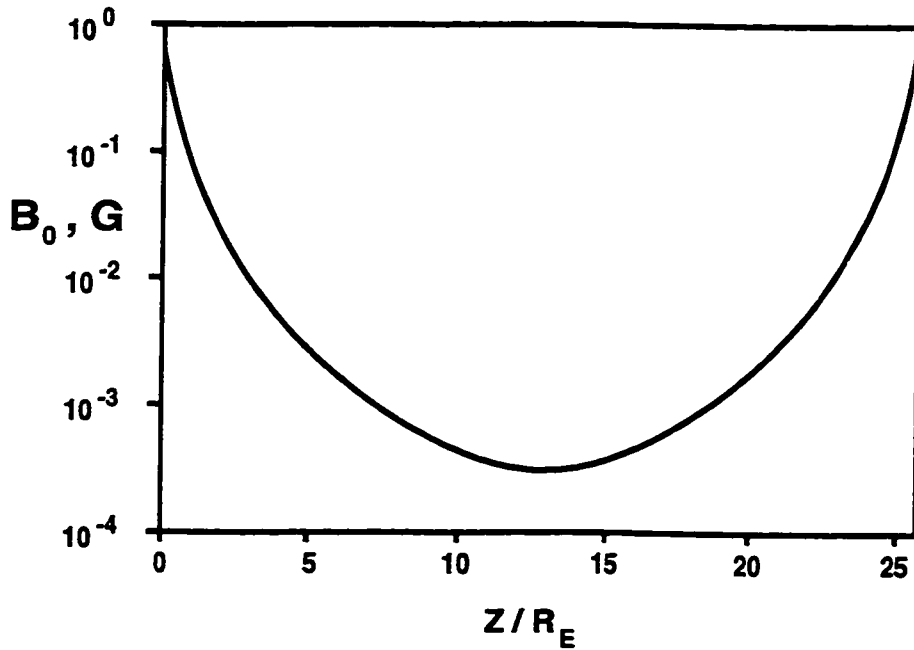


Figure 3.4: Variation of the dipolar magnetic field along the  $L = 10$  magnetic shell computed from  $B_0 = M/h_\mu$ . Here,  $Z$  is distance along magnetic field lines from the southern ionosphere to the northern ionosphere

chapter) and stationary (for example, the stretched topology of the total magnetic field modelled in chapter 5).

The value of the Earth's dipolar magnetic field varies as  $1/L^3$  in the equatorial plane, increasing Earthward. Also, it changes significantly along field lines. Variations of  $B$  along the magnetic field line at the  $L = 10$  shell are shown in Figure 3.4

### 3.2.3 Equilibrium of the Dipolar Magnetosphere

An equilibrium requires  $dV/dt = 0$  in the momentum equation. As can be seen from (2.5), the equilibrium condition is

$$-\nabla P + \frac{1}{4\pi}(\nabla \times \mathbf{B}) \times \mathbf{B} = 0 \quad (3.10)$$

For a dipolar magnetic field  $\mathbf{B} = B_\mu \mathbf{e}_\mu$ ,  $B_\mu h_\mu = M$  is constant which means that  $\nabla \times \mathbf{B} = 0$ . Then, from (3.10), equilibrium is defined as  $\nabla P = 0$ . Physically, this means that in the dipolar magnetic field, the magnetic pressure and curvature of the magnetic field lines are in balance, and hence plasma pressure must be uniform for equilibrium. If the magnetic field is nondipolar (as in the case for stretched magnetic field lines), the initial equilibrium pressure distribution changes according to (3.10). In this case, the equilibrium may be unstable with respect to ballooning and Alfvén ballooning modes. We shall consider this problem in Chapters 4 and 5.

### 3.3 Linear Shear Alfvén Waves in the Dipolar Magnetosphere

#### 3.3.1 Dispersion Relation for Linear SAWs

Below, we shall consider the structure of standing SAWs which results from solutions to the SAW dispersion relation. We assume that waves are toroidal which means that oscillations occur in the azimuthal direction. We shall consider only the low- $m$  (large wavelength) case for which we can neglect azimuthal dispersion and coupling with the poloidal components  $B_\nu$  and  $V_\nu$ . Discussion of these effects will be given at the end of this chapter.

Let us assume that there is an initial perturbation comprising of an azimuthal velocity component  $V_\phi$  and an azimuthal magnetic field  $B_\phi$ . Linearizing (2.1)-(2.4) and assuming that the resistivity and viscosity terms are negligible, one can obtain



linear equations describing a toroidal SAW:

$$\frac{\partial h_\phi B_\phi}{\partial t} - \frac{1}{h_\nu^2} \frac{\partial}{\partial \mu} (h_\nu V_\phi B_0) = 0, \quad (3.11)$$

$$\frac{\partial V_\phi}{\partial t} = \frac{B_0}{4\pi\rho h_\mu h_\phi} \frac{\partial h_\phi B_\phi}{\partial \mu}. \quad (3.12)$$

Combining them, we can derive a linear SAW equation for the magnetic field perturbation:

$$\frac{\partial^2 h_\phi B_\phi}{\partial t^2} - \frac{1}{h_\nu^2} \frac{\partial}{\partial \mu} \frac{V_{A0}^2}{h_\phi^2} \frac{\partial}{\partial \mu} h_\phi B_\phi = 0, \quad (3.13)$$

where  $V_{A0}^2 = B_0^2/4\pi\rho_0$  is the square of the background Alfvén speed and  $\mu$  varies from the lower,  $\mu_-$ , to the upper,  $\mu_+$ , end of the magnetic field line.

Equation 3.13 has a fundamental set of eigenmodes

$$h_\phi B_\phi = b_N e^{-i\omega_N t} S_N(\mu), \quad (3.14)$$

where  $b_N$ ,  $\omega_N$  and  $S_N(\mu)$  are the mode's amplitude, eigenfrequency and eigenfunction, respectively. Substitution of (3.14) in (3.13) and integration by parts result in the orthonormality equation for the eigenfunctions:

$$\int_{\mu_-}^{\mu_+} d\mu h_\nu^2 S_M S_N = \delta_{M,N}, \quad (3.15)$$

where  $\delta_{M,N}$  is the Kronecker delta function.

If the background magnetic field and density distributions are defined and boundary conditions for  $h_\phi B_\phi$  are prescribed, equations (3.13)-(3.15) allow us to find the set of SAW eigenfrequencies and eigenfunctions.

### 3.3.2 Eigenproblem for a Standing SAW in the Dipolar Magnetosphere

Standing SAWs appear as global oscillations of the entire magnetic field line. Therefore, the boundary conditions for these waves may be applied in the highly conductive ionospheric E-region. The conductivity across magnetic field lines in the ionosphere is much higher than in the magnetosphere. For simplicity, we assume that the magnetospheric plasma conductivity is zero across field lines and that the ionospheric boundaries are superconducting. In this case, the ionospheric electric field  $E_\nu = [V_\phi B_\mu]_{\mu+-} = 0$  which requires  $[V_\phi]_{\mu+-} = 0$ . The condition  $[dV_\phi/dt]_{\mu+-} = 0$  requires  $[d/d\mu(h_\phi B_\phi)]_{\mu+-} = 0$ . These boundary conditions signify that the velocity field has nodes whereas the magnetic field has antinodes at the ionosphere.

Below, we shall present the results of the numerical solution for the eigenproblem described by (3.13)-(3.15) with the boundary conditions prescribed above. A background density distribution was chosen as

$$\rho_0 = \rho_{eq}(1 - \cos \theta^2)^{-q}, \quad (3.16)$$

with  $\rho_{eq} = 1.044 \cdot 10^{-24} \text{ g/cm}^3$  and  $q = 4$ . The distribution of  $\rho_0$  along the magnetic field line and the corresponding field-aligned distribution of the Alfvén speed at  $L = 10$  are shown in Figures 3.5 a and b, respectively.

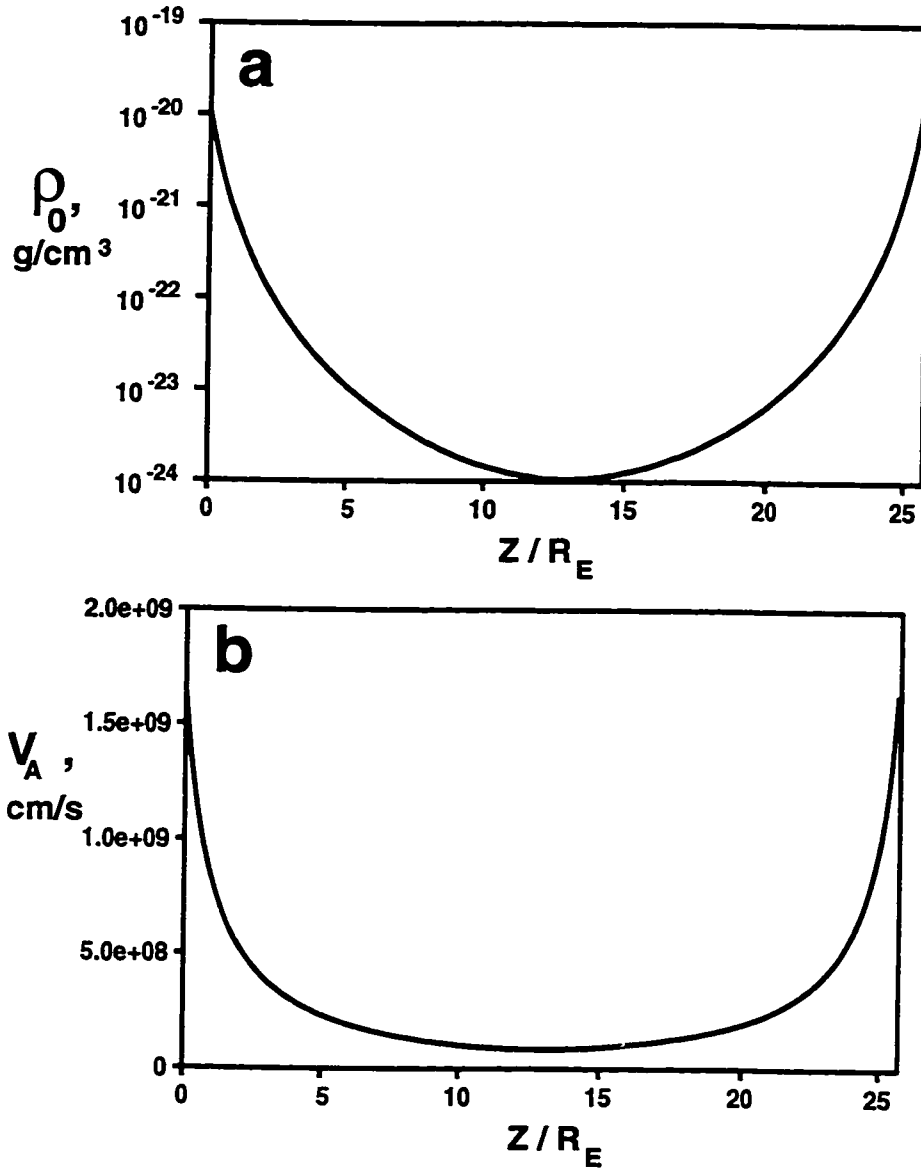


Figure 3.5: Distribution of (a) density and (b) Alfvén velocity along the  $L = 10$  magnetic field line.

Equation (3.16) prescribes a simplified large-scale model of the density distribution along the field line. Near the ionosphere, the plasma density grows significantly. This causes an abrupt decrease of the Alfvén velocity which leads to the formation of an ionospheric cavity [Lysak and Carlson, 1981]. This cavity plays a role of an Alfvénic resonator for short wavelength Alfvén waves [Trakhtengerts and Feldstein, 1984, 1991; Lysak, 1988, 1991]. However, the length of this resonator is approximately  $\sim 10^4$  km which is much smaller than needed for SAW harmonics. Therefore, we shall neglect this inhomogeneity and assume the density and Alfvén velocity distribution as shown in Figure 3.5.

After substitution of (3.14), (3.13) becomes:

$$\omega_N^2 S_N + \frac{1}{h_\nu} \frac{\partial}{\partial \mu} \frac{V_A^2}{h_\phi^2} \frac{\partial}{\partial \mu} S_N = 0. \quad (3.17)$$

The spatial derivatives in (3.17) can be approximated using finite differences and the eigenmode equation (3.17) can then be solved numerically through inversion of a tridiagonal matrix.

Figure 3.6 presents the field aligned distribution of  $h_\phi B_\phi$  (a) and  $V_\phi$  (b) for the first three harmonics of SAW at  $L = 10$ . The magnetic field is normalized by the boundary value of  $h_\phi B_\phi$ , whereas velocities are divided by the  $V_\phi$  value at the mid-line point. Variations of the SAW eigenfrequencies with  $L$ -shells for the same three SAW harmonics are shown in Figure 3.7. As expected, SAW frequencies change significantly with  $L$ -shell. This suggests that if a SAW is excited by an external monochromatic driver, the growth of SAWs would occur only in the vicinity of the particular  $L$ -shell where the driver frequency matches the local SAW frequency. This may result in the radial structuring of the large amplitude SAW regions. We shall consider this problem in the next section.

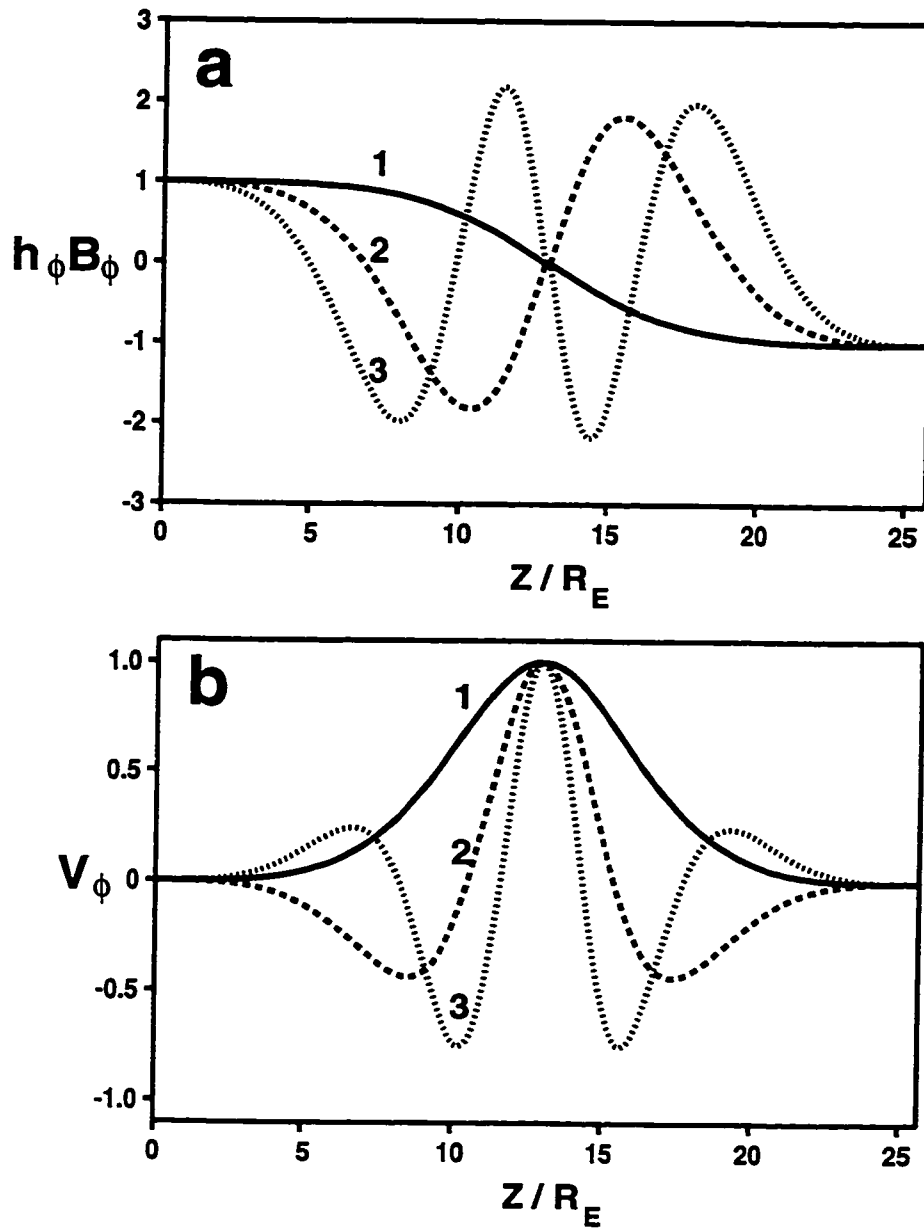


Figure 3.6: Distribution of (a)  $h_\phi B_\phi$  and (b)  $V_\phi$  fields of the first (solid line), second (dashed line), and third (dotted line) SAW modes along the  $L = 10$  magnetic field line.  $h_\phi B_\phi$  is normalized by the boundary value and  $V_\phi$  is normalized by the  $V_\phi$  in the equatorial point.

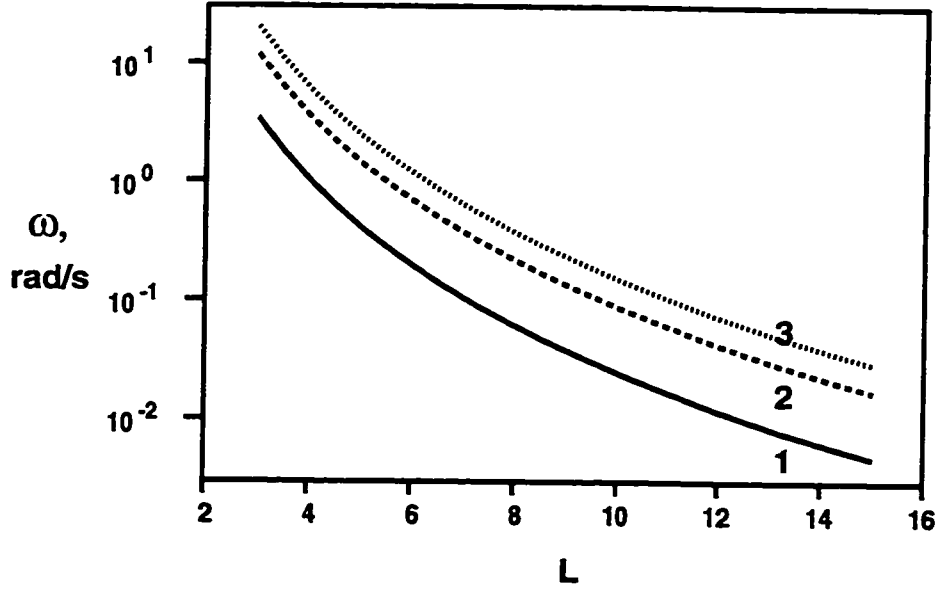


Figure 3.7:  $L$ -shell dependance of  $\omega$  for the first (solid line), second (dashed line), and third (dotted line) SAW modes.

The set of eigenfunctions and eigenfrequencies is a convenient tool to initialize numerous problems using the ADI code as well as to test the code. For example, if a SAW is excited by an initial perturbation of velocity which has a field aligned distribution prescribed by an eigenfunction, the code should reproduce the magnetic perturbation and SAW frequency predicted by the linear problem. On the other hand, if a SAW is excited by an arbitrary perturbation, it should generate a multi-harmonic SAW which can be compared with the linear spectrum. In order to test the nonlinear part of the ADI code and to describe the nonlinear evolution of SAWs in FLRs, we have developed a nonlinear analytical model which includes the linear growth of the SAW, the generation of acoustic modes due to the nonlinear ponderomotive force within a SAW, and the nonlinear saturation of the FLR amplitudes as a result of a nonlinear frequency detuning between the driver and the SAW. The next section is devoted to this problem.

## 3.4 Nonlinear Model of Field Line Resonances in a Dipolar Field

(A version of this section has been published: [Voronkov *et al.*, 1997b]).

### 3.4.1 Nonlinear Model of FLRs

The equation for driven toroidal SAWs follows from (2.1)-(2.4):

$$\frac{\partial h_\phi B_\phi}{\partial t} - \frac{1}{h_\nu^2} \frac{\partial}{\partial \mu} (h_\nu V_\phi B_0) = 0, \quad (3.18)$$

$$\frac{\partial V_\phi}{\partial t} = \frac{B_0}{4\pi\rho h_\mu h_\phi} \frac{\partial h_\phi B_\phi}{\partial \mu} + D, \quad (3.19)$$

where the term  $D = \omega V_D \sin(\omega t)$  models the effect of a CAW driver with frequency  $\omega$  and velocity amplitude  $V_D$  which can be taken as having an arbitrary dependence on  $\mu$ . We assume that  $V_D$  is independent of  $\nu$ . These equations also involve the dipolar magnetic field  $B_0(\mu, \nu)$  and the plasma density,  $\rho = \rho_0 + \delta\rho$ , where  $\delta\rho$  is the density perturbation due to the ponderomotive force.

It has been shown by Rankin *et al.* [1994; 1995] that the density perturbation  $\delta\rho$  is the main nonlinearity in the SAW equation (3.19). According to the continuity equation (2.3), this density perturbation couples to the parallel plasma velocity perturbation  $V_\mu$  and hence to the plasma pressure perturbation:

$$\frac{\partial \rho}{\partial t} + \frac{1}{h_\mu h_\nu h_\phi} \frac{\partial}{\partial \mu} (h_\nu h_\phi \rho V_\mu) = 0, \quad (3.20)$$

$$\left( \frac{\partial}{\partial t} + \frac{V_\mu}{h_\mu} \frac{\partial}{\partial \mu} \right) \frac{P}{\rho^\gamma} = 0, \quad (3.21)$$

$$\rho \frac{\partial V_\mu}{\partial t} + \frac{1}{h_\mu} \frac{\partial P}{\partial \mu} = \rho \frac{V_\phi^2}{h_\mu h_\phi} \frac{\partial h_\phi}{\partial \mu} - \frac{B_\phi}{4\pi h_\mu h_\phi} \frac{\partial h_\phi B_\phi}{\partial \mu} \equiv F_{pm}. \quad (3.22)$$

The set (3.20)-(3.22) describes the coupling between the excited SAW and SMW modes as a result of the ponderomotive force  $F_{pm}$ . As compared to the box model, the ponderomotive force in the dipolar geometry has an additional term which is dependant on the magnetic field line curvature.

### 3.4.2 Linear Growth of SAWs

Assuming that the driver amplitude is small and that its frequency is close to the SAW eigenmode,  $\Delta\omega = \omega_N - \omega \ll \omega$ , we can introduce the envelope approximation for the SAW:  $h_\phi B_\phi = \text{Re}[b_N e^{-i\omega t} S_N(\mu)]$ . The equation for  $B_\phi$  follows from (3.18) and (3.19) in the linear approximation ( $\rho = \rho_0$ ):

$$\frac{\partial^2}{\partial t^2} h_\phi B_\phi - \frac{1}{h_\nu^2} \frac{\partial}{\partial \mu} \left( \frac{V_{A0}^2}{h_\phi^2} \frac{\partial}{\partial \mu} h_\phi B_\phi + h_\nu B_\mu \omega V_D \text{Re}[ie^{-i\omega t}] \right) = 0. \quad (3.23)$$

Multiplying this equation by  $h_\nu^2 S_M$  and integrating it along the field line one finds a linear envelope equation for the SAW mode amplitude:

$$\frac{\partial b_N}{\partial t} = -i\Delta\omega b_N + \frac{\omega}{2} R, \quad (3.24)$$

where



$$R = \frac{1}{\omega} \int_{\mu_-}^{\mu_+} d\mu h_\nu B_\mu V_D \frac{dS_N}{d\mu} \quad (3.25)$$

is an effective driver amplitude. The solution to (3.23) is

$$h_\phi B_\phi = \frac{\omega R S_N}{\Delta\omega} \cos(\omega t) \sin\left(\frac{\Delta\omega}{2} t\right). \quad (3.26)$$

Equation (3.26) describes the linear evolution of the driven SAW and predicts that the central resonant peak of the FLR grows linearly with time and that the width of the resonance narrows with time.

### 3.4.3 Slow Magnetosonic Wave Response

From (3.22), the growth of the amplitude of the SAW results in a corresponding increase in the magnitude of the ponderomotive force  $F_{pm}$ . This causes motion of plasma toward the equatorial plane along geomagnetic field lines which results in a redistribution of the plasma density and pressure. In magnetospheric plasmas, the SMW frequency is much smaller than CAW and SAW frequencies. Therefore we can neglect variations of  $F_{pm}$  within the period of the SAW and consider only the time-averaged (over a SAW period) part of  $F_{pm}$  in the equations for parallel plasma motion, (3.20)-(3.22):

$$\langle F_{pm} \rangle = \frac{|b_N|^2}{8\pi h_\mu h_\phi^2} \left[ \frac{V_{A0}^2}{\omega_N^2 h_\mu^2 h_\phi} \frac{\partial h_\phi}{\partial \mu} \left( \frac{\partial S_N}{\partial \mu} \right)^2 - \frac{1}{2} \frac{\partial S_N^2}{\partial \mu} \right]. \quad (3.27)$$

Then, (3.20)-(3.22) may be reduced to an equation for the pressure variation  $\delta P = P - P_0$ :

$$\frac{\partial^2}{\partial t^2} \delta P - \frac{C_{S0}^2}{h_\mu^2} \frac{\partial}{\partial \mu} \left( \frac{\partial}{\partial \mu} \delta P - h_\mu \langle F_{pm} \rangle \right) = 0, \quad (3.28)$$

where  $C_{S0}^2(\mu) = \gamma P_0 / \rho_0$  is the square of the acoustic wave velocity at the initial moment of time.

The case  $F_{pm} = 0$  provides an equation for free SMW eigenmodes with eigenfrequencies  $\Omega_m$  and eigenfunctions  $U_m$  which are defined as  $C_{S0}^2 \delta \rho = \sum_m n_m U_m$ . It follows from (3.28) that SMW eigenfunctions satisfy the orthonormality condition

$$\int_{\mu_-}^{\mu_+} d\mu \frac{h_\mu^2}{C_{S0}^2} U_{m_1} U_{m_2} = \delta_{m_1 m_2}. \quad (3.29)$$

Integrating (3.28) over  $\mu$  with the weight  $U_m h_\mu^2 / C_{S0}^2$  one can then find an equation for the amplitude of the SMW:

$$\frac{\partial^2 n_m}{\partial t^2} + \Omega_m^2 n_m = - \int_{\mu_-}^{\mu_+} d\mu U_m \frac{\partial}{\partial \mu} h_\mu \langle F_{pm} \rangle = \frac{f_m}{2} |b_N|^2, \quad (3.30)$$

where  $n_m = \text{Re} [n_{0m} e^{-i\Omega_m t}]$ . The driving force in (3.30) is proportional to the local SAW intensity, and the projection  $f_m$  of the ponderomotive force on the  $m$ th SMW is

$$f_m = \int_{\mu_-}^{\mu_+} d\mu \frac{1}{4\pi h_\phi^2} \frac{\partial U_m}{\partial \mu} \frac{\partial S_N}{\partial \mu} \left[ \frac{V_{A0}^2}{\omega_N^2 h_\mu^2 h_\phi} \frac{\partial h_\phi}{\partial \mu} \frac{\partial S_N}{\partial \mu} - S_N \right]. \quad (3.31)$$

In the case of linearly driven SAWs, the solution to (3.30) provides the following prescription for the amplitude of the driven SMW density perturbations:

$$n_m = \frac{f_m \omega^2 R^2}{4\Omega_m^2 \Delta \omega^2} \left[ \frac{1}{\Omega_m^2 - \Delta \omega^2} (\Delta \omega^2 \cos \Omega_m t - \Omega_m^2 \cos \Delta \omega t) + 1 \right]. \quad (3.32)$$

The fact that the SAW can excite many SMW harmonics is the result of differences between the mode structure of SAW and SMW eigenfunctions due to the field aligned spatial inhomogeneity of the system. In the model of homogeneous plasma [Rankin *et al.*, 1994, 1995], the ponderomotive force can only couple directly to the fundamental mode SMW harmonic, and this coupling ultimately defines the nonlinear dynamics of the FLR.

In order to make the interaction between SAWs and SMWs self-consistent, it is necessary to account for the effect of the SMW density perturbations on the evolution of the driven SAW. It was mentioned above that according to Rankin *et al.* [1994; 1995], the most important nonlinear process affecting the SAW arises from the density perturbations in (3.19), which can be written as

$$\frac{\partial V_\phi}{\partial t} = \frac{B_0}{4\pi\rho_0 h_\mu h_\phi} \left(1 - \frac{\delta\rho}{\rho_0}\right) \frac{\partial h_\phi B_\phi}{\partial \mu} + D. \quad (3.33)$$

Here, we have assumed that the density perturbation is small:  $\delta\rho \ll \rho$ .

Substituting into (3.33) the eigenmode expansion of the density perturbations  $C_{S0}^2 \delta\rho = \sum_m n_m U_m$ , where  $n_m$  can be found from (3.30), and repeating the derivation of the envelope equation for the SAW amplitude, one finds that the density perturbation contributes an additional term to (3.24):

$$\frac{\partial b_N}{\partial t} = i(\Delta\omega_{nl} - \Delta\omega)b_N + \frac{\omega}{2}R, \quad (3.34)$$

where the nonlinear shift of the frequency of the SAW is defined by

$$\Delta\omega_{nl} = \sum_m n_m \int_{\mu_-}^{\mu_+} d\mu \frac{V_{A0}^2 U_m}{2\omega h_\phi^2 \rho_0 C_{S0}^2} \left(\frac{\partial S_N}{\partial \mu}\right)^2. \quad (3.35)$$

Equations (3.30) and (3.34) describe the nonlinear evolution of externally driven and coupled SAW and SMW modes. In the particular case where only one SMW mode is excited, equations (3.30) and (3.34) coincide exactly with the rectangular box model derived by *Rankin et al.* [1994; 1995]. The difference here is that field-aligned plasma inhomogeneity and magnetic field curvature result in multimode SMW excitation and a more complicated dynamics for the nonlinear evolution of the FLR. However, the general analysis of equations developed by *Rankin et al.* [1994] also holds for the dipolar model.

### 3.4.4 Numerical Solution and Analysis

In this part, we consider the nonlinear evolution of SAWs initiated by an external driver using one-dimensional full MHD simulations and the analytical model described above. We consider an example where the driver frequency resonates with the local SAW at  $L$  shell 10. The background density distribution is chosen in the form  $\rho_0 = \rho_{eq}(1 - \cos \theta^2)^{-q}$ , with  $\rho_{eq} = 1.044 \cdot 10^{-24} \text{ g/cm}^3$  and  $q = 4$ . For these parameters, the period  $T$  of the first fundamental SAW mode equals 254 s. The background plasma pressure is uniform along the field lines in equilibrium. We consider cases corresponding to different plasma temperatures in the equatorial region of the magnetosphere. The CAW driver is modeled by a Gaussian distribution of the velocity along the geomagnetic field line:  $V_D(\mu) = V_0 \exp(-Z^2/\delta^2)$  with  $V_0 = 1.6 \text{ km/s}$  and  $\delta = 2R_E$ . Here  $Z$  is the distance along the magnetic field line from the equatorial plane.

The temporal evolution of the SAW amplitude  $b_1$ , as predicted by (3.34) and obtained numerically using the complete set of MHD equations, is shown in Figure 3.8. In this figure and later in this section, all values of the magnetic field are given

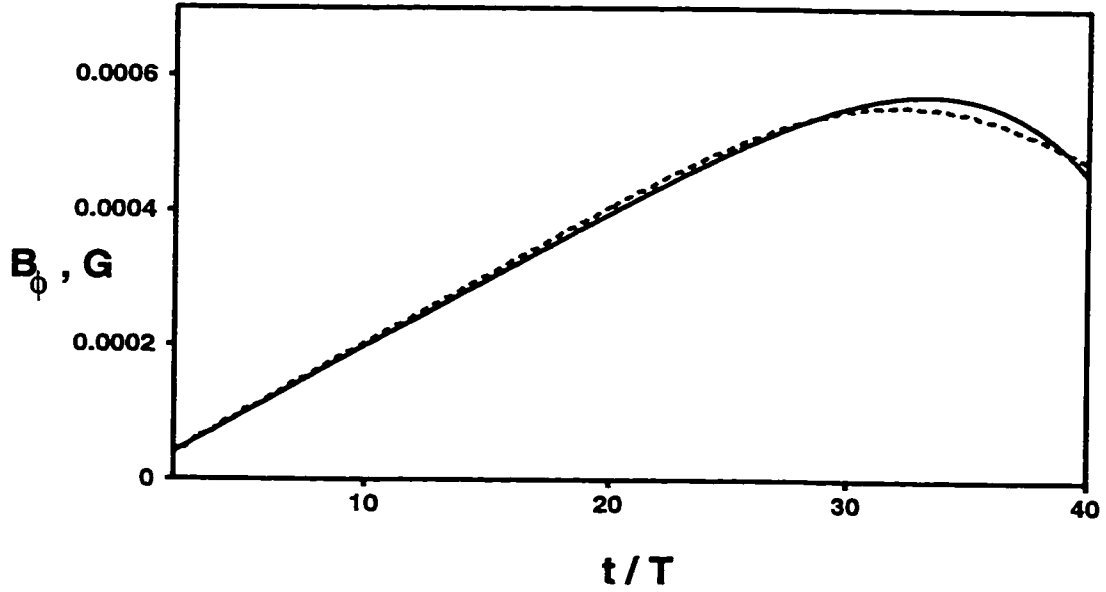


Figure 3.8: The growth of the amplitude of the SAW as predicted by the analytical model (solid line) and obtained numerically from the full set of MHD equations using the ADI code (dashed line).  $\beta$  is  $2.65 \cdot 10^{-2}$  in the equatorial plane.

in G. Time is normalized by the driver period  $T = 2\pi/\omega$ . In this example, the driver frequency  $\omega$  is set equal to the eigenfrequency of the SAW fundamental mode. The ambient plasma pressure  $P_0$  is  $10^{-10}$  dyn/cm<sup>2</sup> which corresponds to  $\beta = 8\pi P_0/B_\mu^2 = 2.65 \cdot 10^{-2}$  in the equatorial plane and  $\beta = 7.2 \cdot 10^{-9}$  near to the ionosphere. From Figure 3.8, it can be seen that the analytical model gives a good prediction of the SAW amplitude evolution during both the linear and nonlinear stages. Similar tests were done for different values of  $\beta$ . The analytical and numerical results were in close agreement.

Now let us consider the influence of the temperature of the plasma in the equatorial plane on the growth and nonlinear saturation of the SAW. Figure 3.9 shows the time evolution of the SAW amplitude and phase for different equatorial values of  $\beta$ :  $2.65 \cdot 10^{-4}$ ,  $2.65 \cdot 10^{-3}$ ,  $2.65 \cdot 10^{-2}$ , and 0.88, respectively. It can be seen

that nonlinear saturation due to the ponderomotive phase shift of the SAW occurs in all cases, but as expected, lower plasma temperatures lead to faster saturation, so that one could expect to observe higher amplitude SAWs on field lines which project into hot plasma regions of the equatorial magnetosphere. In fact, very large amplitude FLRs which may produce active auroral arcs are seen in the evening sector on field lines threading the high  $\beta$  region of the plasma sheet [Samson *et al.*, 1996a]. In our simulations for the hot plasma case with the driver defined above, the amplitude of the SAW velocity reaches a value of 80 km/s in the equatorial plane. Comparing Figure 3.9a with Figure 3.9b, we see that in all cases, the amplitude saturation coincides with a nonlinear temporal phase shift of  $\pi/2$ . This is consistent with the results of Rankin *et al.* [1995].

An important feature in the theory of nonlinear dipole FLRs is the coupling of the excited SAW with a spectrum of SMW modes. The temporal evolution of the amplitudes in the SMW spectrum are shown in Figure 3.10 for the case  $\beta = 2.65 \cdot 10^{-2}$ . Amplitudes have been normalized by the maximum amplitude in the SMW spectrum at the moment of time for which each spectrum is computed. One can see that during the initial stage, a wide spectrum of SMW modes is excited. Later, the spectrum becomes sharply peaked at the second spatial harmonic, which is eventually responsible for the nonlinear SAW saturation. Note that it is the second harmonic SMW that has been accounted for in the box model of Rankin *et al.* [1994] which implies that the box model also reasonably predicts the FLR saturation although it falls short in describing the FLR dynamics.

Figure 3.11 shows the field-aligned distribution of the pressure perturbation at the moment of FLR saturation ( $t = 30T$ ). At this time, the SMW perturbation mainly corresponds to the second harmonic with an amplitude  $\delta P/P_0 \sim 0.4$  in the equatorial plane. Higher SMW harmonics have smaller amplitudes of the order

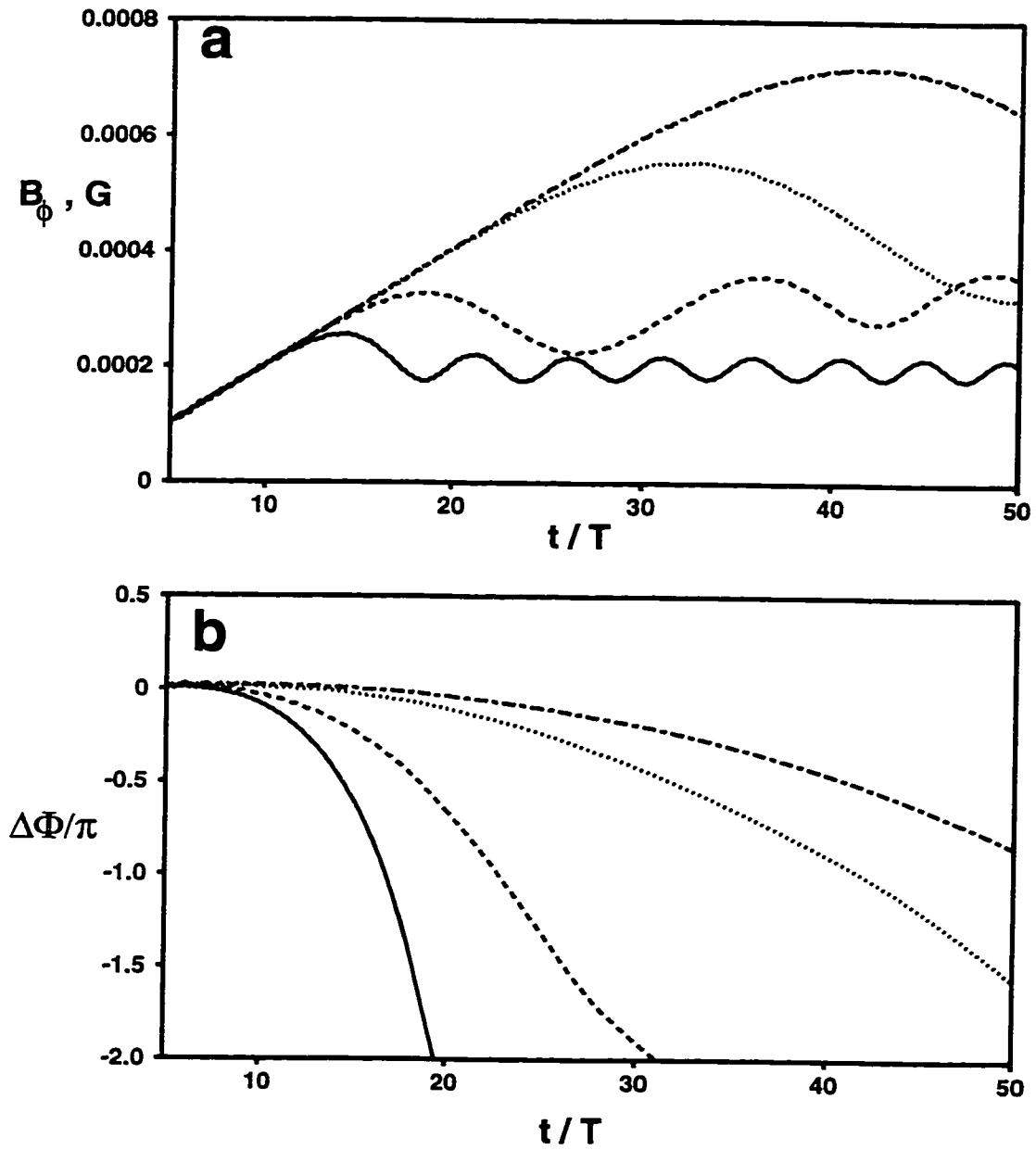


Figure 3.9: The evolution of the SAW amplitude (a) and phase (b) for  $\beta = 2.65 \cdot 10^{-4}$  (solid line);  $2.65 \cdot 10^{-3}$  (dashed line);  $2.65 \cdot 10^{-2}$  (dotted line) and 0.88 (dash-dotted line).

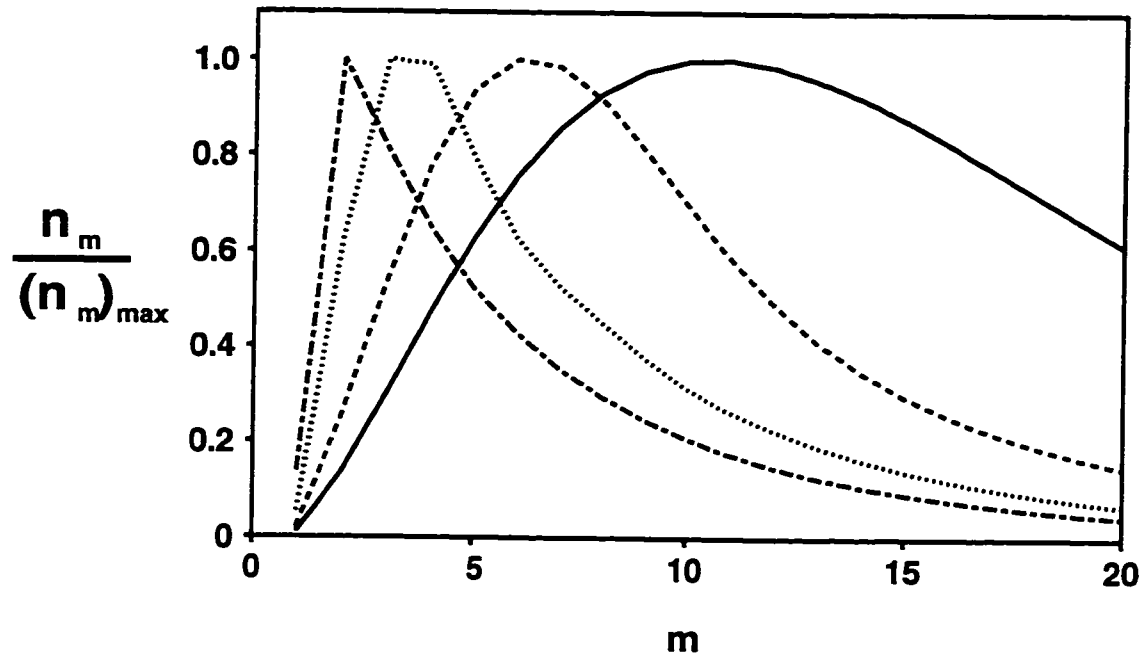


Figure 3.10: Normalized spectra of acoustic waves, generated by the FLR at time  $T$  (solid line),  $4T$  (dashed line),  $10T$  (dotted line), and  $20T$  (dash-dotted line);  $\beta = 2.65 \cdot 10^{-2}$  in the equatorial plane.



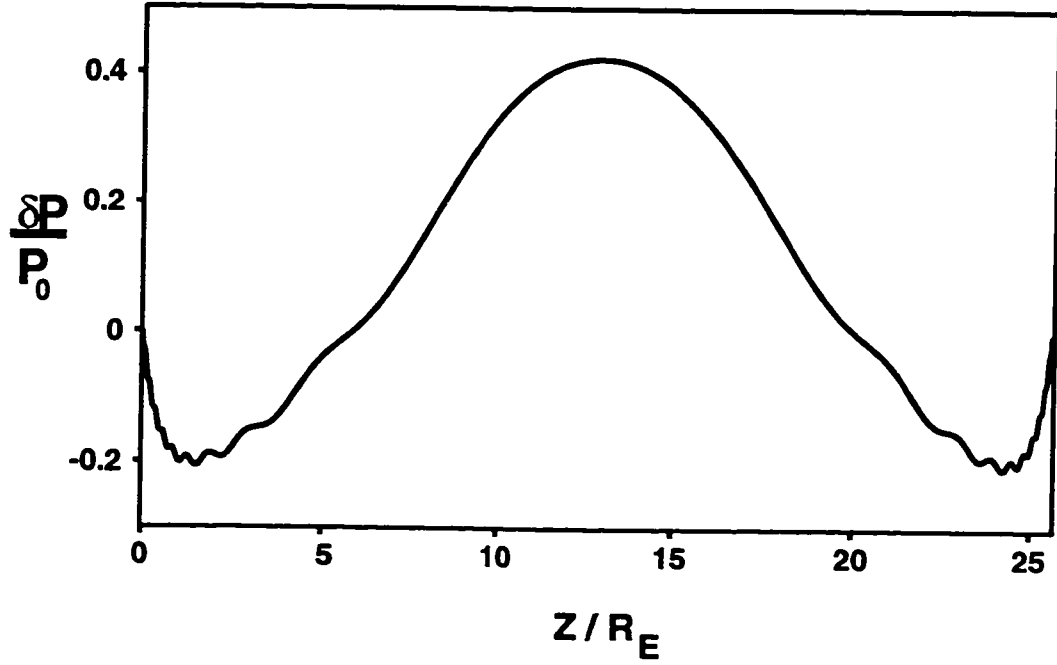


Figure 3.11: Pressure perturbation distribution along the field line at  $t = 30T$ .  $\beta = 2.65 \cdot 10^{-2}$  in the equatorial plane. The distance  $Z$  along the field line is normalized by the Earth's radius  $R_E$ .

of a few percent of the ambient pressure. However, it is interesting to note that because of the field aligned dispersion, these waves are concentrated at distances of  $\sim 1 - 2 R_E$  from the ionosphere and therefore they might have a significant impact on particle heating and acceleration. Higher-frequency SMW harmonics interact intensively with ions with the rate  $\text{Im}\Omega/\text{Re}\Omega \sim 1.1\xi^{7/4}\exp(-\xi^2)$ , where  $\xi = T_e/T_i$  is the ratio of electron and ion temperatures [Chen, 1984].

Another result that is of interest within this model is the growth and saturation of SAWs in the case when the driver frequency is detuned with respect to the SAW eigenfrequency. The amplitude of the SAW is presented in Figure 3.12 as a function of the frequency shift between the SAW and driver for the case  $\beta = 2.65 \cdot 10^{-2}$  and for different moments of time. Since the SAW frequency depends

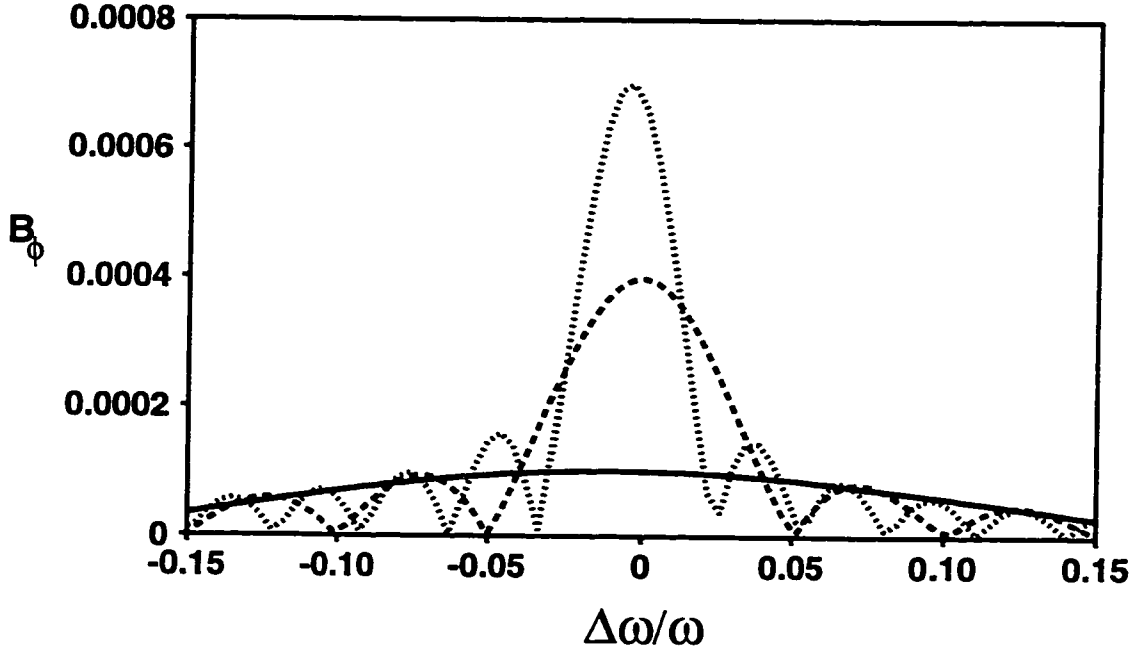


Figure 3.12: SAW amplitudes as a function of the frequency shift between the driver and SAW at time  $5T$  (solid line),  $20T$  (dashed line),  $35T$  (dotted line).  $\beta = 2.65 \cdot 10^{-2}$  in the equatorial plane.

on latitude, Figure 3.12 can be considered as the latitude dependance of the FLR amplitude. Initially, the FLR spreads over a wide range of latitudes. Later, the amplitude is peaked around the eigenfrequency of the resonant magnetic shell, and its maximum shifts toward lower frequency shells.

### 3.5 Three Dimensional Evolution of SAWs

An important feature of the FLR predicted by the theory above is the fact that SAWs evolve into a narrow channel around the resonant  $L$ -shell. In order to estimate the thickness of the FLR region, let us consider the three-dimensional evolution of FLRs obtained using the ADI code.

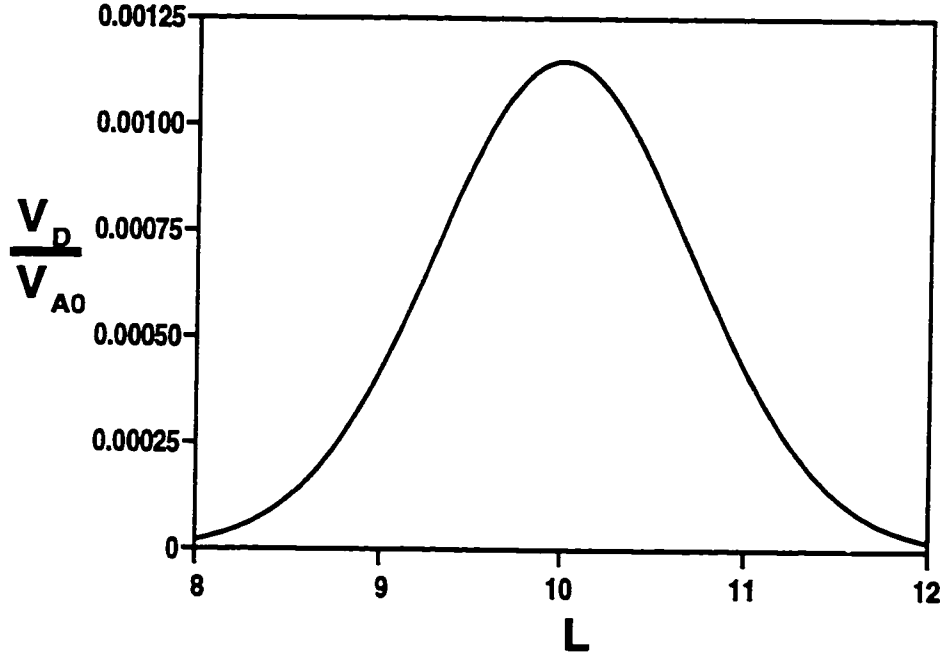


Figure 3.13: Radial distribution of the driver velocity in the equatorial plane.

Here we still neglect azimuthal dispersion effects assuming large wavelengths in the  $\phi$ -direction. A FLR was simulated within  $L$ -shells 8-12. The driver frequency corresponds to the SAW eigenfrequency at  $L=10$  shell as in the previous section. The spatial distribution of the driver amplitude as a function of radial distances in the equatorial plane is shown in Figure 3.13. In this figure, velocities are normalized by the initial Alfvén velocity  $V_{A0}$  in the equatorial plane at  $L=10$ , which is 1384 km/s in this model.

The radial distribution of the SAW velocity at the equatorial plane is presented in Figure 3.14 for  $t = 10T$ . The velocity profiles are plotted for two different phases during one period: when the SAW is seen as a unidirectional plasma flow and when it produces an antisymmetric azimuthal flow. As seen from this figure, the resulting FLR flow channel has the thickness of the order of  $0.5R_E$  with a shear

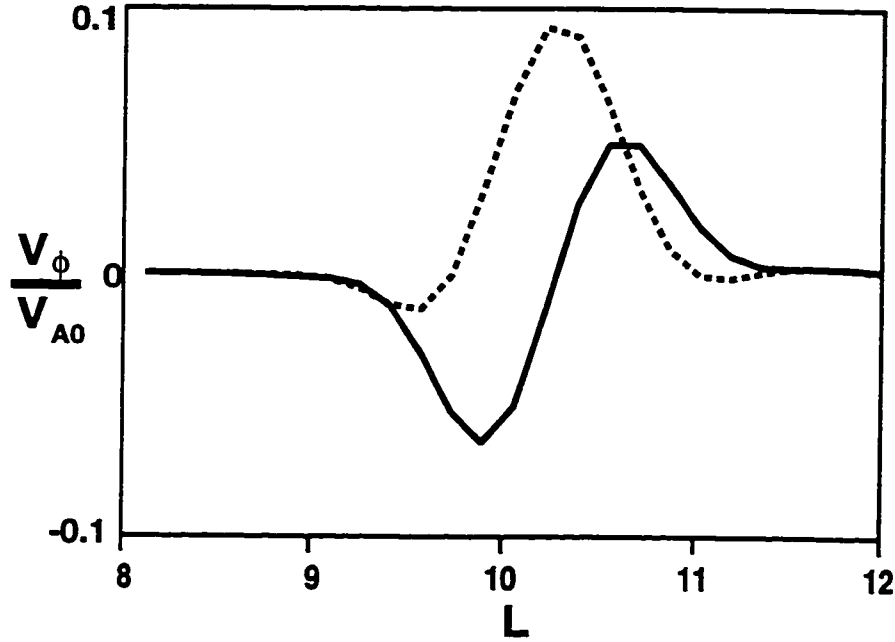


Figure 3.14: Radial distribution of the SAW velocity in the equatorial plane for different phases of the SAW.

$\sim 0.2R_E$  in the equatorial plane. For the shear flow amplitude of the order of  $\sim 100$  km/s which is in agreement with observations of FLRs in the Earth's magnetosphere, this shear flow channel may become unstable with respect to the shear flow (KH) instability.

The results of these simulations allow us to estimate the growth rate of the KH instability due to radial FLR structuring in the equatorial plane. Assuming Gaussian distribution of velocity in the SAW channel, the growth rate can be found from (1.23) as a function of time. The amplitude and thickness of the flow was evaluated using simulations described in this section. Dependence of the KH instability  $e$ -folding time ( $\gamma^{-1}$ ) on the FLR evolution time is presented in Figure 3.15. As seen from this figure,  $e$ -folding time eventually becomes smaller than the SAW

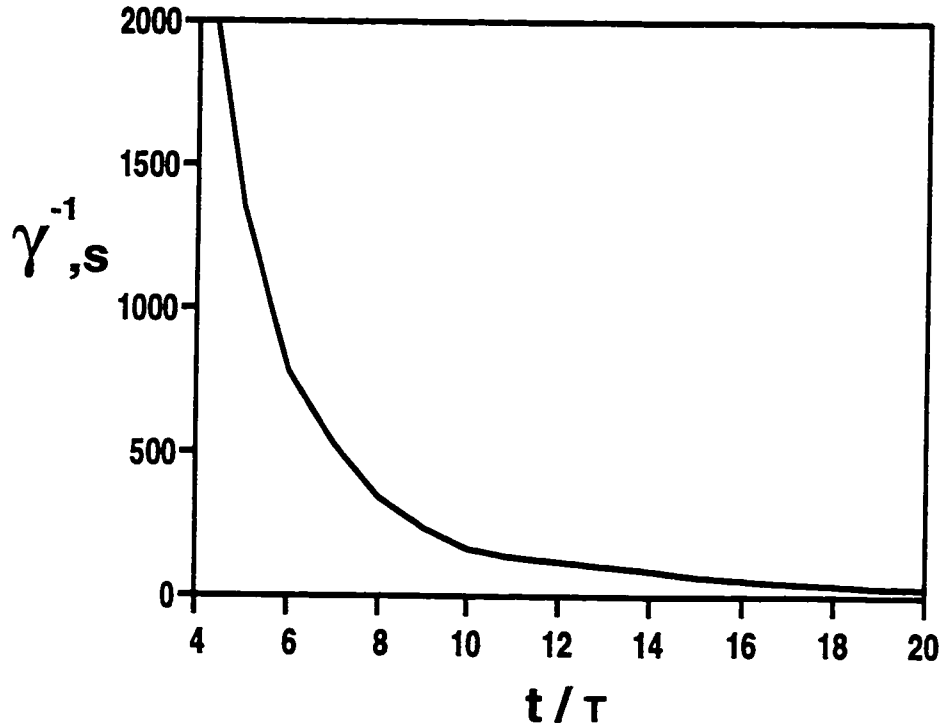


Figure 3.15: Dependence of the KH instability e-folding time on the time of FLR evolution.

half-period. This suggests that the KH-instability may develop in the FLR region forming vortical structures. Such vortices have been observed in association with large amplitude SAWs [*Rankin et al.*, 1993a; *Fenrich*, 1997].

At the ionospheric level, SAWs initiate field-aligned currents (FACs) which provide a magnetosphere-ionosphere interaction within a FLR. The profile of the FACs is presented in Figure 3.16. This figure shows that the FLR produces a pair of FACs (downward and upward) with the longitudinal thickness of the order of tens of kilometers. This appears to be in agreement with the estimated observational thickness of FLRs [*Fenrich et al.*, 1995] and FLR modulated auroras [*Xu et al.*, 1993; *Samson et al.*, 1998] in the ionosphere.

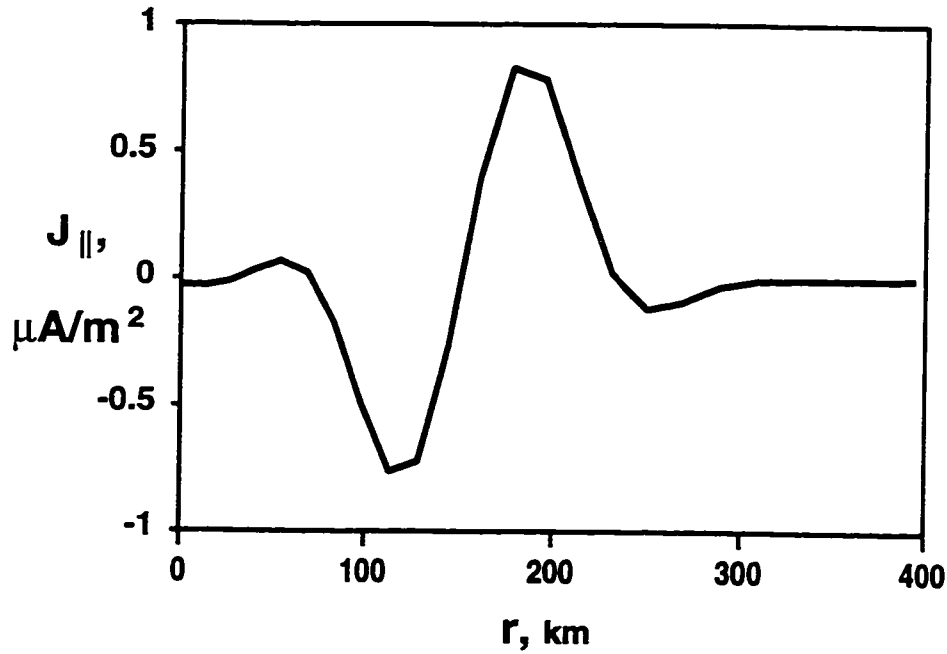


Figure 3.16: Meridional profile of FACs at the ionospheric level.

Because of the earthward gradient of the Alfvén velocity in the equatorial plane, the maximum of the SAW moves anti-earthward during one period. This results in the poleward motion of the FAC sheets. This motion is illustrated by Figure 3.17 where the FAC intensity is shown as a function of latitude and time. If regions of upward FACs correspond to the electron precipitation area, this motion is expected to be observed in the auroral luminosity motion. An example of such a motion is presented in Figure 3.18 [Samson et al., 1998], where the intensity of the 6300 Å luminosity band observed by Gillam and Rankin photometers during the FLR event on January 20, 1996 is plotted in similar coordinates (latitude versus time) as in Figure 3.17 (one degree of latitude corresponds to  $\sim 113$  km at the ionospheric level).

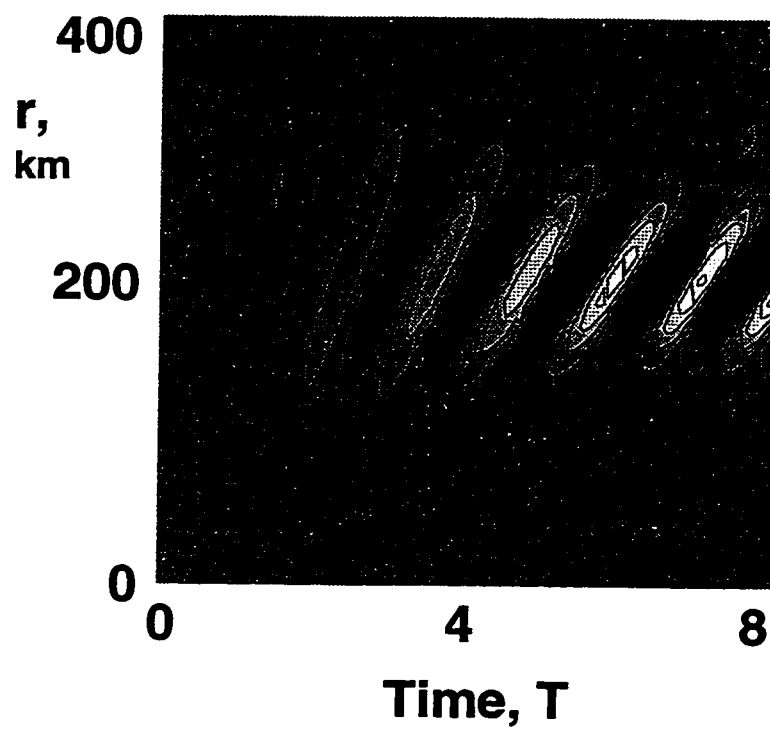


Figure 3.17: Poleward motion of FACs in the FLR region at the ionosphere level. Here,  $r$  is the distance in the meridional direction at the ionospheric level.

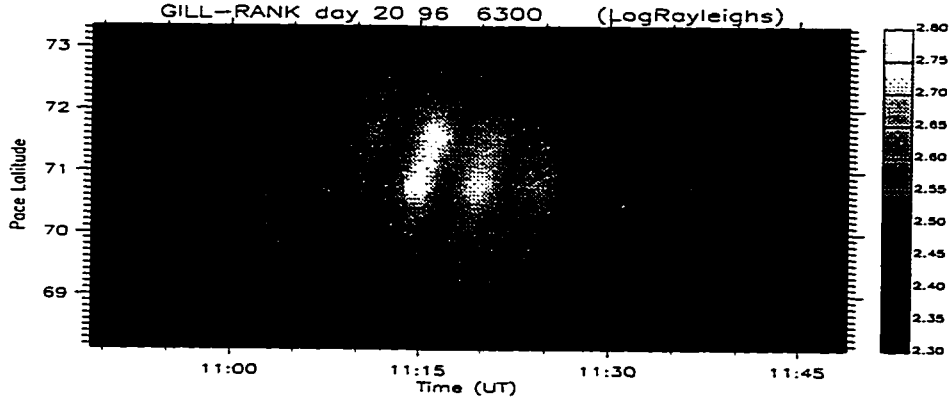


Figure 3.18: Photometer data for the 6300 Å emission associated with a FLR.

### 3.6 Discussion

In this chapter, we described the SAW structure and evolution in FLR regions. We have developed a numerical routine which allowed us to compute SAW eigenmodes and eigenvectors in nonuniform plasmas on curvilinear magnetic field lines. Therefore, SAW fields were found independently of the ADI code and were used to test the ADI code.

SAW evolution in FLR regions was studied using the analytical theory and computer simulations. The theory of FLRs presented above is an advance from the previous box model [Rankin *et al.*, 1994, 1995] toward a more realistic description of nonlinear FLRs. We have taken into account the dipolar geometry of resonant



magnetic shells and the nonuniform distribution of plasma density along geomagnetic field lines. The analytical theory and numerical simulations confirm the main results obtained using the box model. It is shown that the SAW grows because of a resonant coupling with a CAW. In turn, the SAW initiates a ponderomotive force which leads to plasma density redistribution and nonlinear saturation of the FLR due to frequency detuning of the resonant magnetic shell. Compared to the box model, this ponderomotive force consists of three parts: magnetic pressure, magnetic curvature, and particle inertia. We have shown that the density redistribution can be described using an equation for driven SMWs. Owing to the geometry and density inhomogeneity, the coupling between a SAW and nonlinear density perturbations results in the excitation of a wide spectrum of SMWs which gradually form a narrow peak in the vicinity of the second harmonic SMW. The second harmonic SMW is responsible for SAW detuning and FLR saturation. However, the smaller SMW modes may still reach significant amplitudes and might play an important role in particle heating and acceleration at altitudes of 1-2  $R_E$  above the ionosphere. This heating, in conjunction with such mechanisms as two-fluid ponderomotive force acceleration [*Li and Temerin, 1993*], can play an important part in the auroral magnetosphere-ionosphere interaction.

Another result predicted by the dipolar FLR theory is that higher temperatures in the equatorial magnetosphere increase the timescale for ponderomotive FLR saturation, in which case the FLR SAW can grow to large amplitude. This result appears to be in agreement with an observed latitudinal distribution of Pc5 pulsations which have a maximum in the region corresponding to the hot plasmas of the ring current belts [*Walker and Greenwald, 1981; Tian et al., 1991; Potemra and Blomberg, 1996*] and of the evening sector of the inner plasma sheet [*Samson et al., 1996a*].

Using the theory and numerical simulations, we have found that the FLR should evolve into a narrow channel near a resonant shell which can eventually lead to Kelvin-Helmholtz shear flow instabilities [*Rankin et al.*, 1993a]. However in this model, we neglect dispersive effects due to the finite electron skin depth causing electron inertia effect [*Streltsov and Lotko* 1996; 1997]. Electron inertia results in the radial energy outflows from the resonance region which can lead to the FLR saturation. The quantitative comparison of nonlinear saturation due to the ponderomotive force and electron inertia effects can be suggested as a logical step for further study of FLR structure.

In this study, we assumed that ionospheric conductivity is infinitely high. Low conductivity may cause energy dissipation from the Pedersen currents and the interaction of the toroidal and poloidal modes because of the Hall current [*Allan and Knox*, 1979]. Another dispersive mechanism which can affect the nonlinear evolution of FLRs is azimuthal gradients of high-amplitude SAWs. This effect can be significant for large- $m$  (small azimuthal wavelength) SAWs [*Klimushkin et al.*, 1995]. These waves have been observed in the midnight sector of the magnetosphere, whereas small- $m$  FLRs appear in the dawn and dusk sectors [*Fenrich et al.*, 1995; *Fenrich*, 1997]. The detailed modeling of these effects can be addressed in future investigation.

## CHAPTER 4

# Shear Flow and Shear Flow Ballooning Instabilities in the Equatorial Plane of the Earth's Magnetosphere

(A version of this chapter has been published: [Voronkov *et al.*, 1997a])

### 4.1 Preliminary Remarks

In the previous chapter we showed that FLRs may evolve into narrow channels with high amplitude shear flows in the equatorial magnetosphere. These shear flows vary from uni-directional to bi-directional (cf. Figure 3.14). The three-dimensional distribution of the azimuthal velocity is presented in Figure 4.1. If an azimuthal wave length of a KH mode is smaller than an azimuthal wave length of a SAW, we can examine the evolution of the KH instability within FLR fields and consider two types of radial flow profiles.

As discussed in chapter 1, many observations of auroral arcs have shown that they are typically associated with shear flow and vortex structures [Steen and Collis, 1988; Elphinstone *et al.*, 1995; Samson *et al.*, 1996a]. The evening and premidnight sector seems to be the most active region [Kidd and Rostoker, 1991; Murphree and Johnson, 1996; Samson *et al.*, 1996a,b; 1998]. Some authors have suggested that vortex formation in auroral arcs might be caused by shear flows or Kelvin-Helmholtz

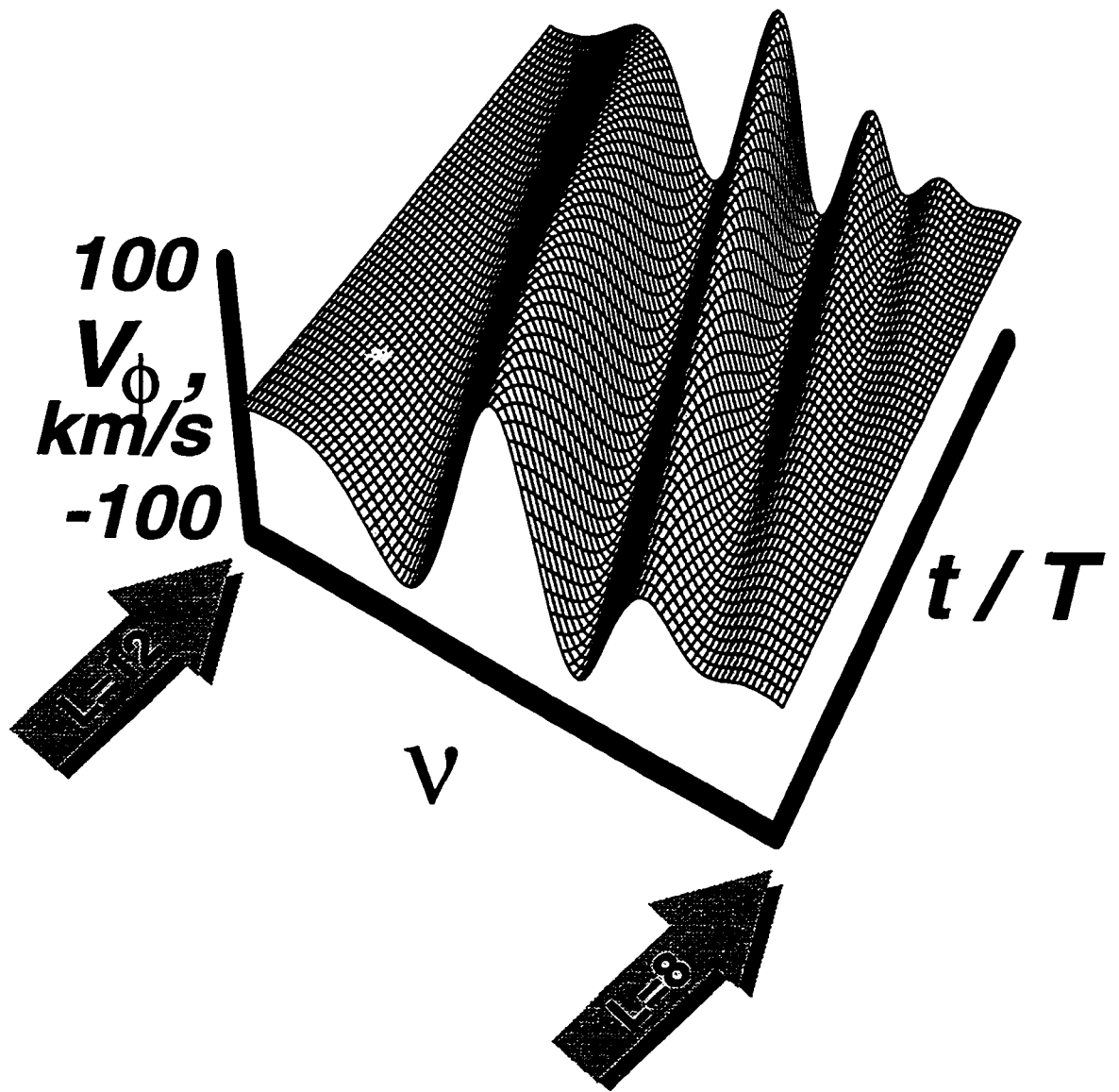


Figure 4.1: Variations of the azimuthal velocity of a SAW in the equatorial plane for one period.

(KH) instabilities in the auroral arc [*Steen and Collis*, 1988; *Kidd and Rostoker*, 1991; *Rankin et al.*, 1993a]. Nevertheless, we should note that KH instabilities alone do not lead to increased kinetic energy in the plasma flow and cannot explain the very large and active auroral vortices that are sometimes seen. A mechanism is needed which will allow extraction of the potential energy stored in regions of the magnetosphere, for example the growth phase magnetosphere, in order to allow the explosive (tens of seconds) growth of the kinetic energy associated with plasma flows. A clue to what this mechanism is might be found in the fact that these active electron arcs are often seen within regions of strong  $H\beta$  emissions and energetic proton (10s of keV) precipitation at the equatorward edge of the evening sector auroral region [*Samson et al.*, 1992b; *Samson et al.*, 1996a]. These  $H\beta$  emissions occur on field lines which thread the inner edge of the plasmashet in regions where there are strong Earthward pressure gradients [*Roux et al.*, 1991; *Kistler et al.*, 1992], particularly during substorm growth phases. Due to the energetic ion trajectories, the strongest pressure gradients are found in the evening sector and before local midnight [*Lyons and Samson*, 1992; *Lyons*, 1995].

Observations of strong Earthward pressure gradients suggest that ballooning or Rayleigh-Taylor modes might play a role in the extraction of the potential energy stored in the near Earth magnetotail. Nevertheless, most analyses have shown that this region is ballooning stable or only slightly unstable [*Lee and Wolf*, 1992; *Ohtani and Tamao*, 1993]. Furthermore, a simple ballooning instability can not be initiated by “white noise” because the ballooning modes of the scales of interest have virtually the same growth rate (cf. Figure 1.6). The presence of both shear flow in the auroral arc and strong pressure gradients in the equatorial magnetosphere suggests that a coupling of shear flow instabilities with a ballooning mode might be a possible mechanism for the formation of large scale vortices.

It is well known that shear flows can stabilize ballooning modes with large wave numbers [Viñas and Madden, 1986; Tajima *et al.*, 1991], in our case - large azimuthal wave numbers. Nevertheless, the evolution of lower wavenumber modes might allow substantial growth of vortex structures and a rapid enhancement of the plasma kinetic energy. While it is not obvious that KH modes have flows and structures which allow the driving of hybrid shear flow ballooning modes, we will show the results of linear analysis and nonlinear computer simulations which indicate that this coupling can occur. In the linear stage, the system develops a KH-like mode which generates a vortex. In the nonlinear stage, this vortex drives radial flows which disturb the initial equilibrium pressure. The pressure perturbations are unstable with respect to the ballooning instability and initiate cell-like flows which constructively add to the initial vortex. This nonlinear interaction results in the growth of a hybrid mode, which starts from large amplitude with a spatial scale that is defined by the nonlinear KH-like vortex. It will be shown that the hybrid instability can grow very rapidly in the equatorial magnetosphere, with e-folding times of the order of tens of seconds.

## 4.2 Theoretical Model

### 4.2.1 Basic Equations

We adopt a one fluid ideal magnetohydrodynamic (MHD) set (2.1)-(2.4) that will be used to model plasma in the equatorial region of the inner edge of the plasma sheet.

We neglect the effect of magnetic field line tying in the ionosphere, and concentrate on a local analysis of the instability in the equatorial region of the

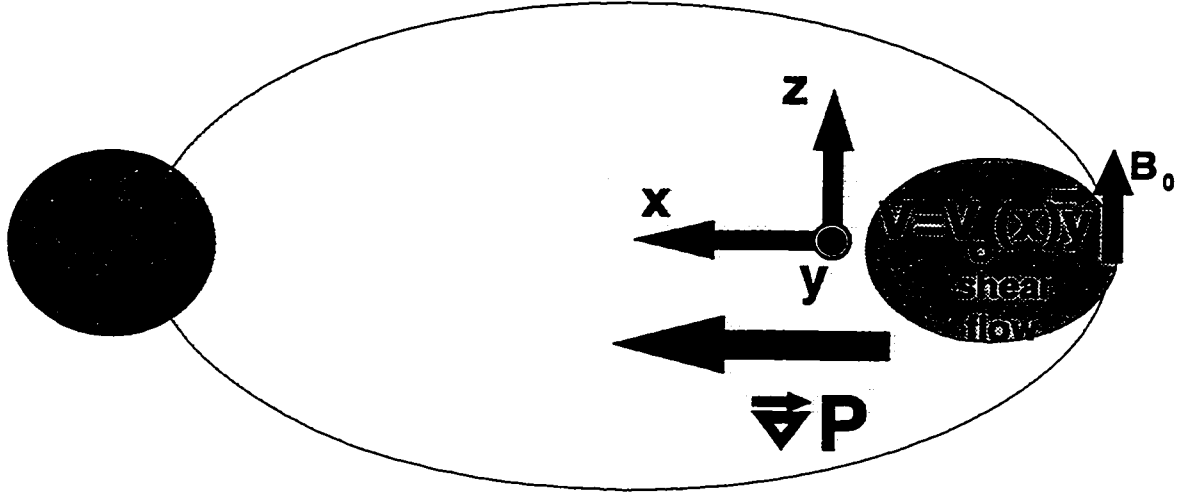


Figure 4.2: A schematic of the inner plasma sheet: a shear flow is embedded in a region of pressure gradient and stretched magnetic field lines.

plasma sheet. We shall develop a model which assumes that magnetic field lines are stretched slightly tailward, and consider the case where the radius of meridional magnetic field line curvature is much smaller than the radius of azimuthal curvature. In this study, we choose a fluid treatment of the problem, neglecting kinetic or finite Larmor radius effects and have assumed that resistivity is negligible.

In the equatorial plane there are two forces produced by magnetic field line curvature that act on plasma in the radial direction: the particle inertial force  $\rho V_z^2/R$  directed tailward and the magnetic curvature force  $-B_z^2/4\pi R$  acting Earthward, where  $z$  is the direction of the ambient magnetic field and  $R$  is the radius of the magnetic field line curvature in the meridional plane. For simplicity, in this study we assume that the difference between these two forces produces an effective centripetal acceleration (or “effective gravity”)  $g$  in the Earthward direction, which is considered to be constant in the interaction region. This assumption allows us to develop a simple analytical model using a Cartesian geometry, in which the  $x$ -axis is directed Earthward, the  $y$ -axis is in the dawn-dusk direction, and the  $z$ -axis is in the ambient

magnetic field direction. This geometry is illustrated in Figure 4.2. We suppose that the shear flow is directed in the azimuthal direction,  $V_y = V_0(x)$ . In equilibrium, the plasma density, pressure, magnetic field and shear flow velocity are considered to be functions of  $x$  only. These assumptions are similar to those made in other papers devoted to a local analysis of shear flow processes [ *Miura and Pritchett*, 1982; *Viñas and Madden*, 1986]. The dynamics of the shear flow in a plasma with a pressure gradient can then be described using the two-dimensional form of MHD equations (2.1)-(2.4) with (2.2) replaced by:

$$\rho \frac{\partial \mathbf{V}}{\partial t} + \rho (\mathbf{V} \cdot \nabla_{\perp}) \mathbf{V} + \nabla_{\perp} (P + \frac{B^2}{8\pi}) - \rho \mathbf{g} = 0, \quad (4.1)$$

where  $\nabla_{\perp}$  stands for the gradient in the equatorial plane.

Our equilibrium is defined as the balance between the effective acceleration and pressure force,

$$\rho_0 g = \frac{\partial}{\partial x} (P_0 + \frac{B_0^2}{8\pi}). \quad (4.2)$$

We consider the stability of this equilibrium with respect to a small perturbation  $e^{i(ky - \omega t)}$ . Assuming that the half width of the shear flow  $\delta$  is much smaller than the pressure gradient spatial scale  $L$ , one can reduce the system of MHD equations above to an equation for the radial component of the flow velocity  $V_x$ ,

$$V_x'' = k^2 V_x (1 - \frac{V_0''}{k(\omega - kV_0)} - \frac{W^2}{(\omega - kV_0)^2}) \quad (4.3)$$

where,



$$W^2 = -\frac{g\rho_0'}{\rho_0} - \frac{g^2}{V_f^2} \quad (4.4)$$

is the analog of the Brunt-Väisälä frequency [Pedlosky, 1987],  $\omega - kV_0(x)$  is the Doppler shifted wave frequency,  $V_f^2 = C_s^2 + V_A^2$  is the square of the fast mode velocity,  $V_0(x)$  is the shear flow velocity, and the dash symbol stands for the derivative with respect to  $x$ .

### 4.2.2 Qualitative Analysis of the Hybrid Mode Instability

Equation (4.3) describes velocity perturbations that arise due to a pressure gradient ( $W$ ) and a shear flow ( $V_0$ ). Depending on the sign of  $W^2$ , the system may be ballooning stable ( $W^2 > 0$ ) or unstable ( $W^2 < 0$ ). In the case where the thermal pressure is a function of the radial distance, whereas the density and magnetic field are uniform in the equilibrium state,  $W^2$  is always negative and therefore the ballooning growth rate  $\gamma_{bal}$  is positive:  $\gamma_{bal} \sim (-W) \sim V_f/L$  for  $k \geq 1/L$ , where  $L$  is the scale of the pressure gradient. The KH instability also has a positive growth rate,  $\gamma_{KH} \sim V_0/\delta$ , for wavenumbers  $k \sim 1/\delta$ . Now we demonstrate that these two processes interact in a constructive way, thereby increasing the growth rates of both instabilities and generating a new hybrid mode. This hybrid mode has both ballooning cell and vortical (KH) components and allows for energy exchange between them.

The physical processes responsible for the coupling can be described as follows (Figure 4.3). Let us assume that  $\rho_0(x)$  and  $g(x)$  are constant and that the gradient of plasma pressure is caused by a temperature gradient in the region where the shear flow exists. We also assume that  $V_0/\delta \gg V_f/L$ , so that the KH instability has the faster growth rate. This means that the instability is initiated as a pure KH

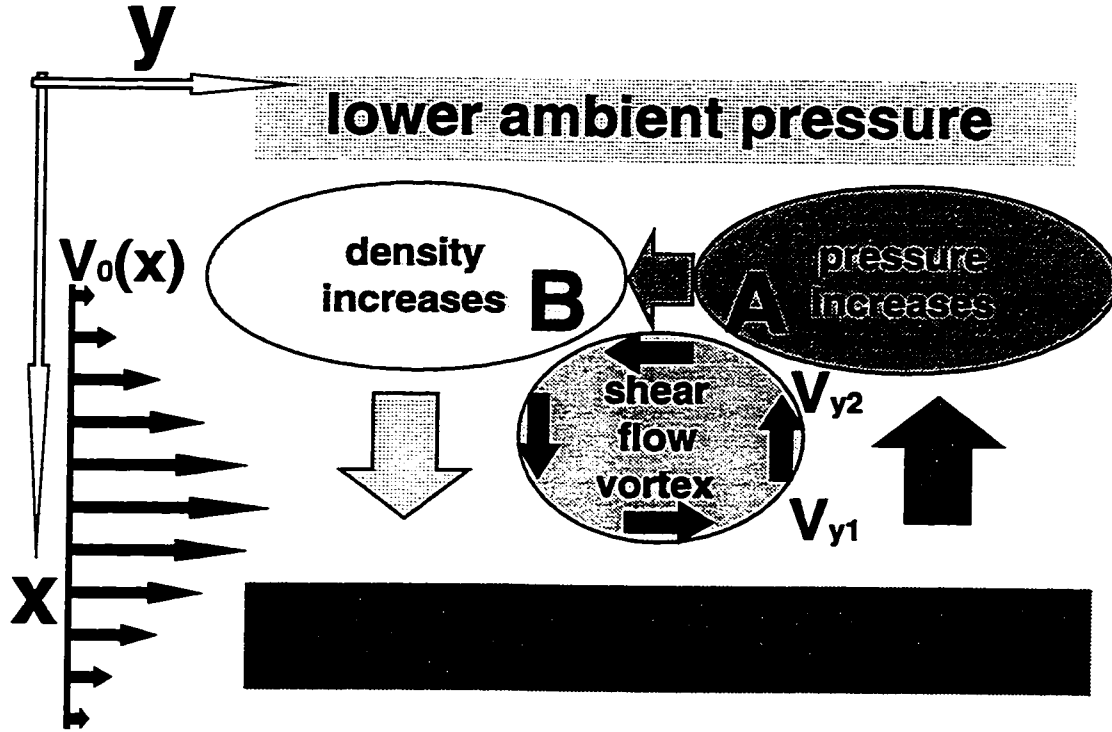


Figure 4.3: A schematic showing the interaction of a shear flow vortex with a pressure gradient cell. A Gaussian shaped shear flow is assumed.

instability which generates a vortex as follows. Suppose that a small perturbation of the radial component of the velocity appears in the shear flow. This involves motion of plasma which causes the flow to deviate from its initial direction and initiates a shear flow vortex shown in the centre of Figure 4.3.

Now let us assume that this KH vortex evolves in a plasma with a temperature gradient, and therefore involves a transfer of plasma energy along stream lines. Let us consider the evolution of the plasma pressure and effective gravity in association with plasma motion along flow streamlines. In Figure 4.3, the radial flux into cell A, initiated by the flow from region  $V_{y1}$  to region  $V_{y2}$ , is opposite the plasma pressure gradient and involves motion of plasma from a hotter region to a colder

region. The colder region allows the hotter region to expand, so that the plasma pressure grows in cell A. The increased pressure in cell A initiates a plasma flow in the  $y$ -direction which contributes to the vortex component and is associated with plasma motion into cell B, providing for a growth of the density in the cell B. As a result, the radial component of the effective force  $\rho g - \nabla P$  deviates from its equilibrium value and is directed out of cell B along the KH vortex streamlines. The resulting acceleration provides additional growth of the KH vortex. Therefore, the ballooning mode accelerates the shear flow vortex and provides a constructive interaction between these two modes.

### 4.2.3 Linear Theory of the Hybrid Instability

The solution to (4.3) was found numerically using a spectral method which can be described as follows. Let us expand the solution of (4.3) into a series of orthogonal functions

$$\Psi = \sum_{n=-N}^N C_n S_n, \quad (4.5)$$

where  $S_n = e^{(in\pi x/L)}$  and  $C_n$  are coefficients. Multiplying (4.5) by a complex conjugate value  $S_m^*$  and integrating over the region  $[-L, L]$ , we end up with a set of linear algebraic equations for  $C_n$  in the form of an eigenvalue problem:

$$\sum_{n=-N}^N \left( -\frac{n^2 \pi^2}{L^2} \delta_{n-m} + \frac{1}{2L} \langle S_m^*, \alpha^2 S_n \rangle \right) C_n = k^2 \sum_{n=-N}^N C_n \delta_{n-m}, \quad (4.6)$$

where

$$\langle S_m^*, \alpha^2 S_n \rangle = \int_{-L}^L \left( \frac{V_0'' k}{\omega - k V_0} + \frac{W^2 k^2}{(\omega - k V_0)^2} \right) \exp\left(\frac{i\pi x(n-m)}{L}\right) dx \quad (4.7)$$

is an operator defined by the physical parameters of the problem.

Equation (4.6) is homogeneous and has a nontrivial solution if the determinant of its coefficients equals zero. This equation is solved for the eigenvalues  $\omega$ , and then the eigenfunctions can be computed for every given eigenvalue  $\omega$ .

The growth rate for pure Kelvin-Helmholtz, hybrid (KH+ballooning) and noninteractive ballooning modes is shown in Figure 4.4. A Gaussian profile for the shear flow in the radial  $x$ -direction was chosen in the form:  $V_y(x)/V_0 = \exp(-(x - x_0)^2/\delta^2)$ . The Brunt-Väisälä frequency for this case corresponds to  $W^2\delta^2/V_0^2 = -0.01$ .

The hybrid mode shown in Figure 4.4 is a result of the coupling of the main ballooning and KH modes. This mode behaves as a pure ballooning mode when  $k$  approaches 0. When  $k$  is extremely small,  $\gamma$  goes rapidly to 0 (not shown in the Figure). Figure 4.4 also shows that the hybrid mode is suppressed for  $k \geq 2/\delta$ . The KH vortex may develop only for  $k \leq 2/\delta$ , and the hybrid vortex spectra is also limited to these wavenumbers. At the same time, the linear analysis reveals the existence of noninteractive ballooning modes which develop independently in the system. As demonstrated in Figure 4.4, only noninteractive ballooning modes may develop in the system for  $k \geq 2/\delta$ , whereas the hybrid mode is suppressed.

The formation of both interacting and noninteracting modes is further explained in Figure 4.5. In this figure, the solid arrows show the direction of plasma motion due to the KH vortex whereas the empty arrows indicate plasma flow within ballooning cells. An initial perturbation, which develops into a vortex, is in phase

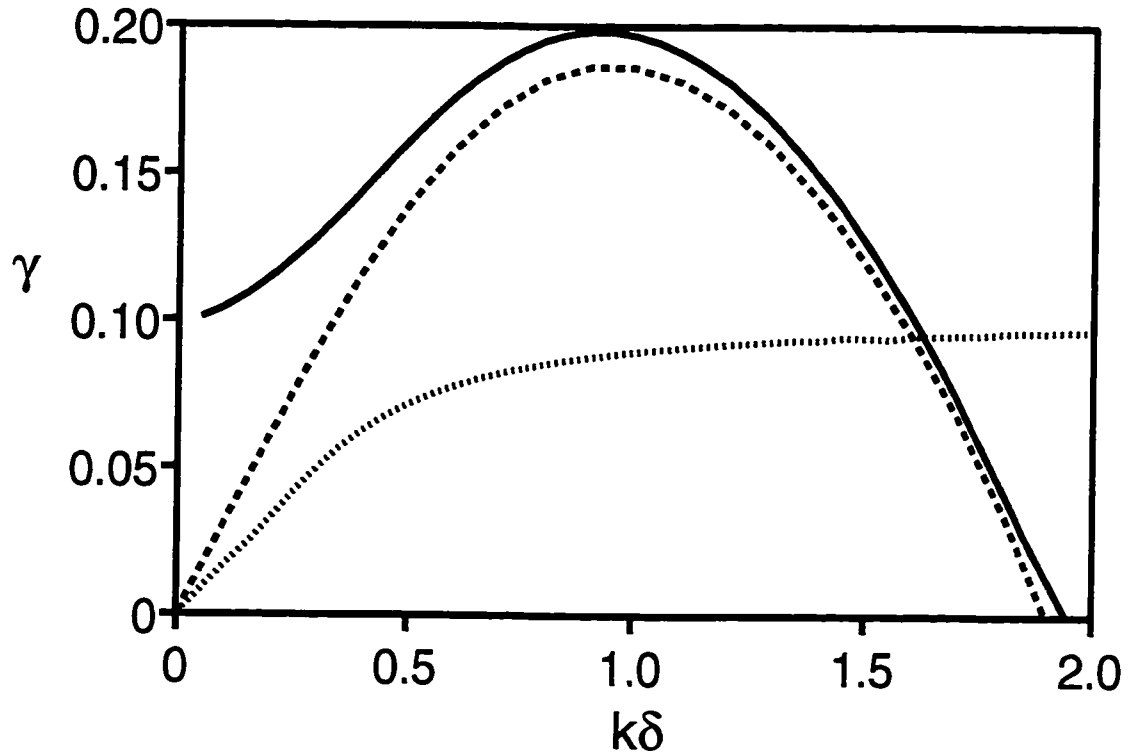


Figure 4.4: Growth rate  $\gamma = \text{Im}(\omega)\delta/V_0$  of the hybrid mode (solid line), KH instability (dashed line), and noninteractive ballooning mode (dotted line) as a function of  $k\delta$ . The growth rates for the hybrid and noninteractive modes are computed for  $W^2(\delta/V_0)^2 = -0.01$ .

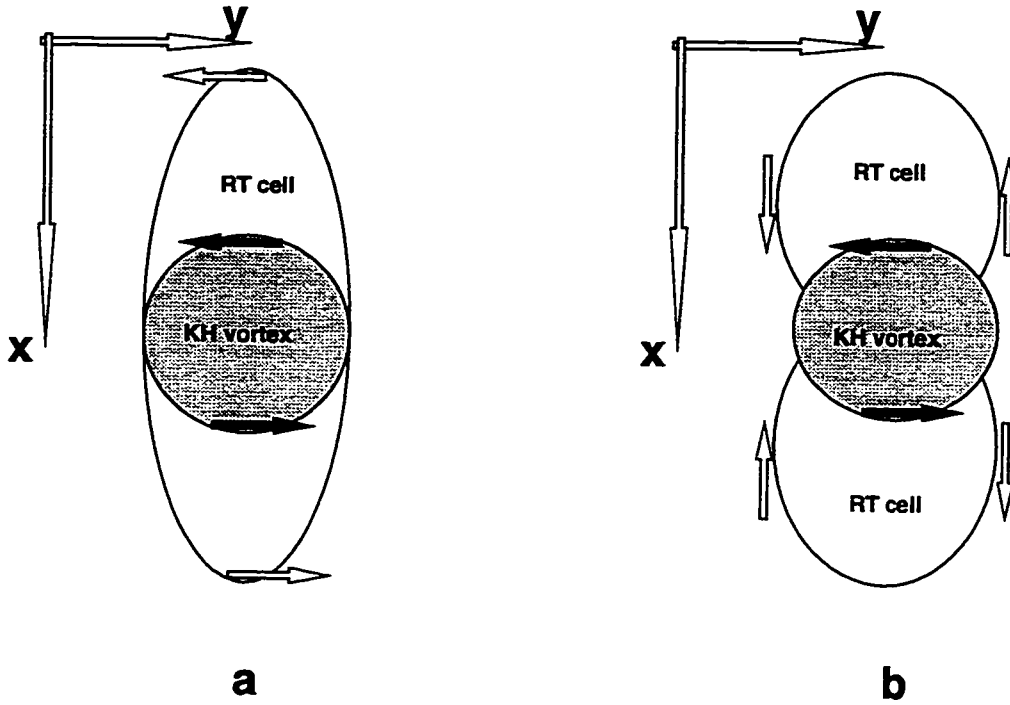


Figure 4.5: A model of the interaction of a shear flow vortex with ballooning modes of different radial scales: (a)  $k_x \sim 1/L$  and (b)  $k_x \sim 2/L$ . Arrows show the direction of the plasma motion due to the KH vortex (solid arrows) and ballooning cells (empty arrows) formation.

with a large scale ( $k_x \sim 1/L$ ) ballooning cell in Figure 4.5a. In this case the ballooning mode interacts with the vortex and coupling occurs. The growth rate of this mode corresponds to the solid line in Figure 4.4. Now let us consider the ballooning mode with the radial wavenumber  $k_x \sim 2/L$ . This ballooning mode is shown in Figure 4.5b and consists of two ballooning cells in the radial direction. It equally enhances (in the bottom part) and suppresses (in the top part) the shear flow vortex, providing a net contribution of zero.

## 4.3 Numerical Results

The results of the linear analysis of the hybrid instability have been compared with numerical solutions to the full set of MHD equations. The 2D simulations use the Alternating Direction Implicit (ADI) code described in chapter 2.

### 4.3.1 Vortex Evolution

In order to test the excitation and evolution of a hybrid vortex mode, a shear flow which is unstable to the KH instability was initiated in a plasma with a pressure gradient. The shear flow was chosen uniform in the  $y$ -direction, with a Gaussian profile in the  $x$ -direction of the form  $V_y(x) = V_0 \exp(-(x - x_0)^2/\delta^2)$ , where  $V_0 = 100$  km/s,  $\delta = 0.0425R_E$  and  $x_0$  is at the center of the simulation box in the radial direction. The length of our simulation box is  $1.5R_E$  in the radial direction and  $2\pi/k$  (one wavelength) in the azimuthal direction. The mesh consists of 100 points in the azimuthal direction distributed uniformly, and 120 points in the  $x$ -direction. The resolution in the  $x$ -direction varies from  $0.009R_E$  in the center of the box to  $0.017R_E$  at the boundaries. The initial plasma density and magnetic field were set as  $\rho = 4.06 \cdot 10^{-24}$  g/cm<sup>3</sup>, and  $B_0 = 0.0004$  G, respectively, with a uniform distribution in both the  $x$  and  $y$ -directions. The Alfvén speed corresponds to  $V_A = 560$  km/s, and the pressure corresponds to  $P = 4.35 \times 10^{-9}$  dyn/cm<sup>2</sup> at  $x_0$  and increases linearly along  $x$  (Earthward in our model) with  $\partial P/\partial x = 5.7 \times 10^{-9}$  dyn/cm<sup>2</sup>/ $R_E$ .

First of all, we study the growth of a hybrid mode with  $k = 0.7/\delta$ . For wavelengths  $k \sim 1/\delta$ , the growth rate of the ballooning instability is small compared to the growth rate of the KH instability in our model, which means that the extraction of potential energy from the ambient plasma, and the formation of the

ballooning cells, is slow. However, as predicted by the linear theory, the combination of a shear flow and a pressure gradient is expected to increase the growth of the vortex through the formation of a hybrid mode. The growth rate increase depends on the pressure gradient and it is about 10% for the chosen parameters of the slightly unstable ballooning mode. The growth of the initial perturbation of the radial component of velocity is shown in Figure 4.6a for hybrid, KH and ballooning modes, respectively. The velocity is normalized by  $V_A$ , whereas time is normalized by the Alfvén transit time  $t_a = L/V_A = 17.1$  s. Figure 4.6b shows the growth of the kinetic energy normalized by the initial total kinetic energy of the shear flow:

$$\Delta\varepsilon = \frac{\int \int \rho V^2 dx dy}{\int \int \rho V_0^2 dx dy} - 1. \quad (4.8)$$

Let us consider the evolution of the hybrid mode in more detail. The growth of the instability shown in Figure 4.6 implies that there are two different stages of evolution with different physical processes involved. We can distinguish the following stages: the linear growth and saturation of the KH-like vortex and the nonlinear growth and saturation of the hybrid vortex. Snapshots of the  $z$ -component of the vorticity  $(L/V_A)(\nabla_\perp \times \mathbf{V})_z$ , for  $t/t_a = 5, 7$  and  $10$ , respectively, which correspond to these stages of the instability evolution, are shown in Figure 4.7.

As seen in Figures 4.6 and 4.7, the first stage of the evolution,  $t/t_a \leq 6$ , corresponds to the linear formation of a KH-like vortex. For our choice of parameters,  $\gamma_{KH}$  is almost 2 times larger than  $\gamma_{bal}$ . Hence, the formation of a hybrid vortex is initially similar to the formation of a shear flow vortex with no pressure gradient in the plasma. However, the growth rate of the hybrid mode is slightly greater than for the KH mode because of the positive interaction of the KH instability with a large scale ballooning cell. At this stage of the vortex formation, the kinetic energy of



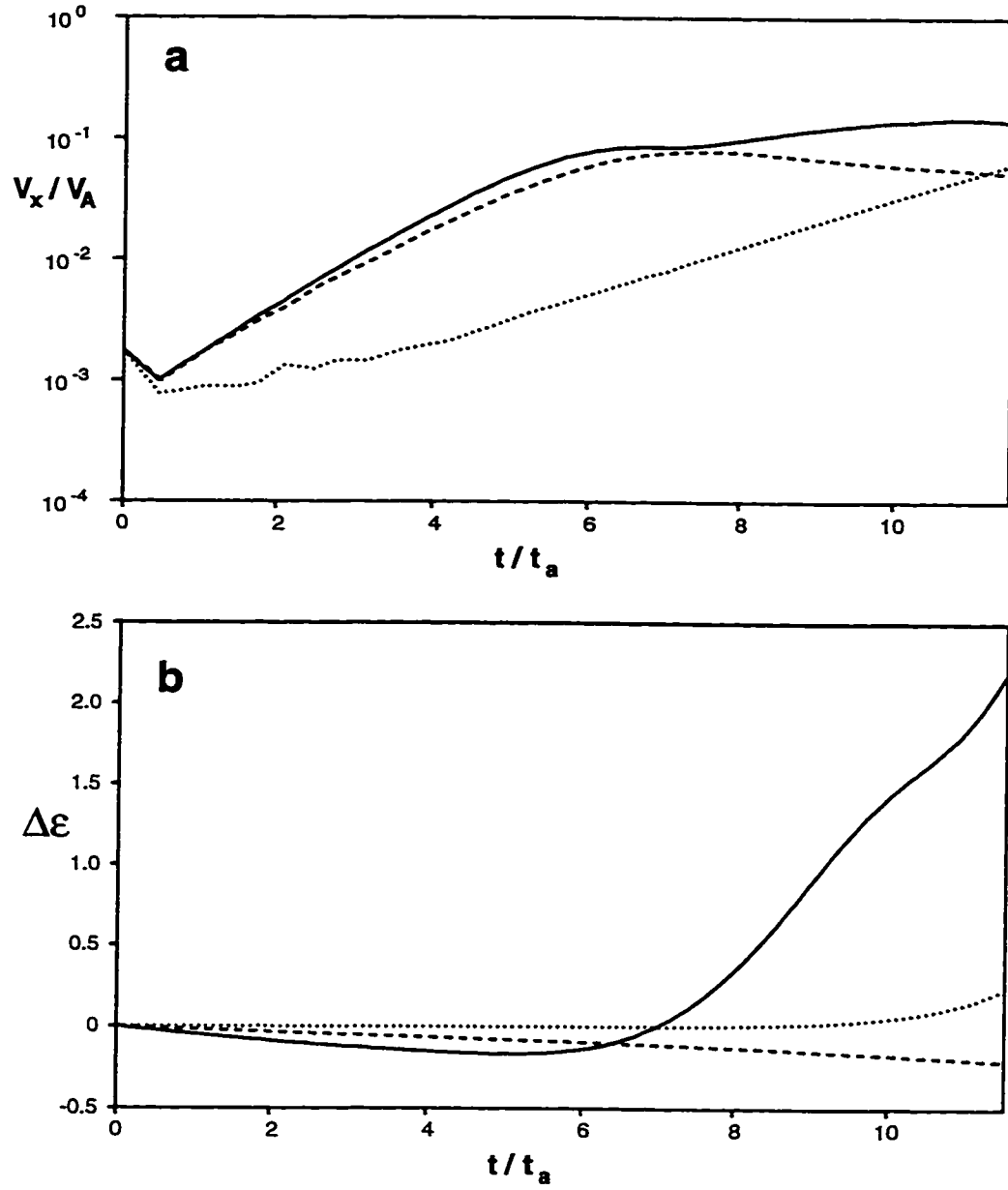


Figure 4.6: Growth of (a) amplitude of the radial velocity  $V_x$  and (b) the integrated kinetic energy of the hybrid mode (solid line), KH mode (dashed line) and ballooning mode (dotted line), respectively.

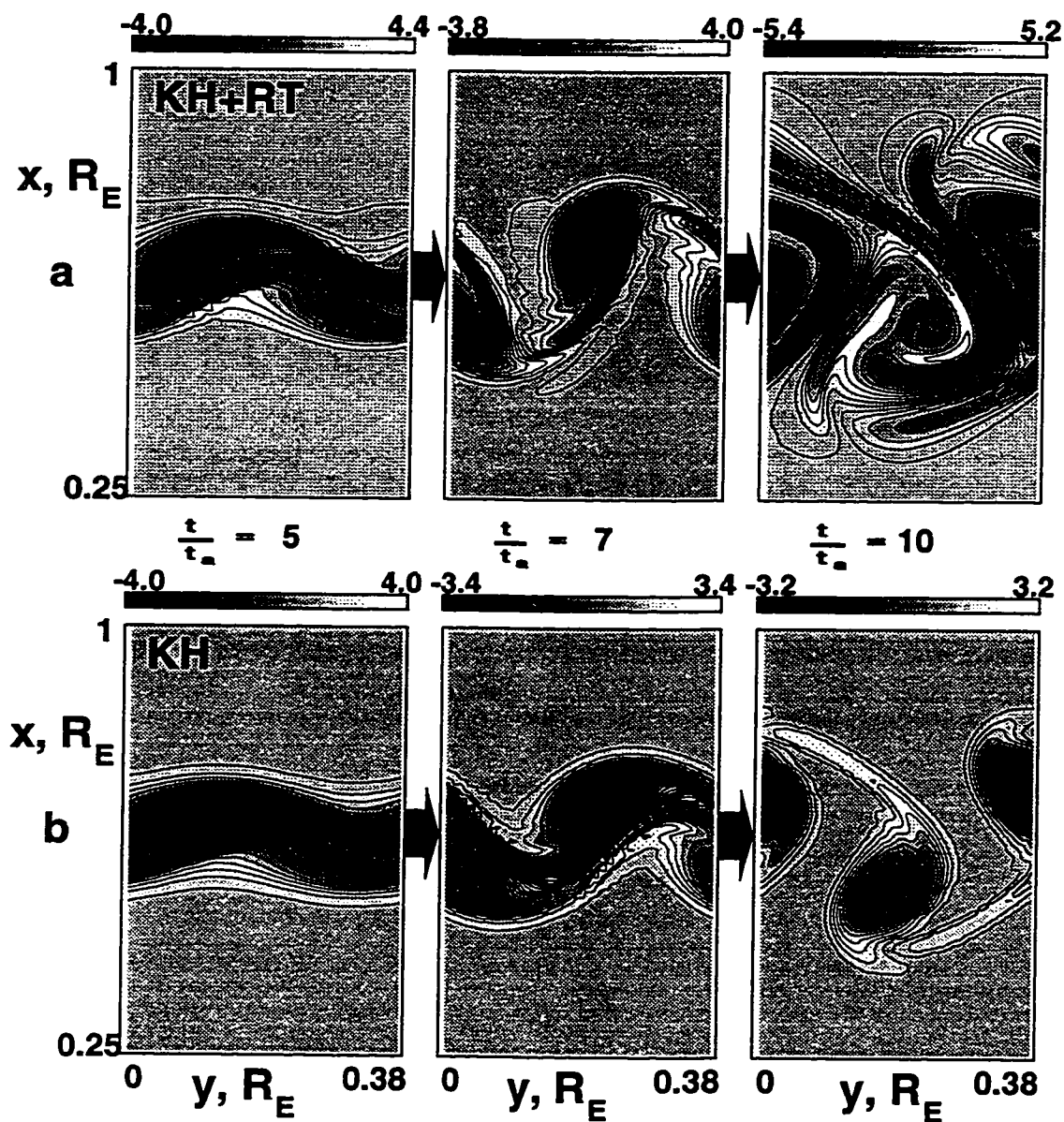


Figure 4.7: Time slices of the vorticity as obtained from the computer simulations for (a) the hybrid mode and (b) the KH instability, for  $t/t_a = 5, 7$ , and  $10$ .

the initial shear flow is transformed into vortex kinetic energy, but the total kinetic energy does not increase, which corresponds to  $\Delta\varepsilon \sim 0$  (c.f. Figure 4.6b). The insignificant trend downwards from zero is caused by the small numerical viscous damping which is required to stabilize the numerical scheme.

The linear growth rate was compared with predictions of the linear theory. The linear growth of  $V_x$  obtained from the simulations and predicted by (4.3) is shown in Figure 4.8 to prove that the results of computer simulations and analytical theory are in close agreement. Slightly spiky behavior of the numerical solution in Figure 4.8 is the result of adjustment of the initial perturbation to the KH eigenfunction.

The first linear stage of the evolution is complete by the time  $t/t_a \sim 6$ . The KH instability is then nonlinearly saturated due to the shear flow expansion in the radial direction (cf. Figure 4.7). At this stage, the hybrid vortex experiences a transition from KH-like to azimuthally moving ballooning-like mode. This transition is evident on comparing the contour panels of Figure 4.7, where it can be seen that billows are starting to form in the hybrid mode evolution.

Figure 4.9 demonstrates this transition stage for the main plasma parameters characterizing the instability: the radial component of the velocity, density, and plasma pressure. The significant changes observed in the density and pressure indicate the beginning of the nonlinear KH-ballooning interaction. The KH vortex defines the spatial shape of the cell and sets up a large perturbation from which further growth of the ballooning-like instability within the cell can occur. This provides a constructive interaction between the KH and ballooning modes and also explains why this transition stage is comparatively short,  $\Delta t/t_a \sim 1$ . As seen in Figure 4.9, a new ballooning cell is formed within the shear flow which has a radial

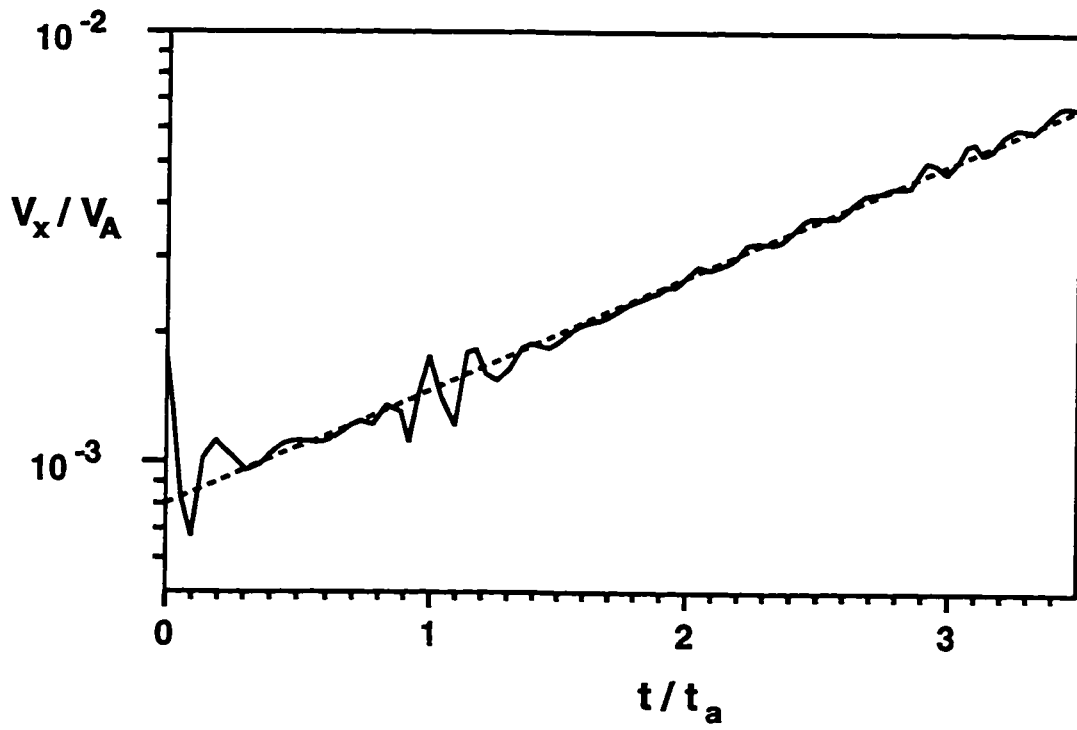


Figure 4.8: Linear growth of  $V_x$  obtained from the ADI code simulations (solid line) and as predicted by the linear theory (dashed line).

scale comparable to the width of the shear flow. The growth rate of the ballooning instability of this cell is smaller than the growth rate of the large scale cell which was associated with the linear stage of the evolution.

When the transition stage is over, the developed hybrid vortex continues to grow, as can be seen from an inspection of Figures 4.6 and 4.7 for  $t/t_a \geq 7$ . At this stage, the growth is slower than for the first stage and is comparable to the ballooning instability growth rate of a cell which has the radial scale of the shear flow. This growth is accompanied by an extraction of the ambient potential energy and its transformation into the kinetic energy of the vortex. The total kinetic energy of the vortex grows far beyond the value of kinetic energy of the initial shear flow. For this example, the energy of the hybrid vortex is approximately 3 times larger than the energy of the initial shear flow by the time  $t/t_a \sim 11$ . In contrast, the KH instability simulations indicate that a KH vortex with  $k\delta \sim 1$  can only extract about one half of the total shear flow kinetic energy.

At this nonlinear stage, the instability modifies significantly the spatial distribution of the shear flow and pressure. By the time  $t/t_a \sim 10$ , further growth of the radial component of the velocity is restricted by the boundaries of the expanded flow. Thus, a portion of the vortex flow is then directed along the outer boundaries of the shear flow in order to provide momentum conservation. This initiates secondary flows in the direction opposite to the initial shear flow, and leads to the azimuthally stretched and radially compressed flow structures shown in Figure 4.10. Figure 4.10 also displays a radial asymmetry, which is due to the radial gradient of the fast mode velocity  $V_f$ .

Saturation of the nonlinear hybrid vortex occurs when the vortex size in the radial  $x$  direction becomes comparable to the width of the zeroth order expanded

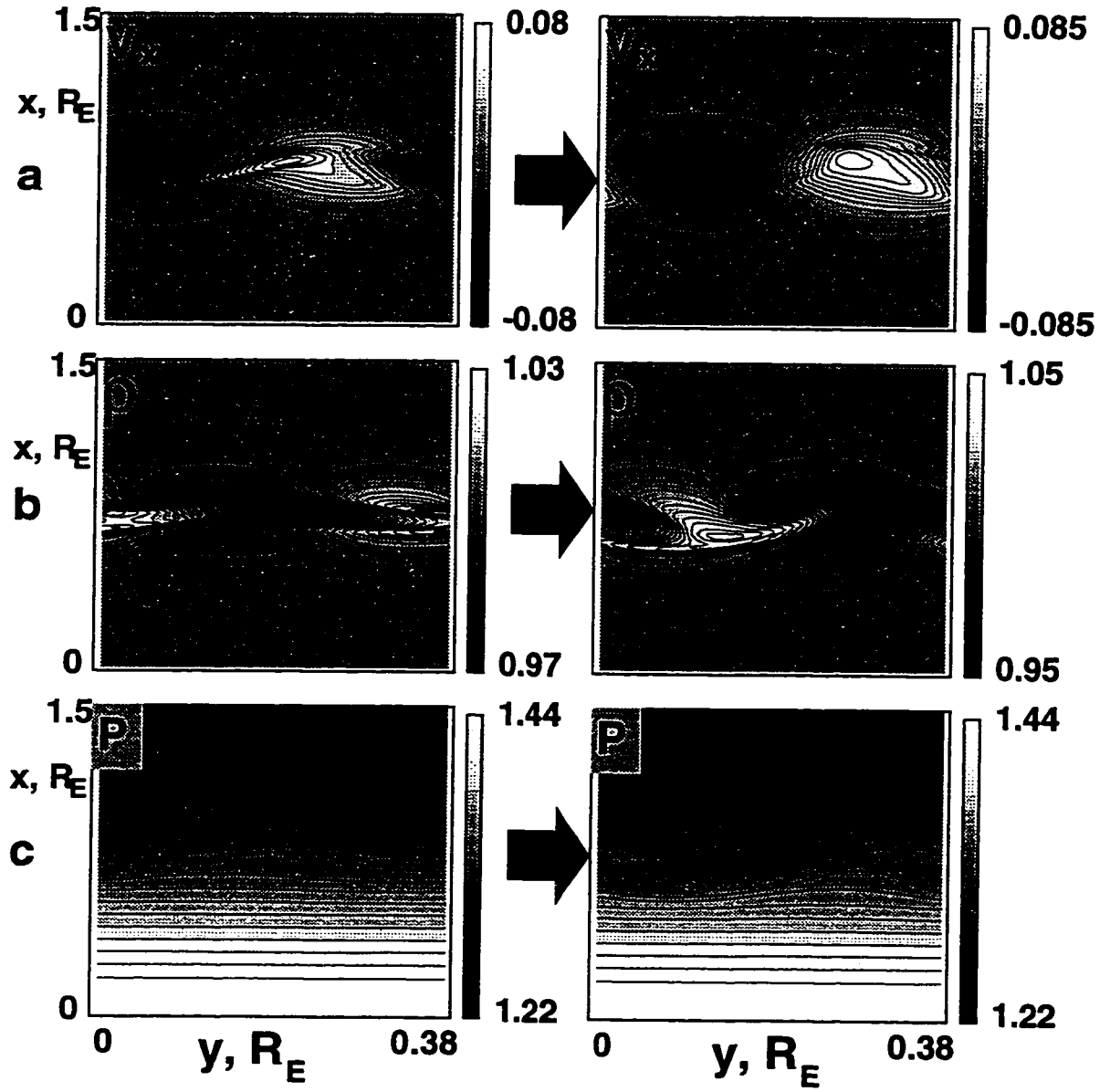


Figure 4.9: Contour plots of (a)  $V_x$ , (b) density and (c) plasma pressure for  $t/t_a = 6$  and  $7$ , respectively, illustrating the transformation of the hybrid eigenmode from KH-like to ballooning-like.

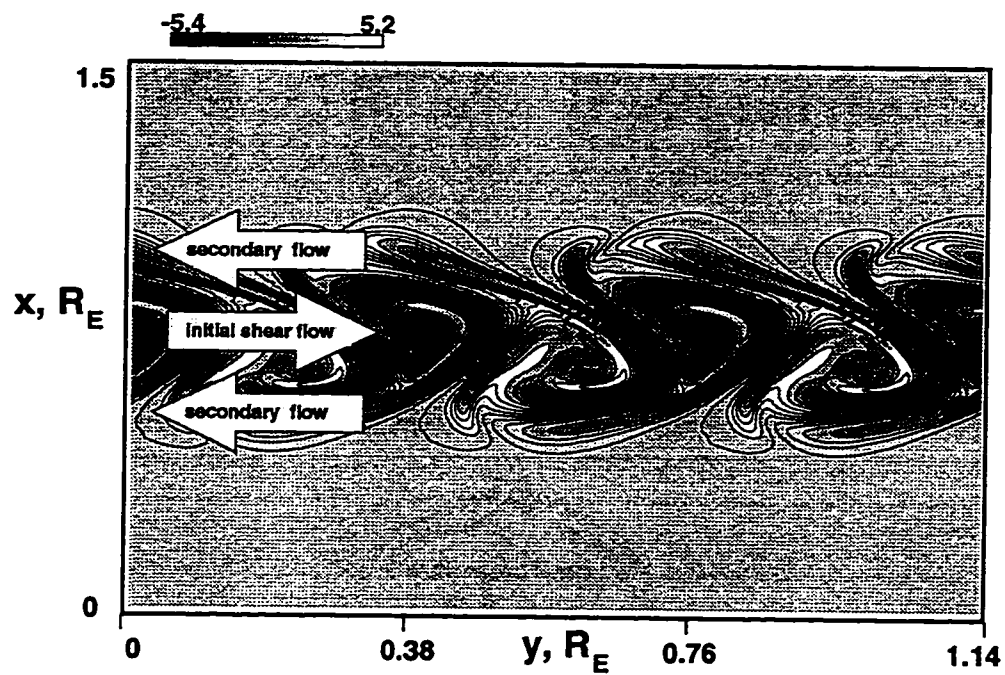


Figure 4.10: The vorticity of the hybrid mode for  $t/t_a = 10$ , demonstrating the generation of secondary shear flows which elongate the vortices in the direction opposite to the initial shear flow. Three wavelengths are combined in order to show a whole vortex structure.

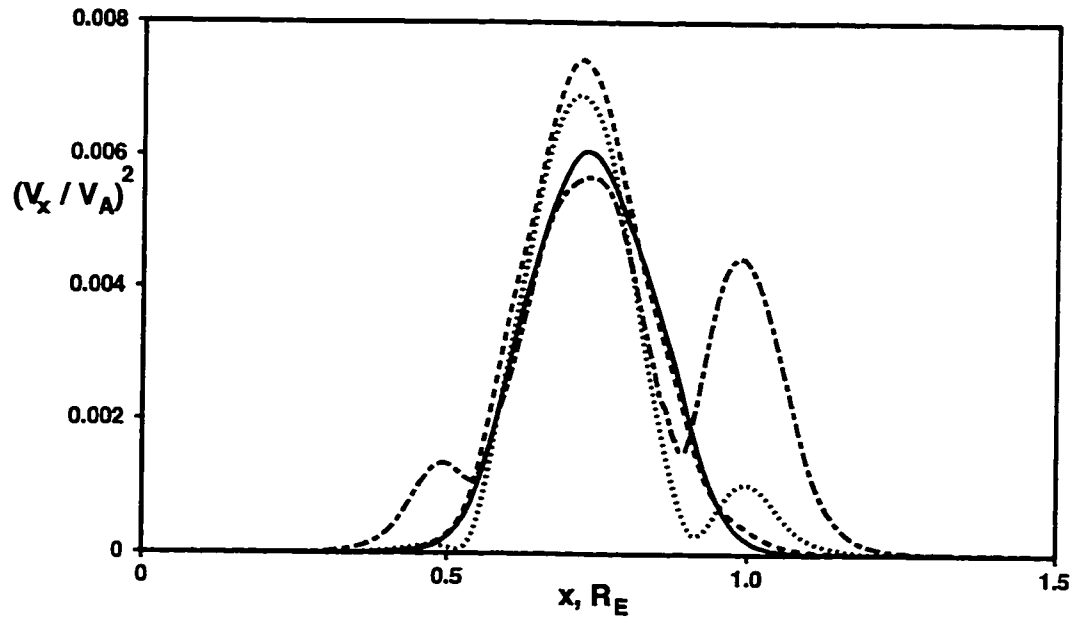


Figure 4.11: Radial distribution of the integrated radial kinetic energy  $\langle V_x^2 \rangle$ , at time  $t / t_a = 8.8$  (solid line), 9.8 (dashed line), 10.7 (dotted line), and 11.6 (dash-dotted line).



shear flow, which is then stable with respect to the KH instability. Nevertheless, new large amplitude perturbations of the radial component of the velocity appear in the secondary reversed flows discussed above. The resulting vortices can be clearly seen at the boundaries of the shear flow in Figure 4.10. These vortices provide for a further interaction with ballooning cells. Figure 4.11 demonstrates the radial distribution and time evolution of the radial kinetic energy  $\langle V_x^2 \rangle = k/(2\pi) \int_0^{2\pi/k} V_x^2 dy$ . The growth of the radial component of the velocity within the shear flow terminates at the time  $t/t_a \sim 10$ , whereas the perturbations which appear at the edge of the shear flow then start growing. This growth provides a further extraction of the potential energy and a corresponding growth of the kinetic energy of the newly generated vortex structures. This stage is seen in Figure 4.6b as kinetic energy growth which starts at  $t/t_a \sim 11$ . The latest nonlinear stage is similar to the edge effects of the ballooning-KH interaction described in the fusion literature [Drake *et al.*, 1992; Finn *et al.*, 1992; Finn, 1993].

### 4.3.2 Wavelength Dependence

The azimuthal size of the vortex is a parameter in our model and is defined by the wavenumber  $k$  of the initial perturbation. If the perturbation has a short wavelength ( $k \geq 2/\delta$ ), the hybrid mode is stable (cf. Figure 4.4) and only ballooning modes with larger wavenumbers in the radial direction (see Figure 4.5b) are unstable. The results of simulations for the mode  $k\delta = 1.8$  are presented in Figure 4.12a. In this case, the shear flow, which is stable with respect to the KH instability, divides the pressure gradient area into two parts, and the noninteractive ballooning mode predicted by the theory to be unstable (see Figure 4.5b) grows above and below the shear flow and stabilizes in the vicinity of the flow.

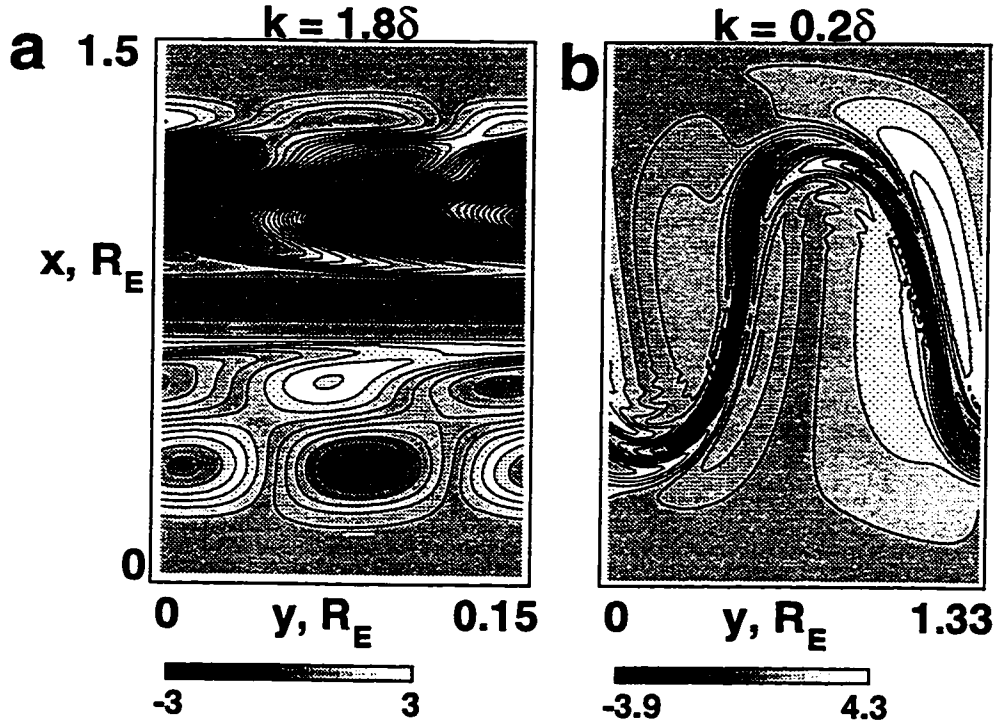


Figure 4.12: The vorticity for (a) small ( $k = 1.8/\delta$ ) and (b) large ( $k = 0.2/\delta$ ) wavelength perturbations.

In the other extreme case of large wavelengths, the hybrid mode is predicted to be unstable, but the ballooning component dominates. Thus the evolution of the hybrid vortex is defined by the ballooning instability, which evolves slower but leads to a strong deformation of the shear flow within the cell. The hybrid vortex takes the shape of a large scale fold, as shown in Figure 4.12b for  $k = 0.2/\delta$ .

### 4.3.3 Bi-directional (Antisymmetric) Flow

In the previous sections we considered a unidirectional Gaussian shear flow. We found that the hybrid mode extracts potential energy from the ambient plasma, but the extension of the vortex in the radial direction is restricted by the boundaries

of the initial shear flow. This restriction of the radial vortex expansion originates from the azimuthal motion of vortices and ballooning cells. Outside the region of the shear flow, ballooning cells no longer move in the azimuthal  $y$ -direction and the original hybrid vortex slides past the ballooning cells without interaction. This process may be illustrated using Figure 4.3 if we imagine that a vortex moves with the shear flow in the  $y$  direction. Then it provides a constructive interaction with a ballooning cell for a half period, when it is in between sections A and B, whereas the interaction is destructive when the vortex moves further to the right side of section A. Therefore, the motion of the hybrid vortex may turn off its interaction with a larger scale ballooning cell. This interaction may be restored if the vortex does not move with respect to the ambient plasma. These types of vortices are produced by the KH instability of a bi-directional (antisymmetric in the radial direction) shear flow.

We shall consider the evolution of a hybrid vortex for a shear flow defined by  $V_y(x) = 2.5V_0 \tanh((x - x_0)/\delta) / \cosh^2((x - x_0)/\delta)$  with  $V_0 = 50$  km/s and  $\delta = 0.0425R_E$ . Other parameters remain the same as in previous examples. The time slices of the vorticity of the hybrid mode are shown in Figure 4.13 for (a)  $k = 1/\delta$  and (b)  $k = 0.5/\delta$ .

The growth of the  $k = 0.5/\delta$  mode is slower during the initial linear stage, but in the nonlinear stage it grows faster and reaches a greater amplitude than for the mode with  $k = 1/\delta$ . Also, for the  $k = 0.5/\delta$  mode, the vortex expands into the broad area beyond the shear flow, whereas shorter wavelength modes are still bounded by the shear flow radial extent. These two cases may be explained by the difference that exists between the saturated state of the KH vortices. The mode with the shorter wavelength is immersed in the shear flow. It can interact only with moving ballooning cells and therefore cannot leave the region of the shear

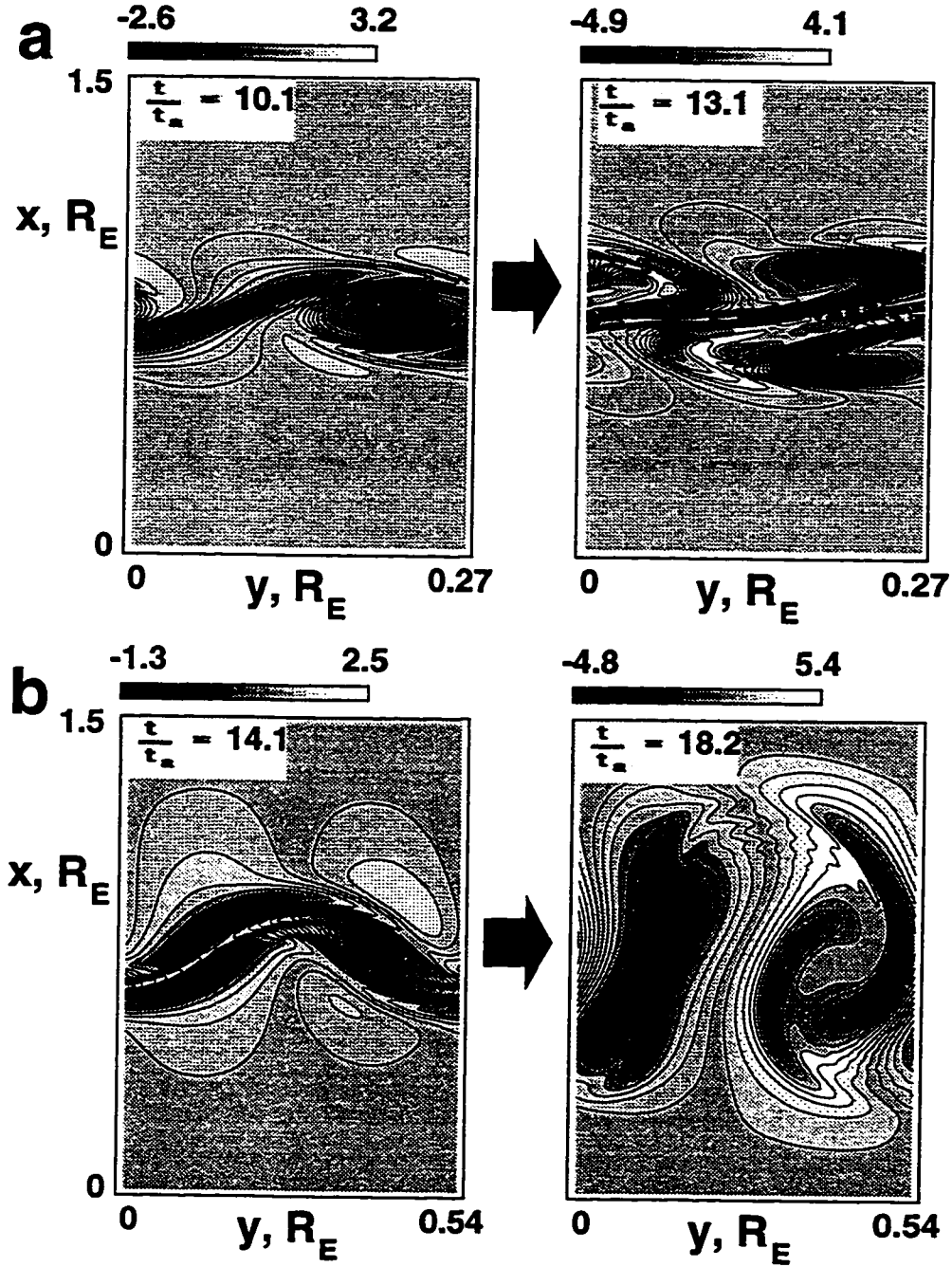


Figure 4.13: Time slices of the vorticity obtained from the computer simulations for the hybrid mode driven by a bi-directional shear flow with (a)  $k = 1/\delta$  ( $t/t_a = 10.1, 13.1$ ), and (b)  $k = 0.5/\delta$  ( $t/t_a = 14.1, 18.2$ ).

flow. Finally this mode saturates at the edges of the shear flow. This saturation is similar to the saturation of the hybrid mode which develops from the unidirectional flow as discussed in section 4.3.1. On the other hand, if larger scale perturbations develop in the bi-directional flow, they evolve into vortical structures that have two characteristic lengths: one scale involves small vortical structures within the flow and the second scale involves a larger distortion of the shear flow itself. This large scale distortion can easily interact with a large scale ballooning cell in the plasma gradient region. The resulting hybrid vortex expands in the radial direction finally destroying the initial shear flow and significantly extending the scale of the immersed vortical structures.

#### 4.4 Validity of the “Effective Gravity” Approach and Energy Balance in the System

An important result of the model considered above is that the vortex gains kinetic energy due to the work done by the “effective gravity force”  $\rho g = (-\rho V_z^2/R + B_z^2/4\pi R)\mathbf{e}_x$ . As discussed in chapter 1, this effective force can be used to describe the linear evolution of a 3D system using a 2D model. However, we showed above that an energy exchange in the system begins at the later nonlinear stage of hybrid mode evolution. At this stage, a nonlinear shear flow vortex interacts with a linear ballooning cell. Also, this vortex evolution can be affected by the boundaries of the shear flow. In this case, additional flows may appear which initiate secondary vortices. Therefore, at this stage of the instability we must exercise some caution before attempting to describe the process by a purely linear approximation of the effective force. Generally, 3D modeling is required to solve this problem exactly.

However, we can test the predictions of the 2D model using a different approach to the magnetic curvature force description.

Let us assume that the centripetal force  $\rho V_z^2/R$  is negligible and that the pressure gradient is in equilibrium with the magnetic curvature force  $B_z^2/4\pi R$ . In order to keep the approach two dimensional, we still need to assume that the radius of curvature does not change in time. However, this model appears to be an advance of the previous “effective gravity” model because it includes the nonlinear term  $B_z^2$  which can be important at the second and third stages of the evolution. Let us consider the results of simulations which include the curvature force  $B_z^2/4\pi R$ , and compare them with the results obtained for the “effective gravity” model.

The linear evolution of a hybrid vortex is described by the same dispersion relation (4.3) with

$$W^2 = -\frac{B_0 B'_0}{2\pi R \rho_0} - \frac{2B_0^4}{(4\pi R \rho_0 V_f)^2}. \quad (4.9)$$

As discussed above, if the initial density and ambient magnetic field are uniform, the linear solution to (4.3) does not depend on the form of  $W$ . Therefore the spectra presented in Figure 4.4 remain valid for this model as well.

Figure 4.14 shows the growth of the radial velocity  $V_z$  obtained using the ADI code for two dimensional MHD simulations with the curvature force modelled as an “effective gravity” (solid line) and as  $B_z^2/4\pi R$  (dotted line). For this example, the initial Gaussian shear flow and pressure gradient have the same radial distribution as defined in section (4.3.1), and the wavenumber  $k = 1/\delta$ . As seen from Figure 4.14, both models result in approximately the same growth of the instability at linear and transition stages whereas at the later nonlinear stage, the evolution may differ.

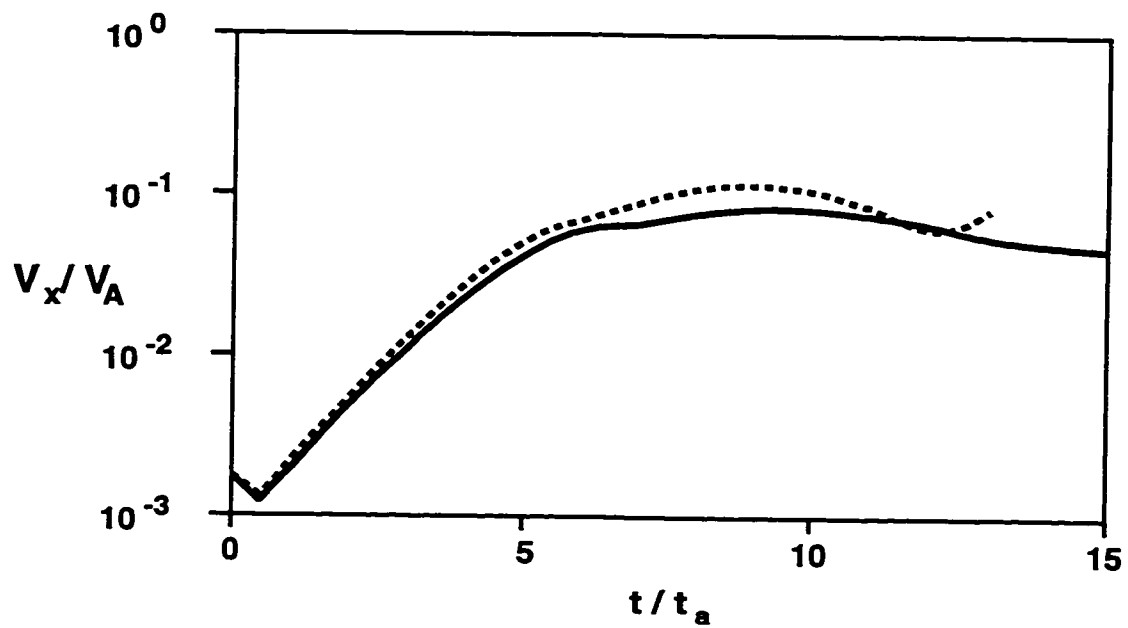


Figure 4.14: Growth of amplitude of the radial velocity  $V_x$  for two models: effective gravity (solid line) and curvature (dashed line).

However, an analysis of the interaction of vortices with ballooning cells revealed that the basic principles of the mode coupling obtained for the gravity model hold for the “magnetic curvature” model as well.

Let us consider the evolution of energy in the system. In the example below, we used an antisymmetric shear flow described in section (4.3.3) and a radial perturbation of velocity with  $k = 0.5/\delta$ . The growth of  $V_x$  for the shear flow ballooning (hybrid) mode (solid line) and the KH mode (dashed line) is presented in Figure 4.15a. The dynamics of energy in the system with the shear flow ballooning mode is shown in figure 4.15b. As seen from this figure, the total kinetic energy (solid line) is growing due to the work produced by the magnetic curvature force (dash-dotted line). The total energy stored in the plasma pressure gradient (dashed line) decreases and the energy of the magnetic pressure (dotted line) increases at the same rate. Therefore, the total pressure in the system does not change whereas the growth of the total kinetic energy occurs due to the work done by the magnetic curvature force. This result strongly suggests that the hybrid vortex extracts potential energy stored in the stretched magnetic field lines. The spatial distribution of the total kinetic energy at  $t/t_a = 14$  is shown in Figure 4.16. As seen from this figure, the main portion of kinetic energy is stored in the vortex.

## 4.5 Discussion

Our computer simulation of the interaction of the KH and ballooning instabilities has revealed a multi-stage evolution of the vortex structure. Initially, the vortex evolution is qualitatively similar to the pure KH instability. Quantitatively, the vortex develops faster in the presence of the pressure gradient due to the constructive interaction of a shear flow vortex with a large scale ballooning cell in the radial



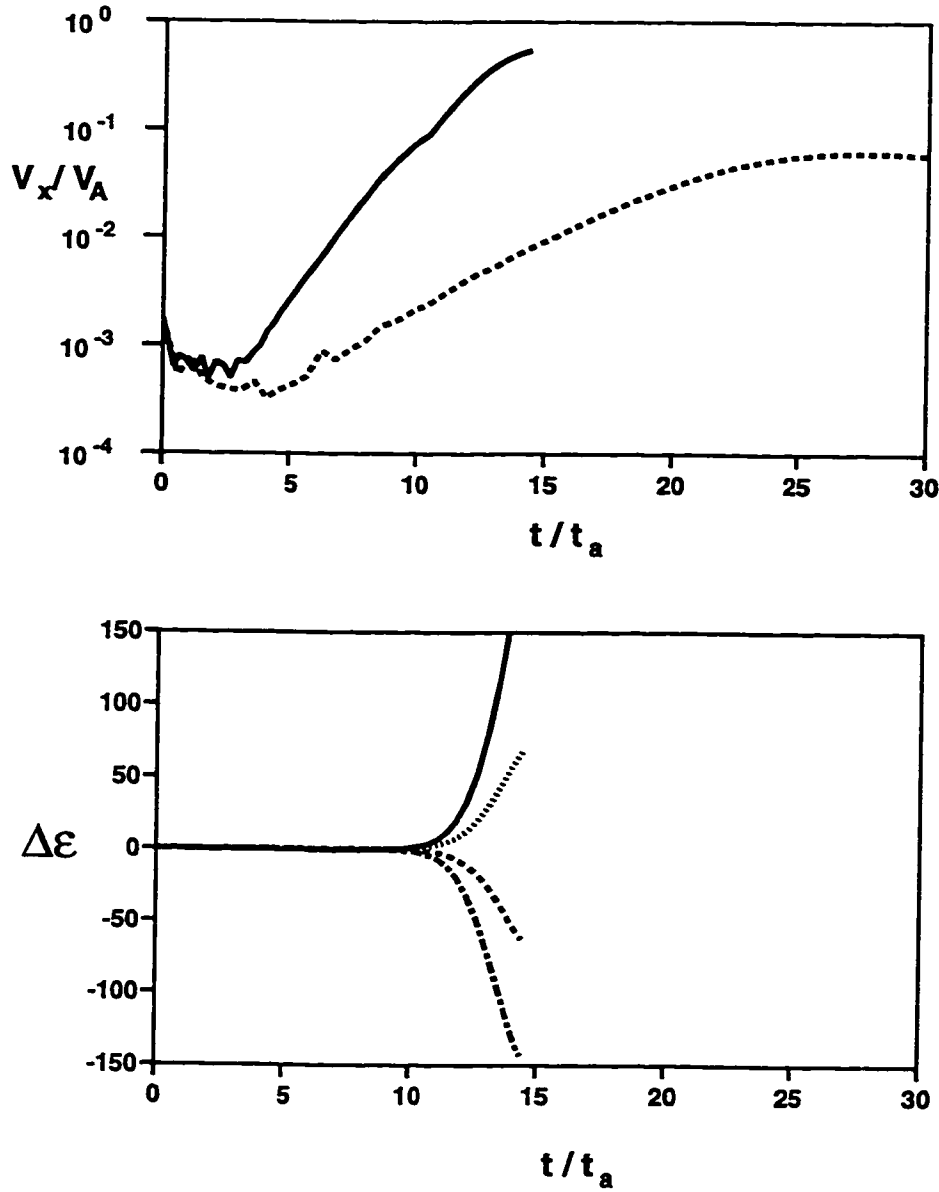


Figure 4.15: (a) Growth of the radial velocity amplitude of the hybrid mode (solid line) and KH mode (dashed line), respectively. (b) Evolution of kinetic energy (solid line), and potential energy due to the work done by the plasma pressure (dashed line), magnetic pressure (dotted line), and magnetic curvature (dash-dotted line) in the system with the hybrid vortex.

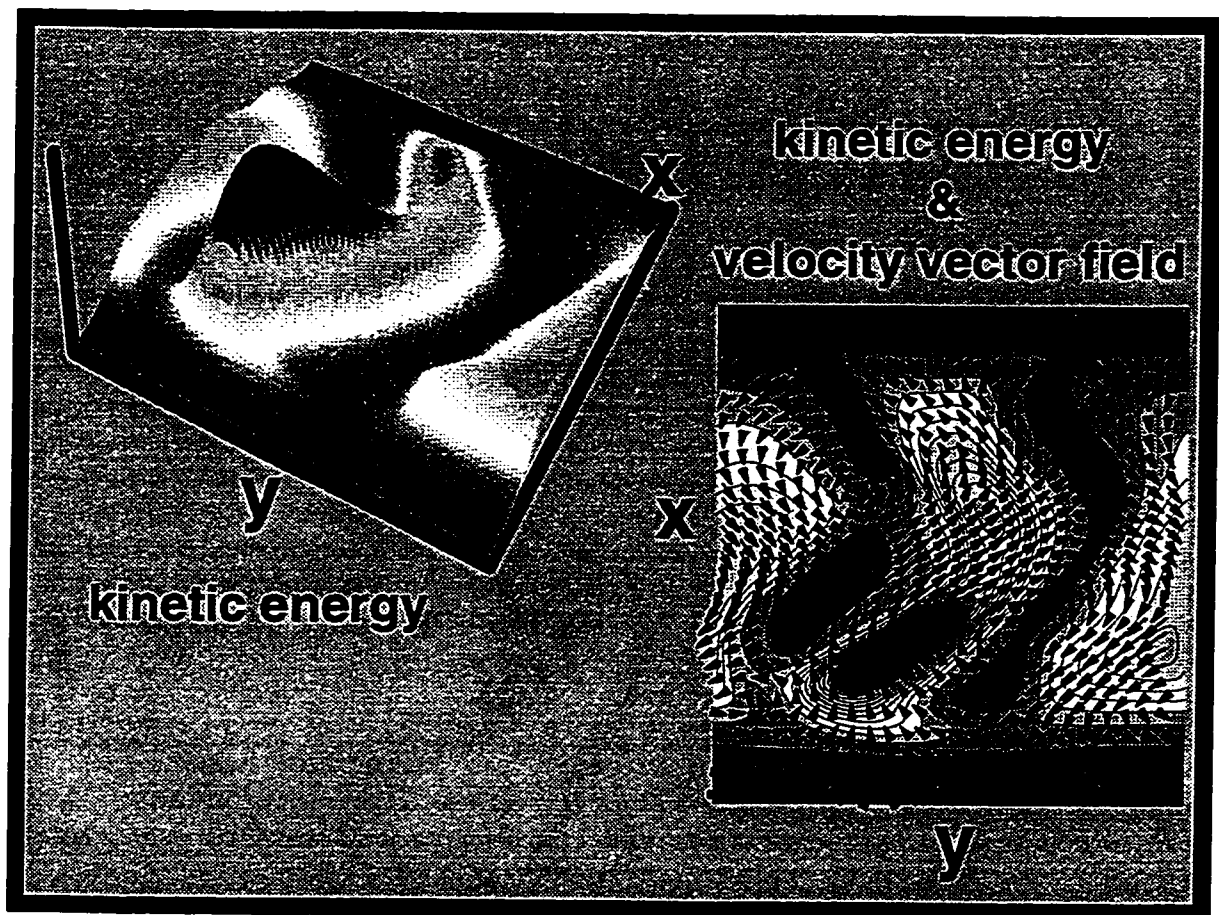


Figure 4.16: Spatial distribution of the kinetic energy and the velocity field associated with the hybrid vortex at  $t/t_a = 14$ .

direction. Later in time, the hybrid vortex extracts potential energy from the ambient plasma, providing for further growth of the kinetic energy of the vortex. This scenario suggests an explanation for observations indicating that only vortices in the late evening and midnight sectors, where the pressure gradient is large, may develop in association with vigorous surges, whereas vortices in the earlier evening sector appear and vanish without further evolution.

It follows from the simulations that perturbations with wavelengths  $k \sim 0.5/\delta$  imposed on a bi-directional flow can evolve into large amplitude surge-like structures which can destroy the original shear flow and expand over a wide region during a characteristic time of tens of seconds. Similar behavior was seen experimentally by *Steen and Collis* [1988] during observations of a westward travelling surge.

The theory and numerical results presented above are a simplified model of some of complicated processes in the inner plasma sheet. In this region, both radial and azimuthal pressure gradients may develop during the growth stage. A primary goal of our model was to consider a situation in which an unstable shear flow could interact with a background pressure gradient which is initially in equilibrium with the magnetic curvature force of stretched field lines. This force acts on the plasma in the Earthward direction and was assumed to be in the simple form  $\rho \cdot g$ , where  $g$  stands for a centripetal acceleration of the particles as a result of both magnetic curvature and particle inertia. Generally, magnetic curvature may vary in time as a result of the temporal evolution of magnetotail currents or through currents produced by the instability itself. Particle inertia may also change in time due to an acceleration along magnetic field lines and/or growth or decay of the parallel energy of the particles. In this model we have neglected these effects.

In this study, we have adopted a fluid model that neglects kinetic or finite

Larmor radius effects. This means that our model is valid for describing the evolution of structures with a spatial scale larger than the Larmor radius. For the sample shear flow and chosen density, the ion Larmor radius is smaller than the scale size of the vortices. However, if the initial shear flow is thinner, or if vortex fine structure is to be studied, ultimately kinetic effects should be taken into account. Kinetic and fluid-kinetic hybrid treatments have been presented by *Ganguli et al.* [1988]; *Thomas and Winske* [1993]; *Huba* [1996]. These studies revealed the importance of small scale effects and their influence on the growth rate and frequency of the shear flow instability. Also, the kinetic effects may be responsible for an asymmetry in the instability with respect to the centre of the flow [*Thomas*, 1995; *Huba*, 1996]. All of these small scale effects may be important for the auroral arc fine structure dynamics.

The other problem to be addressed is the importance of non-ideal MHD terms which violate the frozen field condition. The importance of the Hall term for the KH instability evolution was described by *Huba* [1994] for spatial scales on the order of the Larmor radius. We neglected this effect by assuming that the width of the flow is larger than the Larmor radius. Similarly, localized resistivity can initiate a large scale tearing mode [*Hesse and Birn*, 1994]. This mode can be driven by magnetic curvature [*Sundaram and Fairfield*, 1995; 1997], which implies that in a resistive plasma, additional hybrid modes are expected. The interaction of the shear flow and vortices with these modes seems to be a significant problem which might be addressed in future investigations.

The model presented in this chapter is also significantly simplified because we have neglected field aligned gradients of plasma parameters and have reduced our consideration to a 2D model of the equatorial plane of a symmetric magnetotail. Even though such an approach is limited in its ability to describe the full dynamics

of auroral arc intensifications, it has allowed us to obtain a simple solution to the problem which reveals some of the physical mechanisms that involve an acceleration and subsequent radial expansion of the vortex structure.

## CHAPTER 5

# Three Dimensional Evolution of Shear Flow and Ballooning Vortices

### 5.1 Introductory Remarks

As discussed in chapter 3, the small- $m$  SAWs in FLR regions may evolve into azimuthally extended and radially narrow channels which can eventually become unstable with respect to the KH instability. Evolution of this instability in the equatorial plane of the magnetosphere was studied in chapter 4. We showed that in the linear stage, the KH instability forms a vortex which grows with a characteristic time smaller than the fundamental SAW period typically observed in association with FLRs. In the presence of pressure gradients, this growth is even faster due to the interaction of the KH vortex with ballooning modes. However, in the model described in chapter 4, we assumed  $k_y \gg k_{\parallel}$  and therefore, we neglected all effects associated with the finite length of magnetic field lines and with the nonuniform field-aligned distribution of plasma parameters. Therefore, this model was further developed into the 3D dipolar model.

In this chapter, we consider shear flow and ballooning instabilities using 3D modeling which allows us to obtain a more realistic scenario for vortex formation and evolution. Since we expect that the growth rate of vortices will vary along the field line, these shear flow instabilities should excite field-aligned currents (FACs)

due to field-aligned velocity gradients. This process is similar to the FAC excitation due to field-aligned velocity gradients in SAWs (cf., equation 3.11). The FACs are of particular interest because they map the instability patterns into the ionosphere, and hence they permit a comparison with observations of auroral structures.

According to *Miura* [1996], an “auroral vortex street (curl) often seen in association with discrete auroral arcs is visible evidence of the K-H instability driven by the shear of the  $\mathbf{E} \times \mathbf{B}$  drift velocity”. *Miura* [1996] emphasized that the stabilizing effect of ionospheric line-tying can not be neglected whenever the KH instability  $e$ -folding time is comparable to or larger than the Alfvén wave transit time between the ionospheric boundaries. The influence of the ionospheric line-tying effect was studied by *Miura and Kan* [1992], *Galinsky and Sonnerup* [1994], and *Miura* [1996]. *Galinsky and Sonnerup* [1994] showed that for a sufficiently large ionospheric conductivity, the line-tying effect saturates the instability. *Miura* [1996] found a critical value of Pedersen conductivity  $\Sigma_{pe} \sim 1/(4\pi V_A)$  above which the KH instability is completely stable. However, some observations show that the characteristic time for the auroral vortex formation is of the order of tens of seconds for folds (length-scale of the order of 10 km) and of the order of seconds for curls (length-scale of the order of 1 km) [*Hallinan and Davis*, 1970; *Davis and Hallinan*, 1976; *Hallinan*, 1976; *Haerendel et al.*, 1996; *Trondsen and Cogger*, 1997; 1998]. This time-scale is much smaller than the field-aligned Alfvén transit time and therefore, the effect of line-tying might be small. These observations are in agreement with the shear flow instability  $e$ -folding time obtained in our simulations described in chapter 4. Also, as shown in chapter 3, the FLR may lead to a shear flow which is unstable with respect to the KH instability with an  $e$ -folding time smaller than the half-period of the fundamental SAW excited in the resonant region (see also *Rankin et al.* [1993a]). Therefore, one can expect that initially the KH instability in the Earth’s magnetosphere should

develop linearly in a similar fashion to that described in chapter 4. However, the effects associated with finite field line length may be extremely important in the nonlinear stage.

We use the ADI code to investigate the evolution of shear flow vortices in the course of the development of the shear flow instability in the dipolar magnetosphere. Our primary goal is to test the applicability of the 2D linear theory for this 3D curvilinear topology and to find mechanisms responsible for the generation of field-aligned currents and for the nonlinear saturation of the instability. The results are presented in section 5.2.

In section 5.3 we present preliminary results of the 3D ballooning mode analysis. For this study, we have developed a computer model in which magnetic field lines are stretched tailward from the dipolar topology.

As discussed in chapters 1 and 4, the inner plasma sheet configuration is favorable for the excitation of the ballooning instability [*Roux et al.*, 1991; *Kistler et al.*, 1992; *Holter et al.*, 1995]. These observations stimulated an extensive study of the ballooning instability. However, most theoretical works on the ballooning instability have dealt with the problem of ballooning and Alfvén mode coupling [*Miura et al.*, 1989; *Hameiri et al.*, 1991; *Lee and Wolf*, 1992; *Ohtani and Tamao*, 1993; *Chan et al.*, 1994; *Vetoulis and Chen*, 1994]. Since this coupling occurs due to the finite field-aligned wavelength of the ballooning mode, these earlier works have typically considered a time frame of several SAW periods, and have used models for the global magnetospheric equilibrium (e.g., *Kan* [1973]). In some papers, these modes are called the “ballooning modes” despite the diversity of the involved physical mechanisms. *Chan et al.* [1994] referred to these hybrid waves as Alfvén-ballooning modes which precisely reflects the origin of these modes.



*Lee and Wolf* [1992], *Ohtani and Tamao* [1993], and *Chan et al.* [1994] found that if the plasma pressure is isotropic, the interaction of “even” SAW harmonics with ballooning modes does not lead to instability. By “even” we mean those SAW harmonics for which the field-aligned distribution of the radial electric field is symmetric with respect to the equator. Stability of these Alfvén-ballooning modes suggests that they are unlikely to be a valid mechanism for auroral activations or substorm onset triggering [*Ohtani and Tamao*, 1993].

In this study, we deal with the ballooning mode dynamics within time frames which are smaller than the Alfvén wave transit time. As shown in Chapter 4, for typical magnetospheric parameters, ballooning cells can grow with the characteristic time of tens of seconds. During this time, this mode can allow the release of substantial energy from the ballooning unstable configuration. Our objective is to test this conclusion using the 3D ADI curvilinear model. We also assume that the ballooning unstable region is localized in the near-equatorial region of the plasma sheet. Compared to some other works dealing with the ballooning instability [*Miura et al.*, 1989; *Lee and Wolf*, 1992; *Ohtani and Tamao*, 1993; *Chan et al.*, 1994; *Vetoulis and Chen*, 1994], our analysis may be considered as “local” because of the smaller spatial and temporal scales of the processes considered.

## 5.2 Shear Flow Instability in the Dipolar Magnetosphere

Let us consider a fraction of the dipolar magnetosphere with an embedded azimuthal shear flow. Our simulations extend from  $L=9.25$  to  $L=10.75$  across the field lines ( $\nu$ -direction) and from the southern to the northern Earth’s ionosphere along the

field lines ( $\mu$ -direction). The azimuthal extent corresponds to one wavelength of the KH mode.

We shall consider evolution of a vortex which develops from the initial shear flow

$$V_{\phi 0} = V_0 \exp\{ -[(r_{eq} - r_{0,eq})/\delta]^2 \} \frac{[h_\nu B_0]_{eq}}{h_\nu B_0}, \quad (5.1)$$

where the subscript “eq” stands for the equatorial plane,  $r_{eq}$  is the radial distance in the equatorial plane,  $r_{0,eq} = 10R_E$ ,  $\delta = 0.057R_E$  is the half width of the flow in the equatorial plane,  $V_0 = 150$  km/s is the maximum of the shear flow velocity in the equatorial plane, and  $B_0$  is the ambient magnetic field.

The distribution of the shear flow velocity  $V_{\phi 0}$  in the  $(\mu, \nu)$  coordinate plane is shown in Figure 5.1. This flow represents a stationary shear flow in the dipolar coordinates. The field-aligned distribution of the initial shear flow defined by (5.1) allows us to separate the growth of the KH mode from background oscillations associated with standing SAWs. However, our results are valid for shear flows that support KH instabilities initiated by SAWs if the  $e$ -folding time of the KH instability is much smaller than the SAW period. The shear flow instability in this study was initiated by imposing an initial velocity perturbation  $V_\nu = 0.02 \times V_{\phi 0} \sin(k_\phi \phi)$  with an azimuthal wavelength  $\lambda_\phi = 2\pi\delta$ .

Using the fact that the width of the shear flow is much smaller than the length of the field line, we can assume that initially, the instability evolves similar to the 2D KH instability studied in chapter 4. If this assumption is valid, it allows us to develop a simplified theory of the instability which assumes that the evolution of vortices and their field-aligned interaction occur in different time scales. Therefore,

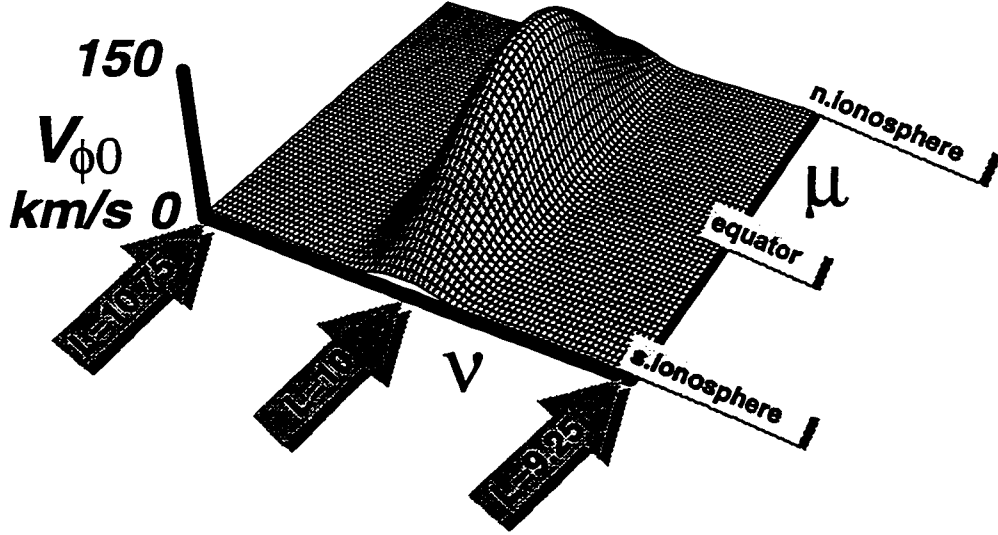


Figure 5.1: Distribution of the azimuthal shear flow velocity.

let us begin with comparisons of the results of 3D simulations with the predictions of the 2D theory and simulations.

Figure 5.2a shows the evolution of the vorticity  $(\nabla \times \mathbf{V})_{\parallel}$  in the equatorial plane during the linear ( $t = 20$  and  $40$  s) and nonlinear ( $t = 60$  and  $70$  s) stages. Vortex dynamics obtained from the 2D modeling is shown in Figure 5.2b. Comparing Figures 5.2a and 5.2b, we can see that the linear vortex evolution ( $t = 20$  and  $40$  s) is similar in the 2D and 3D models. In the nonlinear stage, 2D vortex evolves into a larger structure.

In Figure 5.3, the growth of the 3D KH instability in the equatorial plane is compared with the results of 2D simulations. As seen from this figure, the growth rate of the 3D KH instability is smaller than the growth rate in the 2D case. However, the characteristic time scales of the linear growth and nonlinear saturation

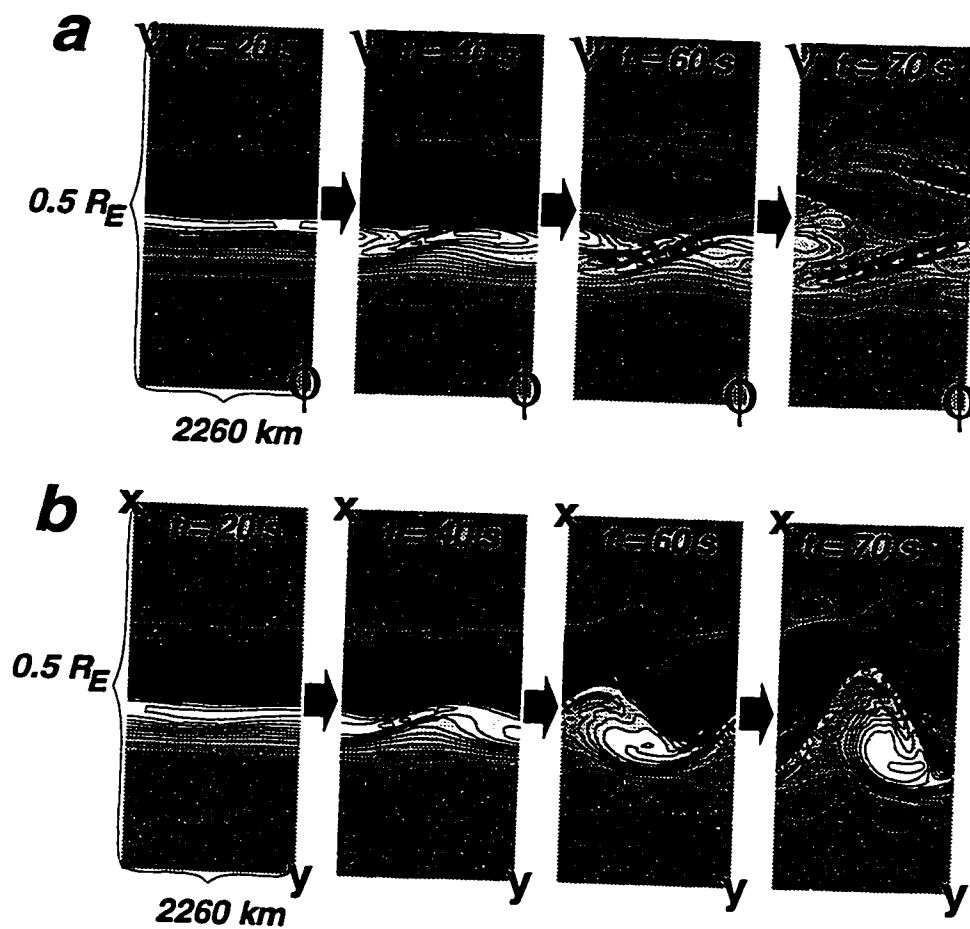


Figure 5.2: Time slices of vorticity in the equatorial plane for  $t = 20, 40, 60,$  and  $70$  s obtained using (a) 3D and (b) 2D models.

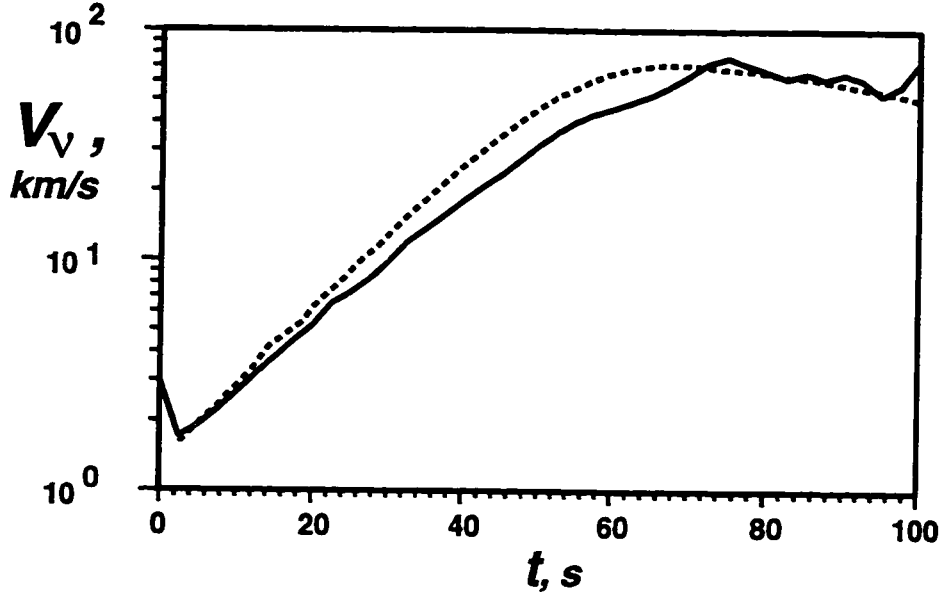


Figure 5.3: Growth of the  $V_v$  amplitude at the equatorial plane as obtained from the 3D (solid line) and 2D (dashed line) models.

are similar in both models. It is necessary to mention that artificial viscosity and resistivity required to stabilize the code with respect to small numerically unstable harmonics is smaller ( $\sim 2$  times) in 3D simulations than in 2D. In 3D simulations, these numerically unstable harmonics can escape along the field lines from the region where they originate. This provides higher numerical stability of 3D simulations.

The distribution of  $V_v$  in  $(\nu, \phi)$  planes (perpendicular to the field line) is shown in Figure 5.4 for different altitudes along the field line. An eigenfunction of  $V_v$  predicted by the 2D theory for parameters corresponding to the equatorial plane is also shown in this figure (Figure 5.4d). This figure also suggests that the 2D theory of the KH instability provides us with appropriate predictions for the linear KH mode evolution in the dipolar 3D model.

All these results show that for the chosen parameters, the linear 3D and

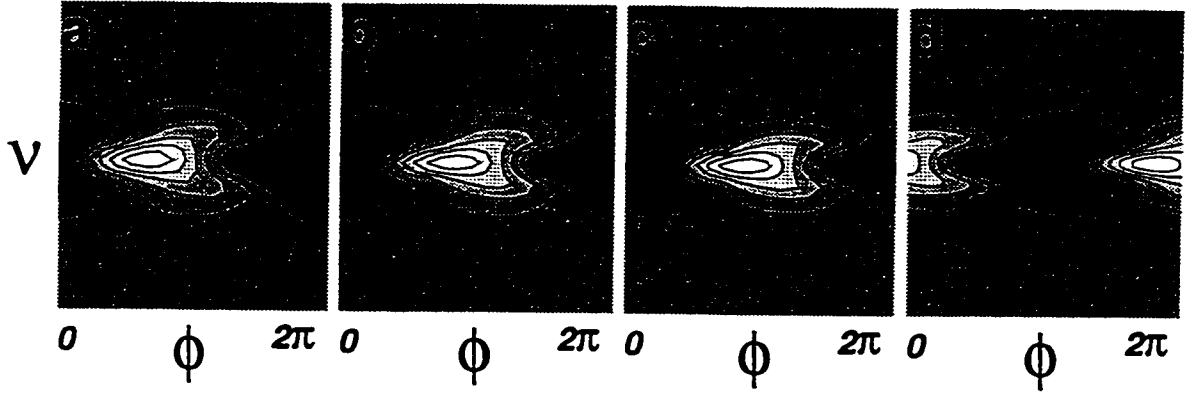


Figure 5.4: Radial ( $\nu$ ) and azimuthal ( $\phi$ ) distribution of  $V_\nu$  at (a)  $3.1R_E$ , (b)  $8.3R_E$ , and (c)  $13.5R_E$  along the field line and (d) a KH eigenmode predicted by the 2D theory.

2D KH instabilities evolve similarly. However, in the 3D case, there is a weak field-aligned interaction (or energy exchange) between vortices at different altitude levels. This interaction should be accounted for in order to obtain accurate growth rates of the 3D instability. Below, we develop a simplified linear analytical model of the KH instability in the dipolar coordinates which can explain the field-aligned vortex coupling in terms of currents produced by the instability.

The linearized MHD equations in dipolar coordinates can be reduced to

$$-i\Omega_{KH}\rho_0 V_\nu = -\frac{1}{h_\nu} \frac{\partial P}{\partial \nu} + \frac{1}{c} j_\phi B_0, \quad (5.2)$$

$$-i\Omega_{KH}\rho_0 V_\phi = -\rho_0 \frac{V_\nu}{h_\nu} \frac{\partial V_{\phi 0}}{\partial \nu} - \frac{1}{h_\phi} \frac{\partial P}{\partial \phi} + \frac{1}{c} j_\nu B_0, \quad (5.3)$$

$$-i\Omega_{KH}\rho + \rho_0 \nabla \cdot \mathbf{V} = 0, \quad (5.4)$$

$$-i\Omega_{KH}P + \rho_0 C_S^2 \nabla \cdot \mathbf{V} = 0, \quad (5.5)$$

where  $\Omega_{KH} = \omega - kV_{\phi 0}/h_\phi$  is the Doppler shifted frequency in the dipolar coordinates,  $\rho_0$  is the ambient density, and  $k$  is the azimuthal wave number. These

equations give the dispersion relation for the instability as:

$$\frac{h_\phi^2}{h_\nu^2} V_\nu'' = k^2 V_\nu \left(1 - \frac{h_\phi^2}{h_\nu \Omega_{KH} k} V_{\phi 0}''\right) + \frac{h_\phi B_0 k}{c \rho_0 \Omega_{KH}} (\nabla \cdot \mathbf{j})_\perp, \quad (5.6)$$

where  $V_\nu'' = d^2 V_\nu / d\nu^2$  and  $(\nabla \cdot \mathbf{j})_\perp$  is current divergence perpendicular to field lines.

The influence of the term  $\frac{h_\phi B_0 k}{c \rho_0 \Omega_{KH}} \langle (\nabla \cdot \mathbf{j})_\perp \rangle$  can be understood as follows. Using  $\nabla \cdot \mathbf{j} = 0$ , this term can be written in the form  $\frac{\xi(\mu) k}{\Omega_{KH}} \frac{\partial}{\partial \mu} (h_\mu j_\mu)$ , where  $\xi(\mu)$  is a coefficient which depends only on the  $\mu$  coordinate. The field-aligned current  $j_\mu$  is driven by the field-aligned gradient of the vorticity. Hence, let us assume that  $j_\mu \sim \nabla_\parallel \cdot (\nabla \times \mathbf{V}) \sim \nabla_\parallel k V_\nu$ . Then the field-aligned coupling term in (5.6) can be evaluated as  $\alpha(\mu) k^2 / \Omega_{KH} |\nabla_\parallel^2 V_\nu|$ , where the coupling coefficient  $\alpha(\mu)$  varies in the range  $\sim [-0.2; 0.2]$  in the problem. The sign of  $\alpha$  depends on the sign of  $\nabla_\parallel^2 V_\nu$ . The dependance of the instability growth rate and frequency on  $\alpha$  is shown in Figure 5.5 for the  $\lambda_\phi = 2\pi\delta$  KH mode. As seen in this figure, the field-aligned vortex coupling tends to diminish the field-aligned variations of vortex amplitudes. Whenever  $\nabla_\parallel^2 V_\nu$  is negative,  $\alpha$  is negative which reduces the growth rate and frequency, and vice versa.

The field-aligned distribution of the phase velocity is presented in Figure 5.6 as obtained from the 3D simulations and as predicted by the 2D theory. As seen from this figure, field-aligned dispersion causes a nonuniform field-aligned distribution of the KH mode phase velocity. The phase velocity variation leads to a phase shift between the vortices at different altitudes. This shift causes the excitation of oblique Alfvén waves as shown in Figure 5.7. It is interesting to note that the phase shift of vortices at different altitudes above the ionosphere can reach  $\sim \pi$  before the KH instability saturates. The convection patterns in the ionosphere and at  $\sim 3R_E$  above the ionosphere are shown in Figure 5.8 for  $t = 50$  s. As seen from the

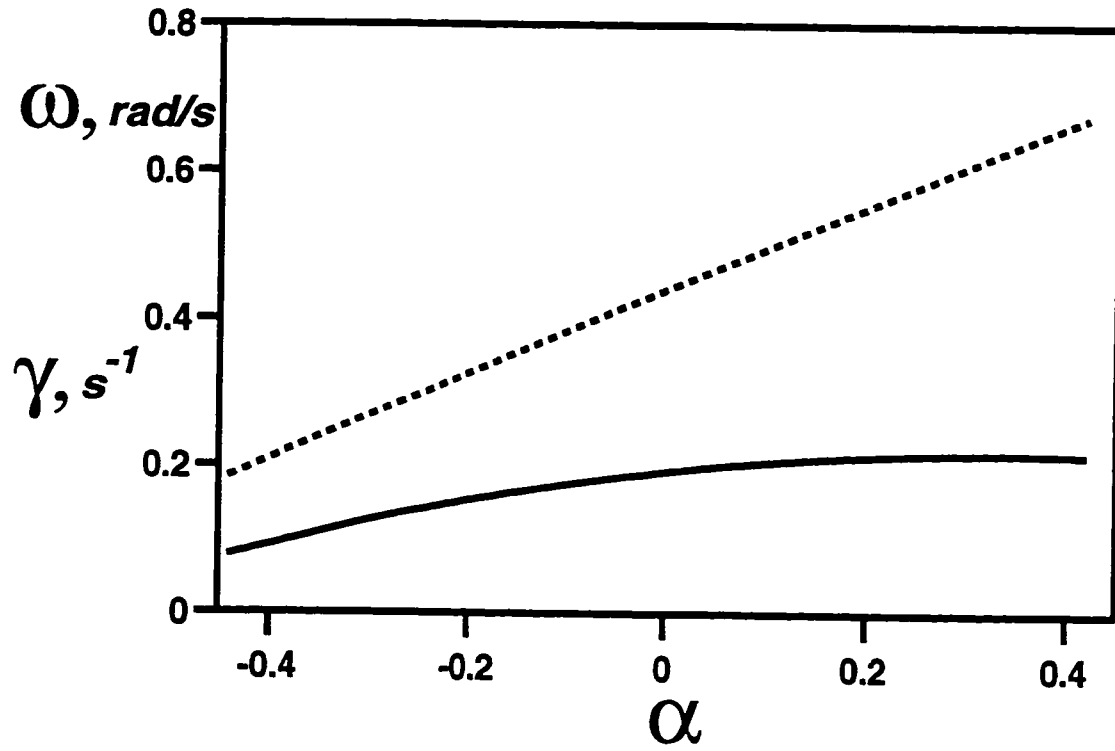


Figure 5.5: Dependence of the growth rate (solid line) and frequency (dashed line) on the coupling coefficient  $\alpha$ . The growth rate and frequency are normalized by  $\delta/V_0$ .



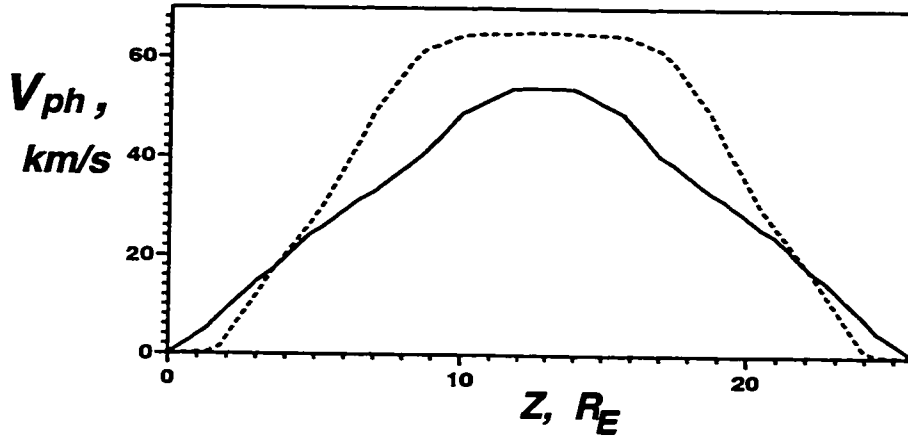


Figure 5.6: Field-aligned distribution of the phase velocity obtained from the 3D simulations (solid lines) and as predicted by the 2D theory (dashed lines).

figure, plasma flow wraps anticlockwise in the ionosphere and clockwise at  $\sim 3R_E$  poleward from the initial shear flow. Equatorward from the flow, the rotation is clockwise at the ionosphere and anticlockwise at  $3R_E$  above. Therefore, this phase shift can be proposed as a candidate mechanism responsible for the opposite rotation of ionospheric convective cells and luminosity patterns which reflect plasma vortical motion at  $\sim 2 - 3R_E$  above the ionosphere where the electron acceleration occurs. As discussed in Chapter 1, this effect is often observed in association with discrete arcs [Davis, 1978; Haerendel *et al.*, 1993, 1996; Frey *et al.*, 1996]. However, qualitative comparisons of the simulation results with observations require further model development including inhomogeneous distribution of the ionospheric conductivity which can significantly modify ionospheric convection patterns.

The nonuniform distribution of the velocity perturbation due to field-aligned variations in the growth rate, frequency, and phase velocity initiates perturbations in the magnetic field. These magnetic field perturbations define the field-aligned current structure above the ionosphere which may be of particular interest with

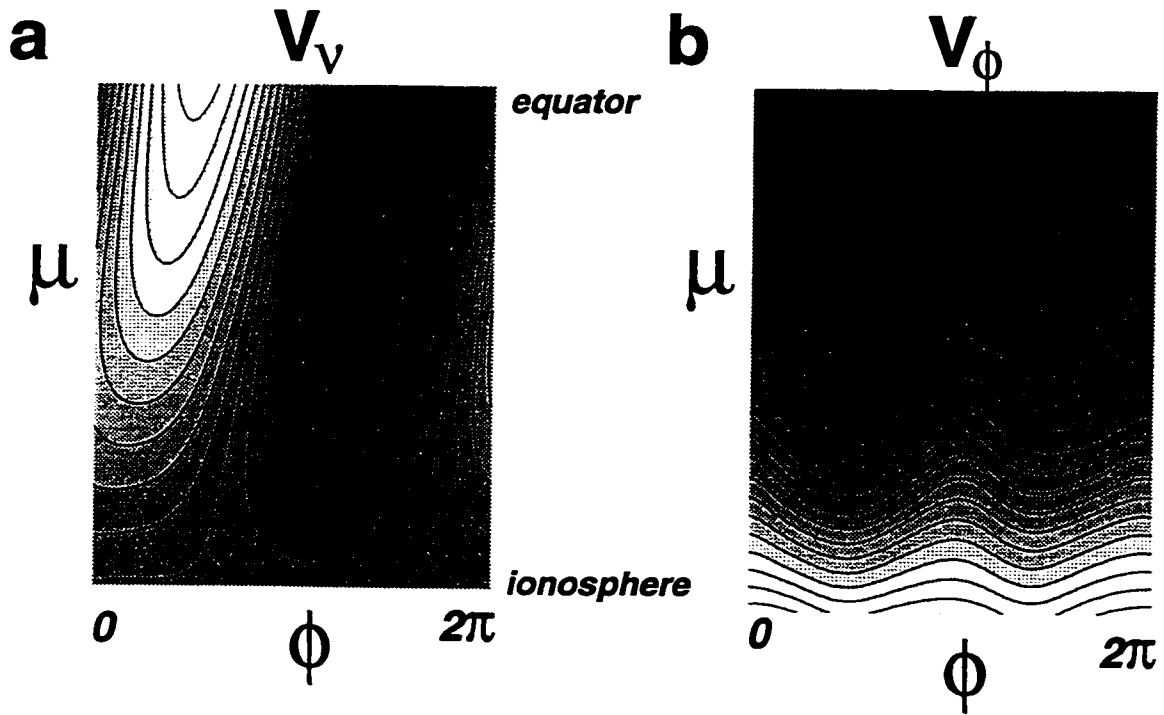


Figure 5.7: Field-aligned ( $\mu$ ) and azimuthal ( $\phi$ ) distribution of (a)  $V_v$  and (b)  $V_\mu$  perturbations (main harmonic) at  $t = 10$  s.

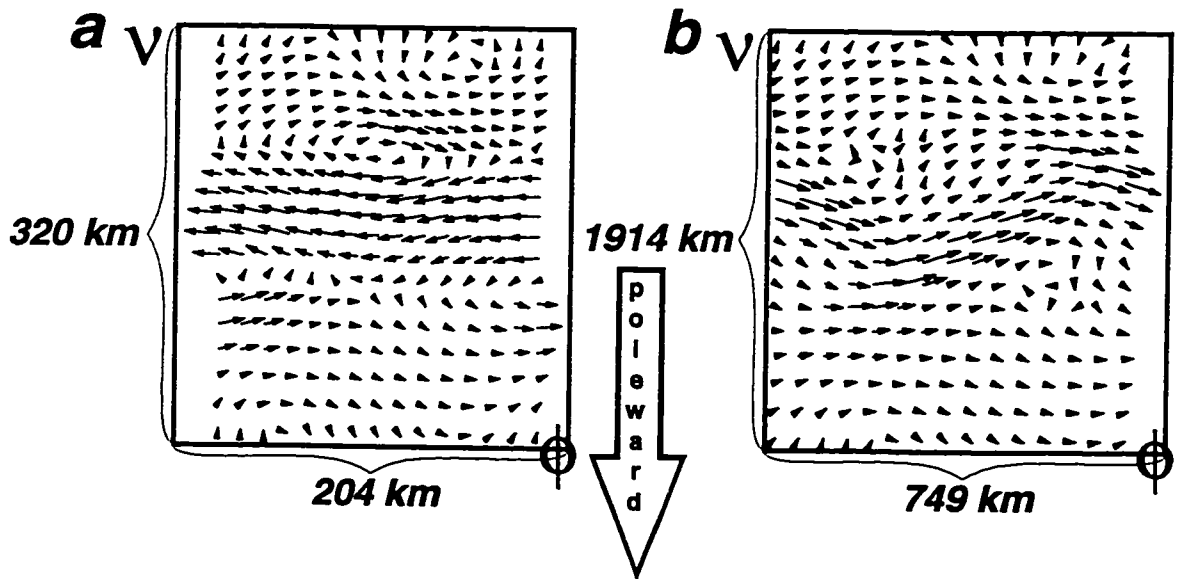


Figure 5.8: Velocity field distribution in (a) the ionosphere and (b) at  $\sim 3R_E$  above the ionosphere at  $t = 50$  s.

respect to comparisons with observations. Therefore, let us consider the problem of how the KH instability modifies the magnetic field in the vicinity of the ionospheric boundaries.

Linearized equations for the magnetic field components  $B_\nu$  and  $B_\phi$  which are responsible for the field-aligned current formation are:

$$\frac{\partial B_\nu}{\partial t} + \frac{1}{h_\mu h_\phi} \left( \frac{\partial}{\partial \phi} h_\mu V_{\phi 0} B_\nu - \frac{\partial}{\partial \mu} h_\phi V_\nu B_0 \right) = 0, \quad (5.7)$$

$$\frac{\partial B_\phi}{\partial t} + \frac{1}{h_\mu h_\nu} \left( \frac{\partial}{\partial \mu} h_\nu V_\phi B_0 \right) = 0, \quad (5.8)$$

where  $B_0$  is the ambient magnetic field. In equation (5.8), we have assumed that near the ionosphere,  $\partial B_\mu / \partial t = 0$ . Magnetic field components can be presented as  $B_{\nu,\phi} = \text{Re}[b_{\nu,\phi}(t) \exp(-i(\omega t - k\phi))]$ . As seen from Figure 5.5, vortex eigenfunctions can be assumed independent of  $\mu$ . This allows us to separate variables for  $V_\nu$  and  $V_\phi$ :  $V_{\nu,\phi} = V_{\nu,\phi 0}(\mu) \xi_{\nu,\phi}(\nu) \exp(-i(\omega t - k\phi))$ , where  $V_{\nu,\phi 0}(\mu)$  are the initial amplitudes and  $\xi_{\nu,\phi}(\nu)$  are the eigenfunctions. Then, the solutions for  $b_\nu$  and  $b_\phi$  are:

$$b_\nu = C_1(e^{i\Omega_{KH}t} - 1) + C_2t, \quad (5.9)$$

$$b_\phi = C_3(e^{i\omega t} - 1) + C_4t, \quad (5.10)$$

where the coefficients  $C_{1,2,3,4}$  are:

$$C_1 = \frac{iB_0}{h_\phi \Omega_{KH}^2} \left( \frac{V_{\nu 0}}{h_\nu} \frac{\partial \omega}{\partial \mu} - \Omega_{KH} \frac{\partial}{\partial \mu} \frac{V_{\nu 0}}{h_\nu} - i\Omega_{KH} V_{\nu 0} \phi \frac{\partial k}{\partial \mu} \right),$$

$$C_2 = \frac{B_0 V_{\nu 0}}{h_\mu \Omega_{KH}} \frac{\partial \omega}{\partial \mu},$$

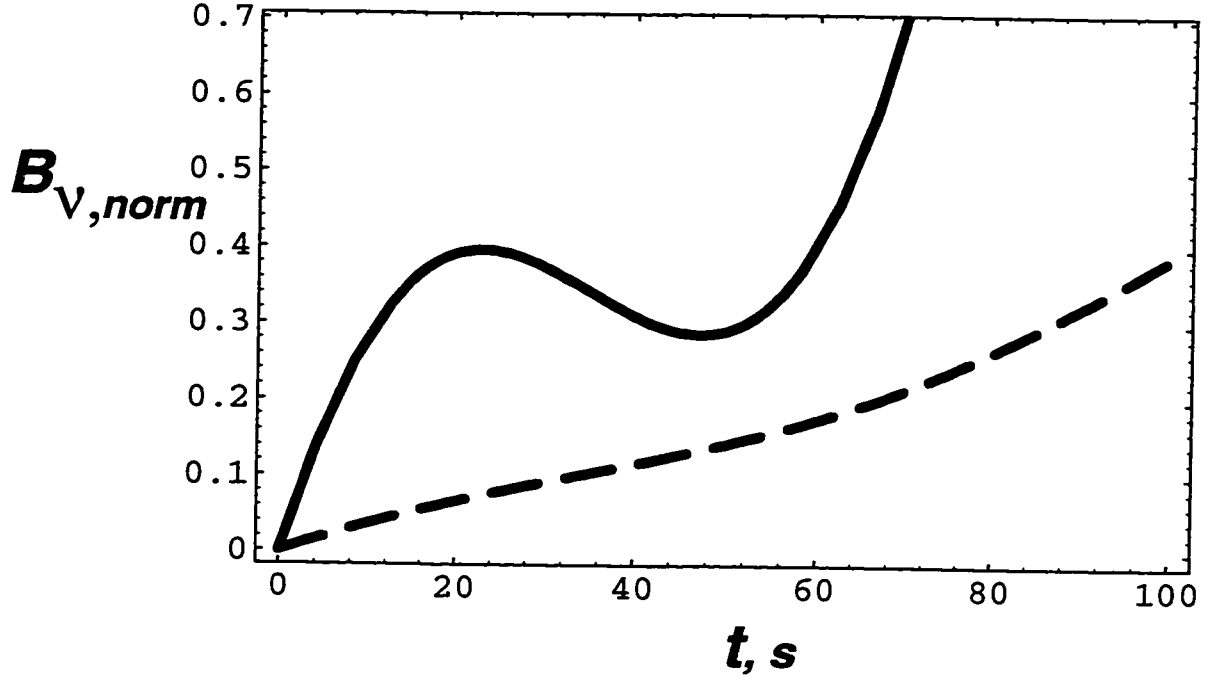


Figure 5.9: Temporal evolution of the  $B_{\nu, norm}$  perturbation amplitude as predicted by equation (5.9) for  $C_1/C_2 = 30$  (solid line) and 10 (dashed line).

$$C_3 = \frac{iB_0}{h_\nu \omega^2} \left( \frac{V_{\phi 0}}{h_\phi^2 \omega} \frac{\partial \omega}{\partial \mu} - \frac{\partial}{\partial \mu} \frac{V_{\phi 0}}{h_\phi} \right),$$

$$C_4 = \frac{B_0 V_{\phi 0}}{h_\mu \omega} \frac{\partial \omega}{\partial \mu}.$$

Equations (5.9)-(5.10) show that the magnetic field perturbations  $B_\nu$  and  $B_\phi$  grow linearly for  $t < \gamma^{-1}$ , and exponentially for  $t > \gamma^{-1}$ . Also, their growth is modulated with frequencies  $\Omega_{KH}$  and  $\omega$ , respectively. Note, that in our case  $\Omega_{KH} \sim \omega$  at the ionosphere and  $\omega \gg \gamma$  everywhere.

The growth of the amplitude of  $B_\nu$  is presented in Figure 5.9 as predicted by (5.9) for  $C_1/C_2 = 30$  (solid line) and  $C_1/C_2 = 10$  (dashed line). At the ionosphere,  $V_\nu$  is small because of the small growth rate and hence  $C_1$  is much greater than  $C_2$ . This provides well defined modulation with the period  $T = 2\pi\Omega_{KH}^{-1}$ , linear growth

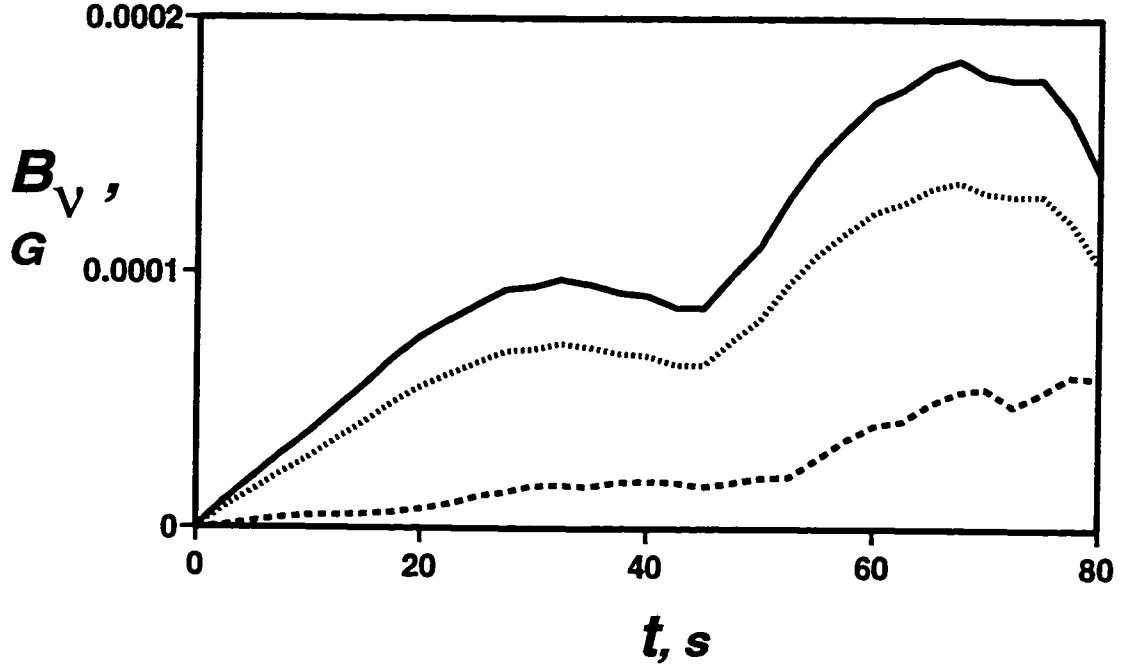


Figure 5.10: Growth of  $[B_\nu]_{MAX}$  at the ionosphere (solid line),  $0.5R_E$  (dashed line), and  $1R_E$  (dotted line) along the field line.

for  $t < \gamma^{-1}$ , and exponential growth for  $t > \gamma^{-1}$ . At higher altitudes where  $C_2$  is increased, the modulation becomes less noticeable. The similar evolution of the  $B_\nu$  component was obtained using the ADI code as presented in Figure 5.10.

The spatial distribution of field-aligned currents is shown in Figure 5.11 for the linear ( $t = 10$  and  $30$  s) and nonlinear ( $t = 70$  s) stages of the instability. As seen from the figure, initially field-aligned currents form into a fold-like structure which dissipates later in the nonlinear stage.

Further nonlinear evolution of the KH instability is in fact a gradual transformation of the KH mode into the fundamental SAW harmonic. Figure 5.12 shows the field aligned distribution of the  $B_\phi$  component obtained from 3D simulations

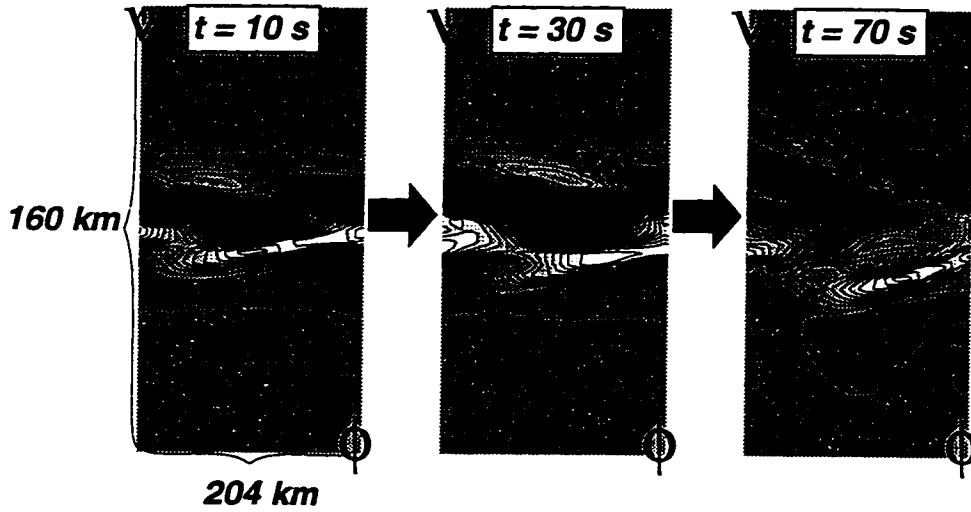


Figure 5.11: Time slices of the field-aligned current distribution at the ionosphere illustrating the formation and dissipation of the fold-like structure.

of the nonlinear KH mode and the fundamental harmonic SAW eigenfunction computed using (3.13). The comparison of these two functions confirms that the main SAW harmonic is the major mode which develops in the system during the nonlinear stage.

The transition from the KH mode to the SAW mode leads to the broadening and dissipation of the shear flow. Figure 5.13 shows time evolution of the radial distribution of the value  $\int_0^{2\pi} V_\phi d\phi$  which characterizes an average mass transport by the flow. This result is similar to the result found by *Rankin et al.* [1997] using the box model. The broadening and dissipation of the flow is principally a 3D KH effect. In the 2D case, the flow periodically widens and narrows with a period equal to the KH instability growth time.

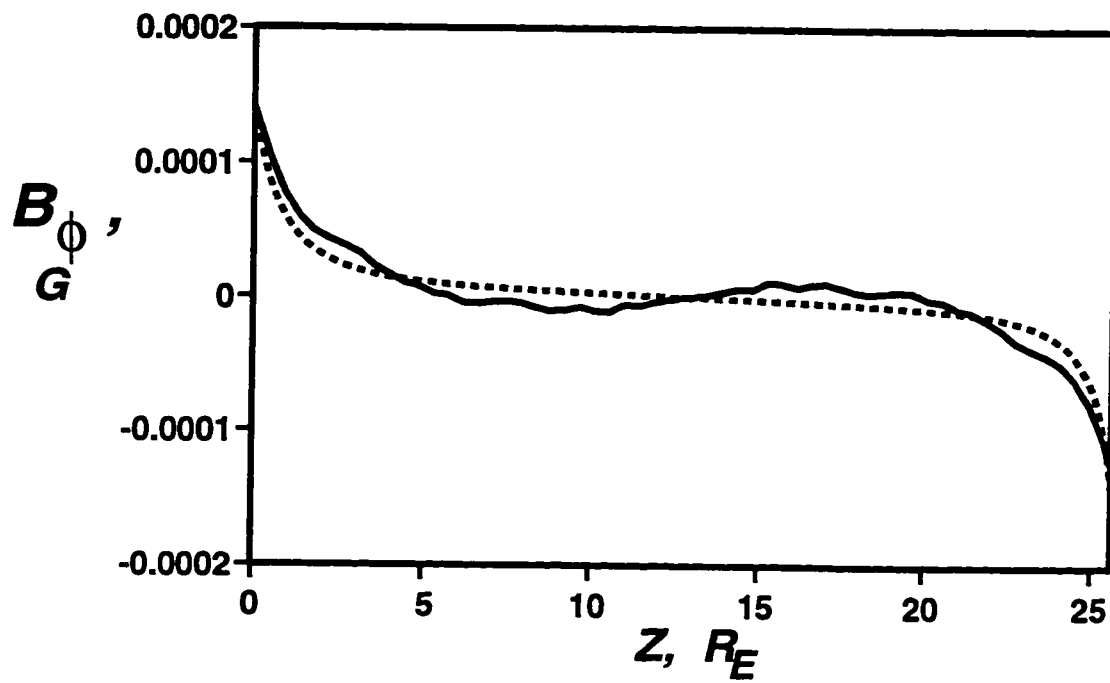


Figure 5.12: Field-aligned distribution of the  $B_\phi$  amplitude at  $t=70$  sec (solid line) and the  $B_\phi$  eigenfunction of the main SAW harmonic (dashed line).

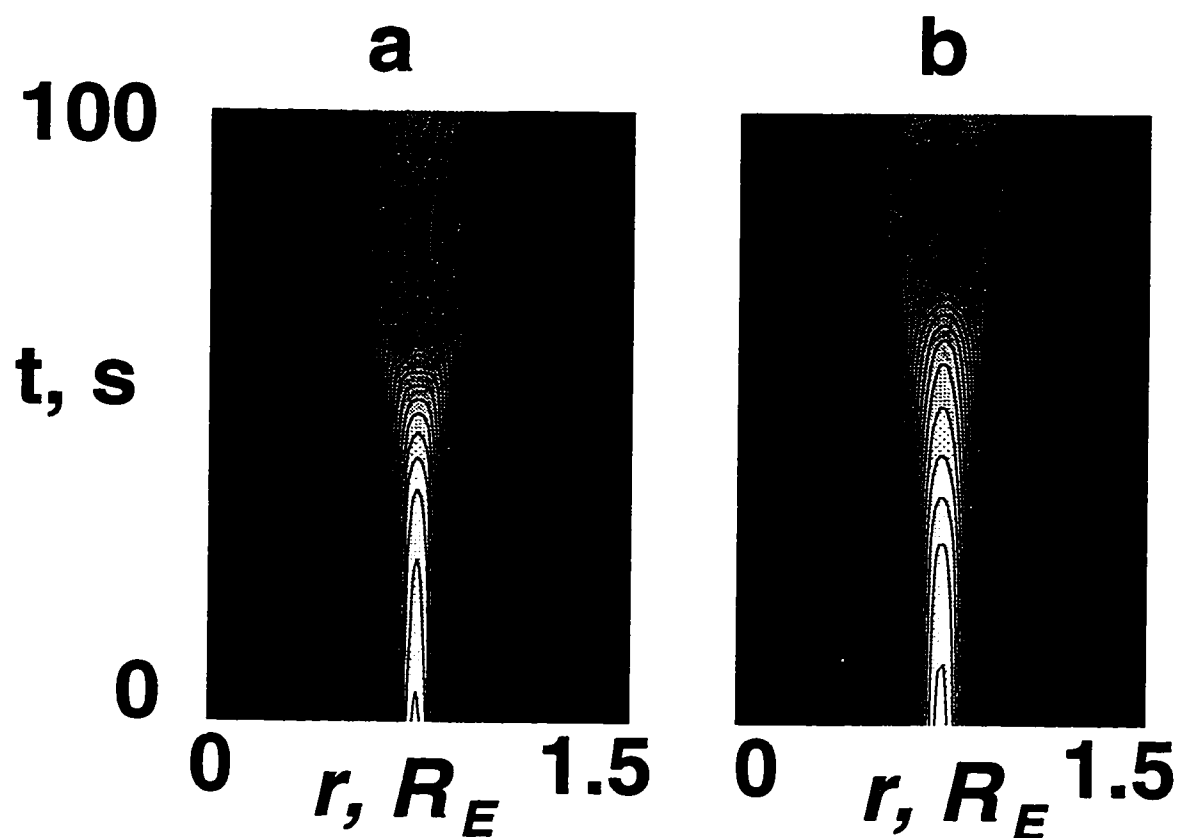


Figure 5.13: Temporal evolution of the shear flow in the equatorial plane as obtained from (a) 2D and (b) 3D models.



## 5.3 3D Ballooning Instability in the Plasma Sheet

### 5.3.1 The Ballooning Equilibrium Problem

The equilibrium of the plasma pressure and magnetic forces in the magnetosphere was originally studied by *Kan* [1973]. In this work, *Kan* [1973] assumed that the plasma was isothermal everywhere in the magnetotail, and that the density was uniform along the magnetic field lines. These assumptions allowed *Kan* [1973] to obtain an infinite set of partial solutions to the Grad-Shafranov equation [*Freidberg*, 1982] which describes the magnetospheric equilibrium. Further interest in this problem has raised recently after *Miura et al.* [1989] suggested that *Kan*'s model could be unstable with respect to the fundamental harmonic of the Alfvén ballooning mode. This result was argued by *Lee and Wolf* [1992], *Ohtani and Tamao* [1993], and *Chan et al.* [1994] who showed that in this global model, symmetric Alfvén modes are stable with respect to the ballooning. On the other hand, *Chan et al.* [1994] discovered that anisotropic pressure provides more opportunities for the ballooning instability to be operative. Furthermore, the solution to the isotropic Grad-Shafranov equation requires the assumption of uniform pressure distribution along the field lines [*Freidberg*, 1982; *Chan et al.*, 1994] which is unlikely to be applicable to active auroral processes.

In this study, we consider the ballooning instability in the central plasma sheet and assume that plasma pressure is anisotropic with respect to the dipolar coordinates  $\mu$  and  $\nu$ . In this case, we are free to choose an arbitrary magnetic field distribution providing  $\nabla \cdot \mathbf{B} = 0$ . Then we can find the equilibrium pressure distribution from the momentum equations for  $V_\nu = V_\mu = 0$  and  $\partial V_\nu / \partial t = \partial V_\mu / \partial t = 0$ . We have assumed that the enhanced pressure is localized around the equatorial

plane and that it diminishes outwards along the field lines.

Figure 5.14 shows the equilibrium distribution of  $P_{[\nu,\phi]}$  and  $B_\mu$  in the equatorial plane and field-aligned (plane  $[\nu,\mu]$ ) distribution of  $P_{[\nu,\phi]}$  and  $B_\nu$  which we used in the simulations described below. This distribution models the pre-substorm ion pressure distribution observed by *Kistler et al.* [1992] in the equatorial plane. These observations show a strong Earthward pressure gradient at  $7-9R_E$  with minimum  $\sim 0.2$  nPa at  $9R_E$ . Then the ion pressure grows tailward reaching  $\sim 1$  nPa at  $11-12R_E$ . Estimates made using (4.4) and (4.9) for the plasma pressure distribution found by *Kistler et al.* [1992] revealed that the region at  $8-10R_E$  is unstable with respect to ballooning. Therefore, we shall consider the evolution of the ballooning instability which develops from the equilibrium which is consistent with the pre-substorm pressure distribution observed by *Kistler et al.* [1992].

### 5.3.2 Ballooning Instability

In order to model the evolution of the ballooning instability in the equatorial region of the plasmasheet, we set boundaries at  $6R_E$  above the ionosphere and at  $L = 8.5$  and  $L = 11.5$  in the  $\nu$  direction. Plasma parameters were chosen as discussed in section 5.3.1 and demonstrated in Figure 5.14.

Growth of the initial perturbation  $V_\nu$  is shown in Figure 5.15 for different positions along the field line. As seen from this figure, the instability develops faster at the equatorial plane and then gradually propagates out along the field lines. It is interesting to note that eventually, the ballooning mode starts growing at the positions very close to boundaries even though these regions were initially stable with respect to ballooning.

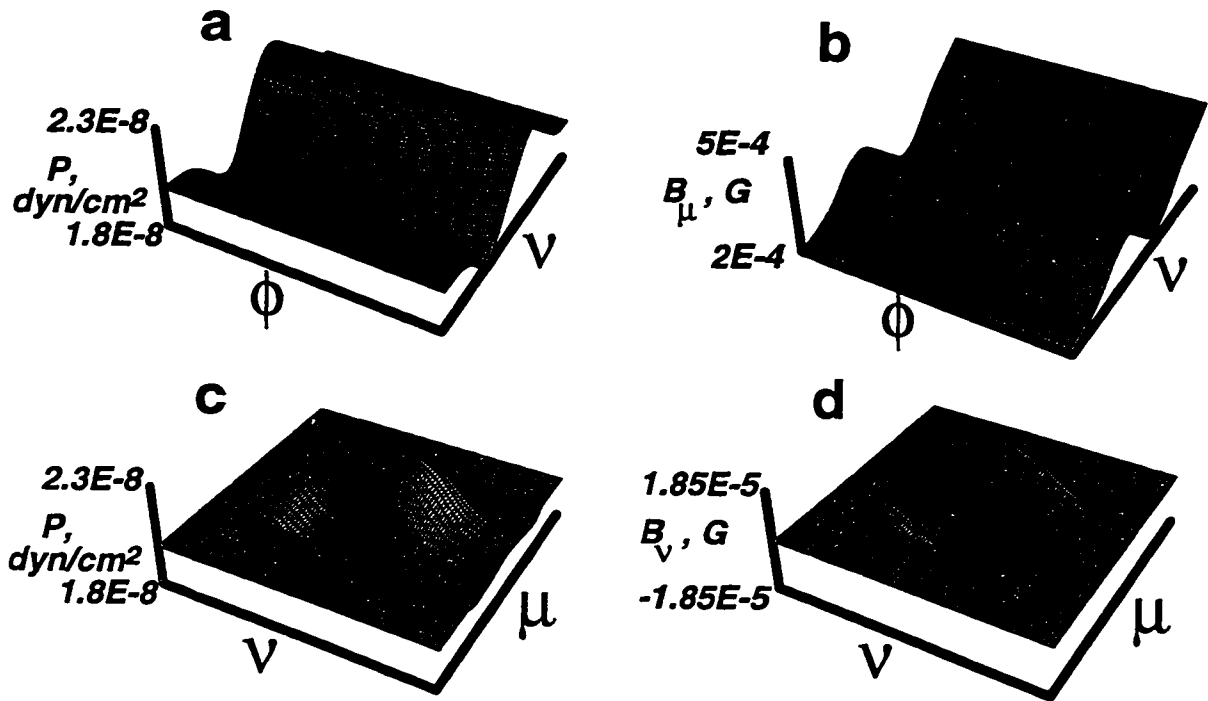


Figure 5.14: Initial equilibrium conditions for the 3D simulations of the ballooning instability: (a)  $P_{[\nu,\phi]}$  and (b)  $B_\mu$  in the equatorial plane, and (c)  $P_{[\nu,\phi]}$  and (d)  $B_\nu$  in the  $\mu, \nu$  plane. Field-aligned coordinate  $\mu$  starts at  $5R_E$  above the southern hemisphere and ends at  $5R_E$  above the northern hemisphere. Coordinate  $\nu$  covers the fraction from  $L = 8.5$  till  $L = 11.5$ .  $\phi$  is azimuthal corresponding to 2432 km in the equatorial plane.

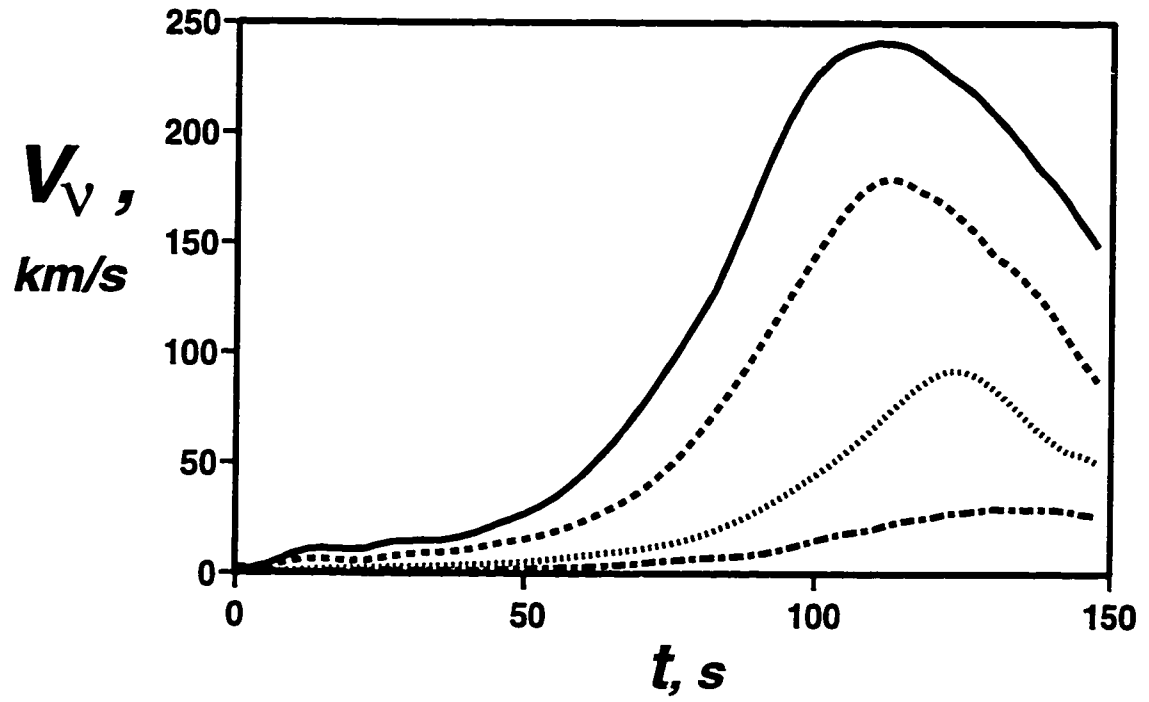


Figure 5.15: Growth of the initial perturbation  $V_v$  at  $7.8R_E$  (solid line),  $5.4R_E$  (dashed line),  $2.8R_E$  (dotted line), and  $0.7R_E$  (dash-dotted line) from the boundary along field lines.  $7.8R_E$  corresponds to the equatorial plane.

In the equatorial plane, the dynamics of the instability are very close to those predicted by the 2D theory (Chapter 4). Figure 5.16 presents time slices of the radial component of velocity  $V_r$ , the pressure, and the transient magnetic field  $B_\mu$  in the equatorial plane for three phases of the instability evolution: the initial distribution ( $t = 0$  s), linear growth of the ballooning cell ( $t = 75$  s), and nonlinear saturation at the boundaries of the ballooning unstable region ( $t = 100$  s). Figure 5.17 shows the energy changes in the system. As seen from this figure, the kinetic energy grows due to the work done by the magnetic curvature force as in the results of the 2D simulations described in chapter 4. During the nonlinear stage, this results in significant changes of the magnetic field topology in the unstable region. This process is illustrated by Figure 5.18. For this figure, the equatorial magnetic field  $B_\mu$  was averaged in the azimuthal direction and is shown as a function of the radial direction for  $t = 0$  s and  $t = 130$  s. The dipolar magnetic field profile is also shown in this figure.

The nonuniform field-aligned distribution of the ballooning vortices results in the excitation of SAWs similar to those excited by the KH instability. If ballooning cells do not propagate in the azimuthal direction, the SAWs which are excited in the system are mainly defined by the velocity amplitude variations along the field line. The resulting perturbations in the magnetic field  $B_r$  and  $B_\phi$  components is shown in Figure 5.19. These waves have large amplitudes and may affect the further evolution of the system. However, this process involves multi-scale interactions of SAWs and ballooning cells and would require more sophisticated simulations using faster computer techniques. It would be interesting to address this problem in further work.

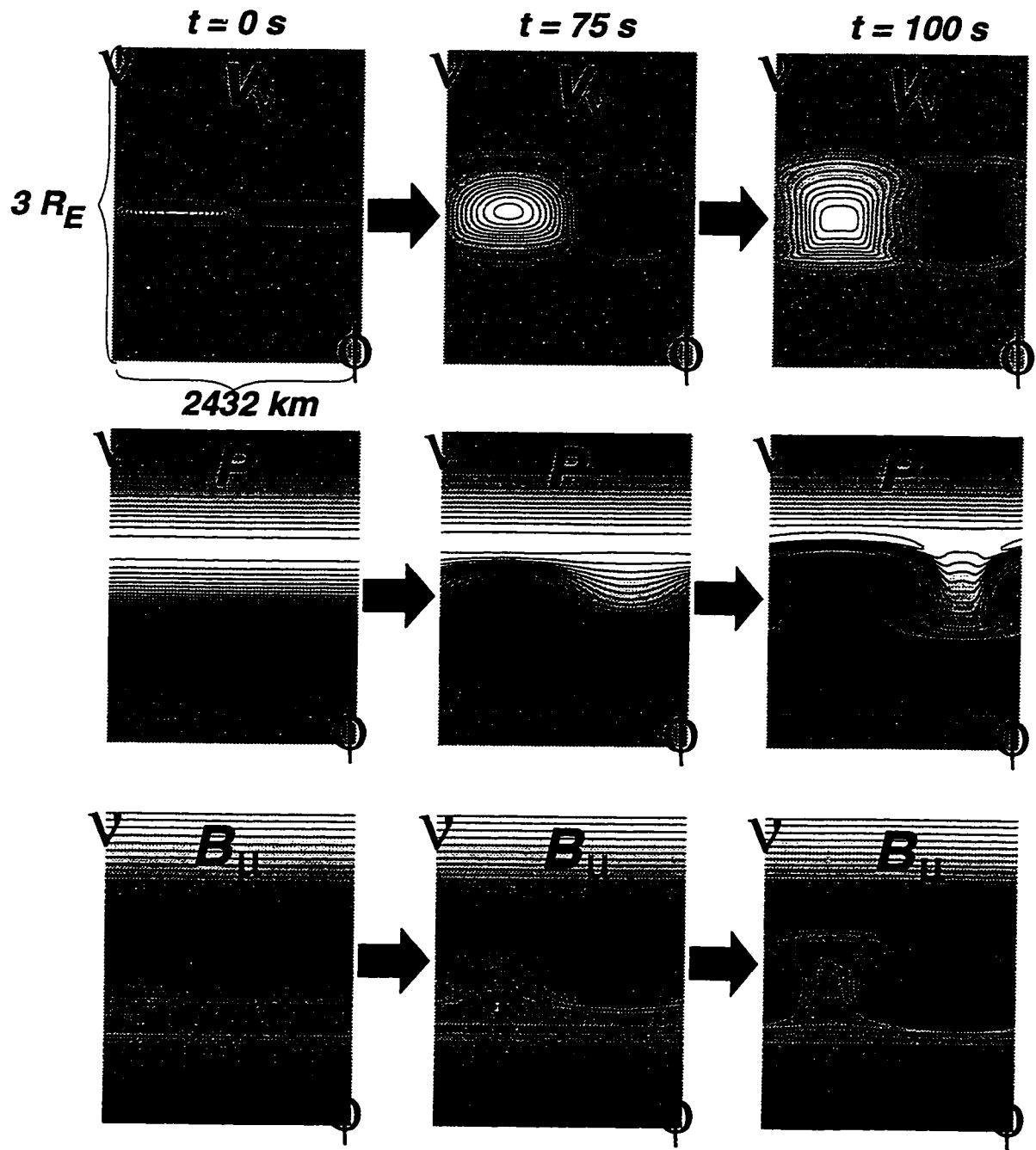


Figure 5.16: Evolution of the ballooning cell in the equatorial plane. Time slices correspond to the initial time ( $t = 0 \text{ s}$ ), linear stage ( $t = 75 \text{ s}$ ), and nonlinear stage ( $t = 100 \text{ s}$ ).

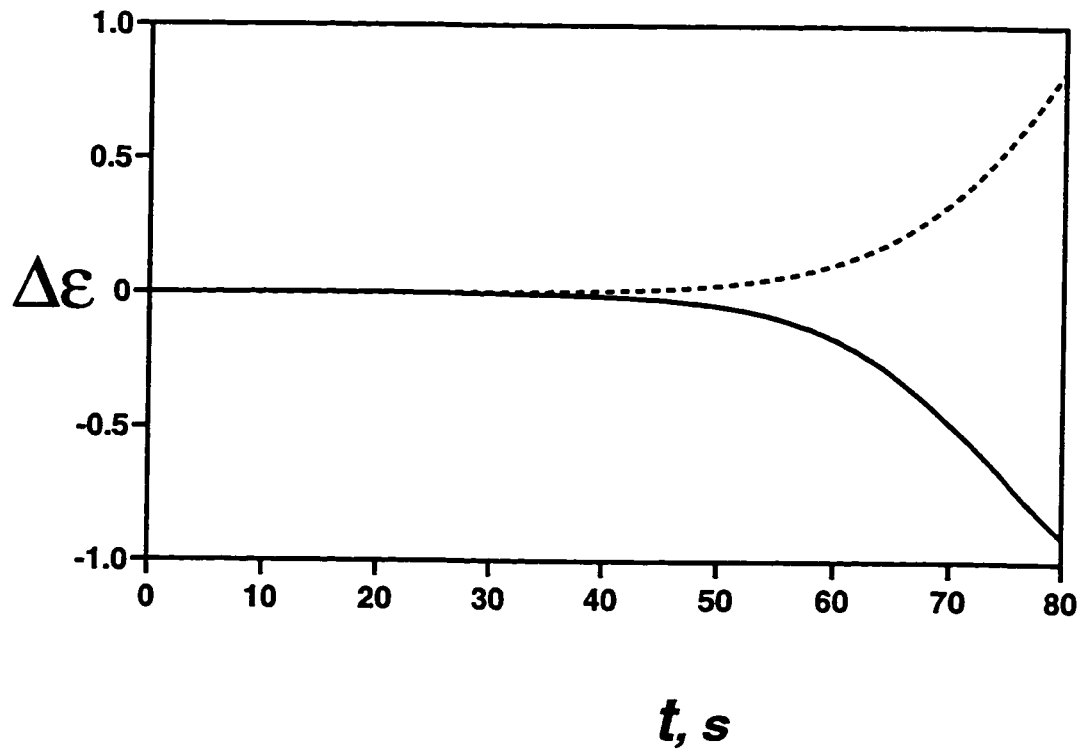


Figure 5.17: Changes of the kinetic energy (dashed line) and the work produced by the magnetic field line curvature force (solid line) in the equatorial region.

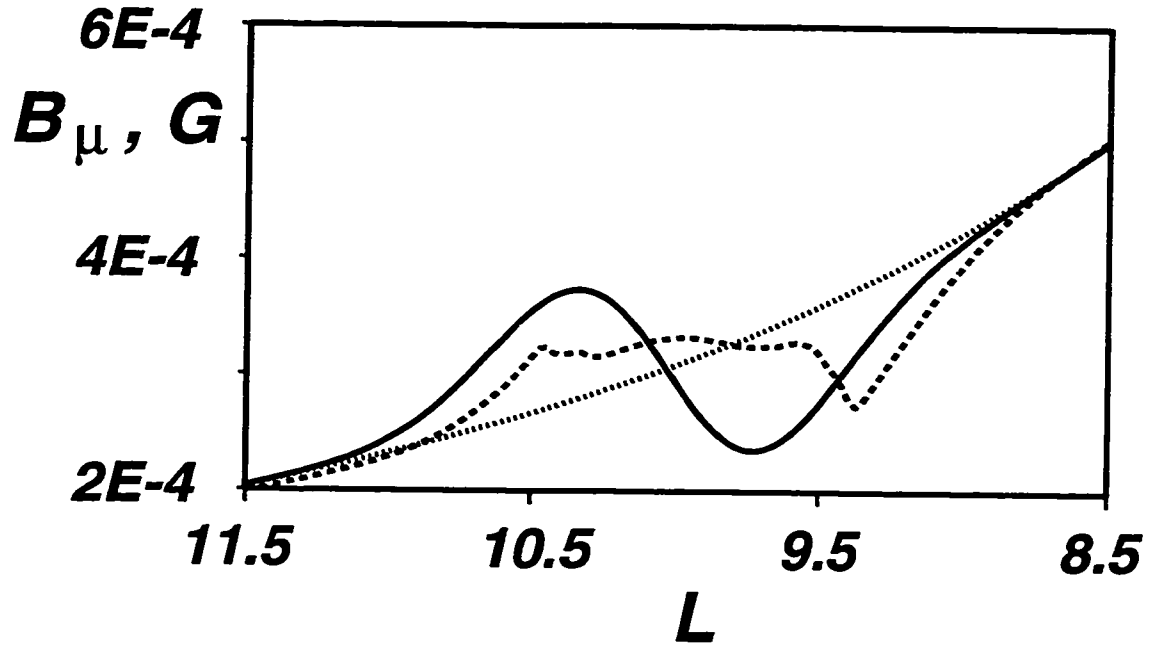


Figure 5.18: Equatorial  $B_\mu$  averaged over the azimuthal wavelength as a function of the radial distance at  $t = 0$  s (solid line) and  $t = 130$  s (dashed line), and dipolar magnetic field (dotted line).

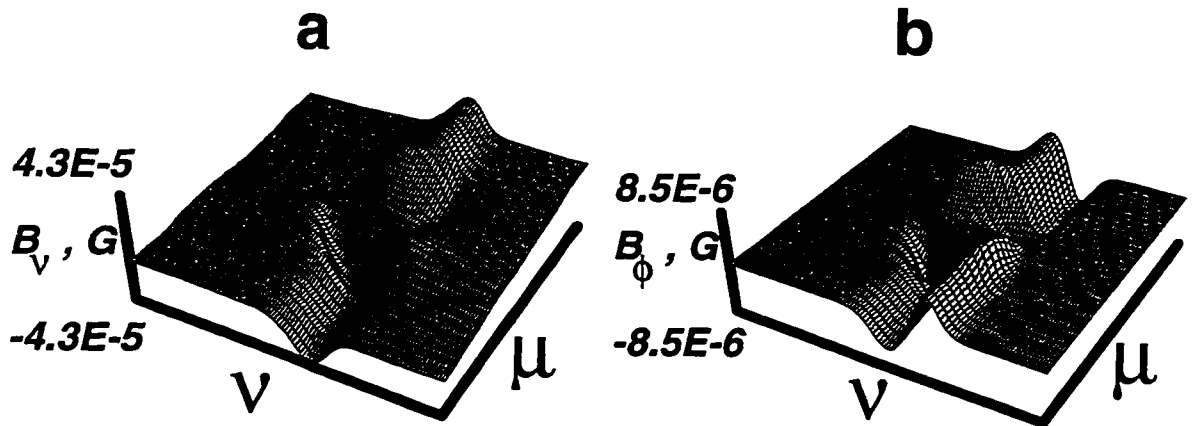


Figure 5.19: Field-aligned distribution of the amplitudes of the magnetic components (a)  $B_\nu$  and (b)  $B_\phi$  at  $t = 100$  s.



## 5.4 Summary

In this chapter, we have presented a complete three dimensional nonlinear model of the shear flow and ballooning instabilities which may occur in the plasma sheet and cause auroral disturbances. This model was constructed using a dipolar coordinate system. The model takes into account the curvilinear magnetic field in the magnetosphere and allows for dispersion along field lines and across magnetic  $L$ -shells. The results of modeling can be summarized as follows.

In the linear stage, the 3D KH instability evolves in a similar fashion to the 2D KH instability. Quantitatively, the 3D KH instability has lower ( $\sim 20\%$ ) growth rate and a lower frequency at the equator than the 2D instability. This difference occurs because of the weak field-aligned coupling (or energy exchange) which exists between vortices at different points along the field line. We have developed an analytical model which allowed us to describe this coupling in terms of the field-aligned currents excited by the instability.

We have shown that the KH mode velocity distribution has approximately the same structure at different levels along the field line. However, these modes have different azimuthal phase velocities at different altitudes. This results in a field-aligned phase shift between vortices and can initiate the oscillations of oblique Alfvén waves during the linear stage of the instability. Also, due to the phase shift between vortices at different altitudes, the spatial distribution of convection patterns in the ionosphere and of the vortical structures at  $\sim 2 - 3R_E$  above the ionosphere, i.e. in the region where the auroral electron acceleration most probably occurs, can be out of phase. This spatial shift can be proposed as a candidate mechanism which might explain the displacement and opposite rotation of the ionospheric convection and luminosity patterns.

We have derived a linear expression for the amplitudes of the magnetic perturbation due to the KH instability. This expression predicts that the magnetic perturbations, which are responsible for the field-aligned current formation above the ionosphere, grow and are modulated with the frequency  $\Omega_{KH}$ . This linear theory prediction occurs in agreement with the numerical solution of the nonlinear MHD equations.

As follows from the simulations, nonlinear evolution of the 3D and 2D KH instabilities differ. Analysis of the nonlinear stage of the 3D KH instability has shown that this stage is, in fact, the gradual transition of the KH mode into the main SAW harmonic. This process is accompanied by a broadening of the shear flow and a dissipation of the KH vortices.

In order to study the evolution of the ballooning mode, we have imposed the pressure gradient and the curvilinear topology of the magnetic field lines in the equatorial region. This study has confirmed the prediction of the 2D analytical model that the ballooning mode is unstable in a system with an Earthward pressure gradient. The total kinetic energy in the system grows due to the work done by the magnetic field line curvature force. This instability may produce localized regions of magnetic field lines which are even more stretched, than they were initially. Simulations showed that in the linear stage, the ballooning instability initiates symmetric ballooning cells which expand radially. The nonlinear saturation occurs when these cells reach the boundaries of the unstable region. In the nonlinear stage, the ballooning mode initiates large amplitude SAWs. However, the further interaction of the ballooning modes and SAWs, as well as the coupling of the shear flow and ballooning instabilities involves spatial and temporal multi-scale mode interaction which can be resolved using more advanced computer techniques. This problem can be proposed as a further application of the three-dimensional computer model

described above.

## CHAPTER 6

### Conclusions

In this work, we have developed the code which solves the system of ideal nonlinear MHD equations in curvilinear coordinates. The code can be easily adapted to run on different kinds of new parallel and vector computers. A new fast technique was developed, tested, and effectively implemented on the Stardent and SGI computers.

We used this code to develop models and a suitable theory of nonlinear FLRs and SAWs in the dipolar magnetosphere. The models and theory are an advance from the previous box model [*Rankin et al.*, 1993b; 1994; 1995] giving a more realistic description of nonlinear SAWs and FLRs. We have taken into account the dipolar geometry of resonant magnetic shells and the nonuniform distribution of plasma density along geomagnetic field lines. The analytical theory and numerical simulations have confirmed the main results obtained using the box model. We have shown that the SAW can linearly grow in resonance regions and initiate the nonlinear ponderomotive force. This ponderomotive force leads to plasma density redistribution and nonlinear saturation of the FLR due to frequency detuning of the resonant magnetic shell. Compared to the box model, this ponderomotive force consists of three parts: magnetic pressure, magnetic curvature, and particle inertia. We have shown that the density redistribution can be described using an equation for driven slow magnetosonic waves (SMWs). Due to the geometry and density inhomogeneity, in the dipolar case the coupling between the SAW and the nonlinear

density perturbations results in the excitation of a wide spectrum of SMWs which gradually form a narrow peak in the vicinity of the second harmonic SMW. As in the box model, the second harmonic SMW is responsible for the SAW detuning which results in FLR saturation. However, the smaller SMW modes (which are not excited in the box model) may still reach significant amplitudes and might play an important role in particle heating at altitudes of 1-2  $R_E$  above the ionosphere. This heating, in conjunction with such mechanisms as two-fluid ponderomotive force acceleration [Li and Temerin, 1993], may play an important role in auroral magnetosphere-ionosphere interactions.

Another result predicted by the dipolar FLR theory is that higher temperatures in the equatorial magnetosphere increase the time scale for ponderomotive FLR saturation, in which case the FLR SAW can grow to large amplitude. This result appears to be in agreement with the observed latitudinal distribution of Pc5 pulsations which has a maximum in the region corresponding to the hot plasmas of the ring current belts [Walker and Greenwald, 1981; Tian et al., 1991; Potemra and Blomberg, 1996] and in the evening sector of the inner plasma sheet [Samson et al., 1996a].

Because of the nonuniform radial distribution of SAW frequencies, the phase velocity of SAWs is directed anti-Earthward. The corresponding temporal dynamics of the field-aligned currents at the footprints of the magnetic field lines is in close agreement with results of photometer observations which show poleward motion of discrete auroral arcs.

Neglecting plasma wave dispersion across magnetic  $L$  shells, which can occur due to electron inertia [Streltsov and Lotko, 1996; 1997], we have found that the FLR should evolve into a narrow channel near the resonant shell. This structuring

can eventually lead to the excitation of Kelvin-Helmholtz shear flow instabilities with characteristic  $e$ -folding time smaller than the SAW half period.

Two-dimensional theory and numerical simulations of the evolution of a shear flow embedded in a pressure gradient region in the equatorial plane have revealed a constructive interaction between the unstable shear flow mode (KH mode) and the ballooning mode. In the linear stage of the instability, the KH vortex interacts with the main ballooning harmonic, which enhances the growth rate of the hybrid mode. When the KH-like vortex saturates, it experiences a short transition stage when the vortex evolution changes from KH-like to ballooning-like. At the end of the transition stage, the hybrid vortex becomes a large amplitude perturbation for the ballooning instability and experiences further growth.

In the nonlinear stage, the hybrid vortex defines the radial size of the interacting ballooning cell. This stage is characterized by an extraction of potential energy from the pressure gradient and its transformation into kinetic energy of the hybrid vortex. During this nonlinear stage, the vortex evolution depends on the azimuthal wave number as well as on the shape of the flow. A uni-directional flow generates vortices which move with respect to the ambient plasma, providing a constructive interaction of vortices and ballooning cells which move with the flow. The optimal wavenumber for this interaction corresponds to  $k \sim 1/\delta$ , where  $\delta$  is a half width of the shear flow. The radial expansion of the vortex is restricted by the interaction of the vortex with the boundaries of the flow. This interaction saturates the hybrid vortex, but at the same time, it modifies the flow and generates large scale perturbations of the boundaries. This leads to a further interaction with a large scale ballooning cell and a further extraction of potential energy from the ballooning unstable region.

A different evolution was obtained for a bi-directional shear flow with an instability wavenumber  $k \sim 0.5/\delta$ . In this case, the hybrid vortex takes the form of a radially stretched fold which does not move in the azimuthal direction. In the nonlinear stage, this vortex interacts with a large-scale ballooning cell, and leads to the fast growth and radial expansion of the vortex.

The model of the shear flow instabilities was further developed into a three-dimensional model which allowed us to study the field-aligned propagation of perturbations. This model has confirmed the main results obtained using the 2D theory and simulations. In the case of the unstable shear flow, we have found that the linear vortex evolution at every altitude along the field lines is similar to that predicted by the 2D theory. However, field-aligned variations of the phase velocity cause a different spatial shift of the vortices at different altitudes. This shift leads to the propagation of oblique Alfvén waves and modifies the field-aligned current dynamics. We proposed that this field-aligned dispersion could be a mechanism which generate a spatial phase displacement between convection and luminosity patterns at the ionospheric level. The further nonlinear evolution of the KH instability is a gradual transition of the KH mode into the fundamental SAW harmonic. This process leads to the broadening and dissipation of the initial shear flow and vortices.

The existence of a radial pressure gradient on the stretched magnetic field lines in the equatorial plasma sheet can lead to a ballooning instability. The scenario of this instability predicted by the 2D model was further developed using 3D simulations. We have shown that the ballooning instability initiates ballooning cells. The kinetic energy accumulated in these cells grows due to the work done by the stretched magnetic field lines. The ballooning cells expand radially with a characteristic time of tens of seconds for the chosen instability parameters. Saturation occurs when these cells reach boundaries of the unstable region. In the nonlinear

stage, the ballooning instability initiates large amplitude SAWs. This suggests that the ballooning mode can constructively interact with SAWs. However, features of this coupling as well as of the interaction of the ballooning and shear flow modes requires more sophisticated study using faster computer techniques. We would like to address this problem in a further study

Summarizing these results, we conclude that interaction between such MHD waves as SAWs, shear flow modes, and ballooning modes which has been considered in this work appears to be a valid candidate mechanism for generating auroral vortices. This processes may lead to the formation of large amplitude folds and curls which are repeatedly observed in association with active auroral arcs.



## Bibliography

- Akasofu, S.-I., *Physics of Magnetospheric Substorms*, 599 p., D. Reidel Publ. Co., Dordrecht, 1977.
- Alfvén, H., and C.-G. Fälthammar, *Cosmical Electrodynamics; Fundamental Principles*, 228 p., Clarendon Press, Oxford, 1963.
- Allan, W., and F. B. Knox, A dipole field model for axisymmetric Alfvén waves with finite ionosphere conductivities, *Planet. Space Sci.*, *27*, 79, 1979.
- Allan, W., J. R. Manuel, and E. M. Poulter, Magnetospheric cavity modes: Some nonlinear effects, *J. Geophys. Res.*, *96*, 11461, 1991.
- Allan, W., Ponderomotive mass transport in the magnetosphere, *J. Geophys. Res.*, *97*, 8483, 1992.
- Allan, W., The ponderomotive force of standing Alfvén waves in a dipolar magnetosphere, *J. Geophys. Res.*, *98*, 1409, 1993a.
- Allan, W., Plasma energization by the ponderomotive force of magnetospheric standing Alfvén waves, *J. Geophys. Res.*, *98*, 11383, 1993b.
- Arnoldy, R. L., Auroral particle precipitation and Birkeland currents, *Rev. Geophys. Space Phys.*, *12*, 217, 1974.
- Atkinson, G., An approximate flow equation for geomagnetic flux tubes and its application to polar substorms, *J. Geophys. Res.*, *72*, 5373, 1967.
- Atkinson, G., F. Creutzberg, R. L. Gattinger, and J. S. Murphree, Interpretation of complicated discrete arc structure and behavior in terms of multiple X lines, *J. Geophys. Res.*, *94*, 5292, 1989.

- Axford, W. I., and C. O. Hines, A unifying theory of high-latitude geophysical phenomena and geomagnetic storms, *Can. J. Phys.*, *39*, 1433, 1961.
- Baker, D. N., and R. L. McPherron, Extreme energetic particle decreases near geostationary orbit: A manifestation of current diversion within the inner plasma sheet, *J. Geophys. Res.*, *95*, 6591, 1990.
- Baker, D. N., T. I. Pulkkinen, R. L. McPherron, J. D. Craven, L. A. Frank, R. D. Elphinstone, J. S. Murphree, J. F. Fennell, R. E. Lopez, and T. Nagai, CDAW 9 analysis of magnetospheric event on May 3, 1986: Event C, *J. Geophys. Res.*, *98*, 3815, 1993.
- Baumjohann, W., R. J. Pellinen, H. J. Opgenoorth, and E. Nielsen, Joint two-dimensional observations of ground magnetic and ionospheric electric fields associated with auroral zone currents: Current system associated with local auroral break-ups, *Planet. Space Sci.*, *29*, 431, 1981.
- Birkeland, K., Sur les rayons cathodiques sous l'action des forces magnetiques intenses, *Arch. Sci. Phys.*, *1*, 497, 1896.
- Borovsky, J. E., Auroral arc thicknesses as predicted by various theories, *J. Geophys. Res.*, *98*, 6101, 1993.
- Brandt, J. C., *Introduction to the Solar Wind*, 199 p., Freeman, San Francisco, 1970.
- Bruning, K., and C. K. Goertz, Dynamics of a discrete auroral arc, *J. Geophys. Res.*, *91*, 7057, 1986.
- Buchner, J., and L. M. Zelenyi, Chaotization of the electron motion as the cause of an internal magnetotail instability and substorm onset, *J. Geophys. Res.*, *92*, 13456, 1987.

- Carlson, C. W., and M. C. Kelley, Observation and interpretation of particle and electric field measurements inside and adjacent to an active auroral arc, *J. Geophys. Res.*, **82**, 2349, 1977.
- Chan, A. A., M. Xia, and L. Chen, Anisotropic Alfvén-ballooning modes in Earth's magnetosphere, *J. Geophys. Res.*, **99**, 17351, 1994.
- Chapman, S., and V. C. A. Ferraro, A new theory of magnetic storms, *Terr. Mag. Atmosph. Elec.*, **36**, 77, 1931.
- Chen, F. F., *Introduction to Plasma Physics and Controlled Fusion*, vol. 1, *Plasma Physics*, Plenum Press, New York, 1984.
- Chen, L., and A. Hasegawa, A theory of long-period magnetic pulsations 1. Steady state excitation of field line resonance, *J. Geophys. Res.*, **79**, 1024, 1974.
- Davis, T. N., and T. J. Hallinan, Auroral spirals 1. Observations, *J. Geophys. Res.*, **81**, 3953, 1976.
- Davis, T. N., Observed characteristics of auroral forms, *Space. Sci. Rev.*, **22**, 77, 1978.
- Douglas, J. J., and J. E. Gunn, A general formulation of alternating direction methods. Part 1. Parabolic and hyperbolic problems, *Numer. Math.*, **6**, 428, 1964.
- Drake, J. F., J. M. Finn, P. Guzdar, V. Shapiro, V. Shevchenko, F. Waelbroeck, A. B. Hassam, C. S. Liu, and R. Sagdeev, Peeling of convection cells and the generation of sheared flow, *Phys. Fluids B*, **4**, 488, 1992.
- Dungey, J. W., Interplanetary magnetic field and the auroral zones, *Phys. Rev. Lett.*, **6**, 47, 1961.

- Eastman, T. E., B. Popielawska, and L. A. Frank, Three-dimensional plasma observations near the outer magnetospheric boundary, *J. Geophys. Res.*, *90*, 9519, 1985.
- Elphinstone, R. D., D. J. Hearn, L. L. Cogger, J. S. Murphree, H. Singer, V. Sergeev, K. Mursula, D. M. Klumpar, G. D. Reeves, M. Johnson, S. Ohtani, T. A. Potemra, I. Sandahl, E. Nielsen, M. Persson, H. Opgenoorth, P. T. Newell, and Y. I. Feldstein, Observations in the vicinity of substorm onset: Implications for the substorm process, *J. Geophys. Res.*, *100*, 7937, 1995.
- Elphinstone, R. D., J. S. Murphree, and L. L. Cogger, What is global auroral substorm?, *Rev. Geophys.*, *34*, 169, 1996.
- Evans, D. S., The observations of a near monoenergetic flux of auroral electrons, *J. Geophys. Res.*, *73*, 2315, 1968.
- Evans, D. S., Precipitating electron fluxes formed by a magnetic field aligned potential difference, *J. Geophys. Res.*, *79*, 2853, 1974.
- Evans, D. S., N. C. Maynard, J. Troim, T. Jacobsen, and A. Egeland, Auroral vector electric field and particle comparisons 2. Electrodynamics of an arc, *J. Geophys. Res.*, *82*, 2235, 1977.
- Fairfield, D. H., Average magnetic field configuration of the outer magnetosphere, *J. Geophys. Res.*, *73*, 7329, 1968.
- Fenrich, F. R., J. C. Samson, G. Sofko, and R. A. Greenwald, ULF high- and low-*m* field line resonances observed with the Super Dual Auroral Radar Network, *J. Geophys. Res.*, *100*, 21535, 1995.
- Fenrich, F. R., The field line resonance: observation and theory, Ph.D. Thesis, 118 p., University of Alberta, Edmonton, 1997.

- Finan, C. H., III, and J. Killeen, Solution of the time-dependent, three-dimensional resistive magnetohydrodynamic equations, *Comput. Phys. Commun.*, *24*, 441, 1981.
- Finn, J. M., J. F. Drake, and P. N. Guzdar, Instability of fluid vortices and generation of sheared flow, *Phys. Fluids B*, *4*, 2758, 1992.
- Finn, J. M., Nonlinear interaction of Rayleigh-Taylor and shear instabilities, *Phys. Fluids B*, *5*, 415, 1993.
- Foster, J. C., D. H. Fairfield, K. W. Ogilvie, and T. J. Rosenberg, Relationship of interplanetary parameters and occurrence of magnetospheric substorms, *J. Geophys. Res.*, *76*, 6971, 1971.
- Frank, L. A., and K. L. Ackerson, Observations of charged particle precipitation into the auroral zone, *J. Geophys. Res.*, *76*, 3612, 1971.
- Freidberg, J. P., Ideal magnetohydrodynamic theory of magnetic fusion systems, *Rev. Mod. Phys.*, *54*, 801, 1982.
- Frey, H. U., G. Haerendel, D. Knudsen, S. Buchert, and O. H. Bauer, Optical and radar measurements of the motion of auroral arcs, *J. Atmos. Terr. Phys.*, *58*, 57, 1996.
- Fritz, H., *Das Polarlicht*, 348 p., Leipzig, 1881.
- Galinsky, V. L., and B. U. Ö. Sonnerup, Dynamics of shear velocity layer with bent magnetic field lines, *Geophys. Res. Lett.*, *21*, 2247, 1994.
- Ganguli, G., Y. C. Lee, and P. J. Palmadesso, Kinetic theory for electrostatic waves due to transverse velocity shears, *Phys. Fluids*, *31*, 823, 1988.
- Goertz, C. K., and R. W. Boswell, Magnetosphere - ionosphere coupling, *J. Geophys. Res.*, *84*, 7239, 1979.

- Gringauz, K. I, Structure of the Earth's ionized gas environment according to the spacecraft measurements of local charged particle densities, *Earth's Satellites*, 12, 105, 1962 (in Russian).
- Guglielmi, A. V., Comment on the ponderomotive self-action of Alfvén waves, *J. Geophys. Res.*, 102, 209, 1997.
- Gurnett, D. A., and L. A. Frank, Observed relationships between electric fields and auroral particle precipitation, *J. Geophys. Res.*, 78, 145, 1973.
- Haerendel, G., S. Buchert, C. La Hoz, B. Raaf, and E. Rieger, On the proper motion of auroral arcs, *J. Geophys. Res.*, 98, 6087, 1993.
- Haerendel, G., B. U. Olipitz, S. Buchert, O. H. Bauer, E. Rieger, and C. La Hoz, Optical and radar observations of auroral arcs with emphasis on small-scale structures, *J. Atmos. Terr. Phys.*, 58, 71, 1996.
- Hallinan, T. J., and T. N. Davis, Small-scale auroral arc distortions, *Planet. Space Sci.*, 18, 1735, 1970.
- Hallinan, T. J., Auroral spirals 2. Theory, *J. Geophys. Res.*, 81, 3959, 1976.
- Hameiri, E., P. Laurence and M. Mond, The ballooning instability in space plasmas, *J. Geophys. Res.*, 96, 1513, 1991.
- Heppner, J. P., M. L. Miller, M. B. Pongratz, G. M. Smith, L. L. Smith, S. B. Mende, and N. R. Nath, The cameo barium releases:  $E_{\parallel}$  fields over the polar cap, *J. Geophys. Res.*, 86, 3519, 1981.
- Hesse, M., and J. Birn, MHD modeling of magnetotail instability for localized resistivity, *J. Geophys. Res.*, 99, 8565, 1994.
- Holter, O., C. Altman, A. Roux, S. Perraut, A. Pedersen, H. Pecseli, B. Lybekk, J.

- Trulsen, A. Korth, and G. Kremser, Characterization of low frequency oscillations at substorm breakup, *J. Geophys. Res.*, *100*, 19109, 1995.
- Hones, E. W., Jr., The poleward leap of the auroral electrojet as seen in auroral images, *J. Geophys. Res.*, *90*, 5333, 1985.
- Huba, J. D., Hall dynamics of the Kelvin-Helmholtz instability, *Phys. Rev. Lett.*, *72*, 2033, 1994.
- Huba, J. D., Finite Larmor radius magnetohydrodynamics of the Rayleigh-Taylor instability, *Phys. Plasmas*, *3*, 2523, 1996.
- Iijima, T., and T. A. Potemra, Large-scale characteristics of field-aligned currents associated with substorms, *J. Geophys. Res.*, *83*, 599, 1978.
- Jacquey, C., J. A. Sauvaud, and J. Dandouras, Location and propagation of the magnetotail current disruption during substorm expansion: Analysis and simulation of an ISEE multi-onset event, *Geophys. Res. Lett.*, *18*, 389, 1991.
- Jacquey, C., J. A. Sauvaud, J. Dandouras, and A. Korth, Tailward propagating cross-tail current disruption and dynamics of near-Earth tail: A multi-point measurement analysis, *Geophys. Res. Lett.*, *20*, 983, 1993.
- Kan, J. R., On the structure of the magnetotail current sheet, *J. Geophys. Res.*, *78*, 3773, 1973.
- Kan, J. R., and W. Sun, Simulations of the westward traveling surge and Pi 2 pulsations during substorms, *J. Geophys. Res.*, *90*, 10911, 1985.
- Kavanagh, L. D., Jr., J. W. Freeman, Jr., and A. J. Chen, Plasma flow in the magnetosphere, *J. Geophys. Res.*, *73*, 5511, 1968.
- Kelley, M. C., Intense sheared flow as the origin of large-scale undulations of the

- edge of the diffuse aurora, *J. Geophys. Res.*, *91*, 3225, 1986.
- Kennel, C. F., and H. E. Petschek, Limit on stably trapped particles fluxes, *J. Geophys. Res.*, *71*, 1, 1966.
- Kidd, S. R., and G. Rostoker, Distribution of auroral surges in the evening sector, *J. Geophys. Res.*, *96*, 5697, 1991.
- Kistler, L. M., E. Möbius, W. Baumjohann, G. Paschmann, and D. C. Hamilton, Pressure changes in the plasma sheet during substorm injections, *J. Geophys. Res.*, *97*, 2973, 1992.
- Kivelson, M. G., J. Etcheto, and J. B. Trotignon, Global compressional oscillations of the terrestrial magnetosphere: The evidence and a model, *J. Geophys. Res.*, *89*, 9851, 1984.
- Klimushkin, D. Y., A. S. Leonovich, and V. A. Mazur, On the propagation of transversally small-scale standing Alfvén waves in a three-dimensionally inhomogeneous magnetosphere, *J. Geophys. Res.*, *100*, 9527, 1995.
- Knudsen, D. J., Spatial modulation of electron energy and density by nonlinear stationary inertial Alfvén waves, *J. Geophys. Res.*, *101*, 10761, 1996.
- Kokubun, S., R. L. McPherron, and C. T. Russell, Triggering of substorms by solar wind discontinuities, *J. Geophys. Res.*, *82*, 74, 1977.
- Landau, L. D., and E. M. Lifshitz, *Electrodynamics of Continuous Media*, 460 p., Pergamon, Oxford, 1984.
- Lee, D.-Y., and R. A. Wolf, Is the Earth's magnetotail balloon unstable?, *J. Geophys. Res.*, *97*, 19251, 1992.
- Li, X., and M. Temerin, Ponderomotive effects on ion acceleration in the auroral



- zone, *Geophys. Res. Lett.*, **20**, 13, 1993.
- Lopez, R. E., and A. T. Y. Lui, A multisatellite case study of the expansion of a substorm current wedge in the near-Earth magnetotail, *J. Geophys. Res.*, **95**, 8009, 1990.
- Lui, A. T. Y., C.-I. Meng, and S. Ismail, Large amplitude undulation on the equatorward boundary of the diffuse aurora, *J. Geophys. Res.*, **87**, 2385, 1982.
- Lui, A. T. Y., R. E. Lopez, S. M. Krimigis, R. W. McEntire, L. J. Zanetti, and T. A. Potemra, A case study of magnetotail current disruption and diversion, *Geophys. Res. Lett.*, **15**, 721, 1988.
- Lui, A. T. Y., A synthesis of magnetospheric substorm models, *J. Geophys. Res.*, **96**, 1849, 1991.
- Lui, A. T. Y., C.-L. Chang, A. Mankofsky, H.-K. Wong and D. Winske, A cross-field current instability for substorm expansion, *J. Geophys. Res.*, **96**, 11389, 1991.
- Lui, A. T. Y., R. E. Lopez, B. J. Anderson, K. Takahashi, L. J. Zanetti, R. W. McEntire, T. A. Potemra, D. M. Klumpar, E. M. Greene, and R. Strangeway, Current disruptions in the near-Earth neutral sheet region, *J. Geophys. Res.*, **97**, 1461, 1992.
- Lyatsky, W., Northward solar wind magnetic field as a substorm trigger. in *Proceedings of the third international conference on substorms (ICS-3)*, 341, ESA SP-389, Versailles, 1996.
- Lyons, L. R., D. S. Evans, and R. Lundin, An observed relation between magnetic field aligned electric fields and downward electron energy fluxes in the vicinity of auroral forms, *J. Geophys. Res.*, **84**, 457, 1979.

- Lyons, L. R., The field-aligned current versus electric potential relation and auroral electrodynamics, in *Physics of Auroral Arc Formation*, *Geophys. Monogr. Ser.*, 25, edited by S.-I. Akasofu, and J. R. Kan, p. 252, Amer. Geophys. Union, Washington, D.C., 1981.
- Lyons, L. R., and J. C. Samson, Formation of the stable auroral arc that intensifies at substorm onset, *Geophys. Res. Lett.*, 19, 2171, 1992.
- Lyons, L. R., A new theory for magnetospheric substorms, *J. Geophys. Res.*, 100, 19069, 1995.
- Lysak, R. L., and C. W. Carlson, The effect of microscopic turbulence on magnetosphere-ionosphere coupling, *Geophys. Res. Lett.*, 8, 269, 1981.
- Lysak, R. L., Theory of auroral zone PiB pulsation spectra, *J. Geophys. Res.*, 93, 5942, 1988.
- Lysak, R. L., Electrodynamic coupling of the magnetosphere and ionosphere, *Space Sci. Rev.*, 52, 33, 1990.
- Lysak, R. L., Feedback instability of the ionospheric resonant cavity, *J. Geophys. Res.*, 96, 1553, 1991.
- Maltsev, Y. P., and W. B. Lyatsky, Surface waves on the plasma sheet boundary, *Planet. Space Sci.*, 32, 1547, 1984.
- Maynard, N. C., D. S. Evans, B. Maehlum, and A. Egeland, Auroral vector electric field and particle comparisons 1. Premidnight convection topology, *J. Geophys. Res.*, 82, 2227, 1977.
- McIlwain C. E., Direct measurement of particles producing visible auroras, *J. Geophys. Res.*, 65, 2727, 1960.

- Mishin, E. V., and M. Förster, 'Alfvénic shocks' and low-altitude auroral acceleration, *Geophys. Res. Lett.*, *22*, 1745, 1995.
- Mitchell, D. G., M. J. Engebretson, D. J. Williams, C. A. Cattell, and R. Lundin, Pc5 pulsations in the outer dawn magnetosphere seen by ISEE 1 and 2, *J. Geophys. Res.*, *95*, 967, 1990.
- Miura, A., and P. L. Pritchett, Nonlocal stability analysis of the MHD Kelvin-Helmholtz instability in a compressible plasma, *J. Geophys. Res.*, *87*, 7431, 1982.
- Miura, A., Anomalous transport by magnetohydrodynamic Kelvin-Helmholtz instabilities in the solar wind-magnetosphere interaction, *J. Geophys. Res.*, *89*, 801, 1984.
- Miura, A., S. Ohtani, and T. Tamao, Ballooning instability and structure of diamagnetic hydromagnetic waves in a model magnetosphere, *J. Geophys. Res.*, *94*, 15231, 1989.
- Miura, A., and J. R. Kan, Line-tying effects on the Kelvin-Helmholtz instability, *Geophys. Res. Lett.*, *19*, 1611, 1992.
- Miura, A., Stabilization of the Kelvin-Helmholtz instability by the transverse magnetic field in the magnetosphere-ionosphere coupling system, *Geophys. Res. Lett.*, *23*, 761, 1996.
- Mozer, F. S., C. W. Carlson, M. K. Hudson, R. B. Torbert, B. Parady, J. Yatteau, and M. C. Kelley, Observations of paired electrostatic shocks in the polar magnetosphere, *Phys. Rev. Lett.*, *38*, 292, 1977.
- Mozer, F. S., ISEE-1 observations of electrostatic shocks on auroral zone field lines between 2.5 and 7 Earth radii, *Geophys. Res. Lett.*, *8*, 823, 1981.

- Murphree, J. S., and M. L. Johnson, Clues to plasma processes based on Freja UV observations, *Adv. Space Res.*, *18*, (8)95, 1996.
- Ohtani, S.-I., S. Kokubun, and C. T. Russel, Radial expansion of the tail current disruption during substorms: A new approach to the substorm onset region, *J. Geophys. Res.*, *97*, 3129, 1992.
- Ohtani, S., and T. Tamao, Does the ballooning instability trigger substorms in the near-Earth magnetotail?, *J. Geophys. Res.*, *98*, 19369, 1993.
- Parker, E. N., Interaction of the solar wind with the geomagnetic field, *Phys. Fluids*, *1*, 171, 1958.
- Pedlosky, J., *Geophysical Fluid Dynamics*, 710 p., Springer-Verlag, New York, 1987.
- Potemra, T. A., and L. G. Blomberg, A survey of Pc5 pulsations in the dayside high-latitude regions observed by Viking, *J. Geophys. Res.*, *101*, 24801, 1996.
- Rankin, R., B. G. Harrold, J. C. Samson, and P. Frycz, The nonlinear evolution of field line resonances in the Earth's magnetosphere, *J. Geophys. Res.*, *98*, 5839, 1993a.
- Rankin, R., J. C. Samson, and P. Frycz, Simulations of driven field line resonances in the Earth's magnetosphere, *J. Geophys. Res.*, *98*, 21341, 1993b.
- Rankin, R., P. Frycz, V. T. Tikhonchuk, and J. C. Samson, Nonlinear standing shear Alfvén waves in the Earth's magnetosphere, *J. Geophys. Res.*, *99*, 21291, 1994.
- Rankin, R., P. Frycz, V. T. Tikhonchuk, and J. C. Samson, Ponderomotive saturation of magnetospheric field line resonances, *Geophys. Res. Lett.*, *22*, 1741, 1995.
- Rankin, R., P. Frycz, J. C. Samson, and V. T. Tikhonchuk, Shear flow vortices in magnetospheric plasmas, *Phys. Plasmas*, *4*, 829, 1997.

- Reiff, P. H., R. W. Spiro, and T. W. Hill, Dependence of polar cap potential drop on interplanetary parameters, *J. Geophys. Res.*, *86*, 7639, 1981.
- Robinson, R. M., and R. R. Vondrak, Electrodynamic properties of auroral surges, *J. Geophys. Res.*, *95*, 7819, 1990.
- Rostoker, G., S.-I. Akasofu, J. Foster, R. A. Greenwald, Y. Kamide, K. Kawasaki, A. T. Y. Lui, R. L. McPherron, and C. T. Russell, Magnetospheric substorms - definition and signatures, *J. Geophys. Res.*, *85*, 1663, 1980.
- Rostoker, G., Triggering of expansive phase intensifications of magnetospheric substorms by northward turning of the interplanetary magnetic field, *J. Geophys. Res.*, *88*, 6981, 1983.
- Rostoker, G., and T. Eastman, A boundary layer model for magnetospheric substorms, *J. Geophys. Res.*, *92*, 12187, 1987.
- Rostoker, G., Phenomenology and physics of magnetospheric substorms, *J. Geophys. Res.*, *101*, 12955, 1996.
- Rothwell, P. L., M. B. Silevitch, and L. P. Block, A model for the propagation of the westward traveling surge, *J. Geophys. Res.*, *89*, 8941, 1984.
- Roux, A., S. Perraut, P. Robert, A. Morane, A. Pedersen, A. Korth, G. Kremser, B. Aparicio, D. Rodgers, and R. Pellinen, Plasma sheet instability related to the westward traveling surge, *J. Geophys. Res.*, *96*, 17697, 1991.
- Ruohoniemi, J. M., R. A. Greenwald, and K. B. Baker, HF radar observations of Pc5 field line resonances in the midnight/early morning MLT sector, *J. Geophys. Res.*, *96*, 15697, 1991.
- Russell, C. T., and M. M. Hoppe, Upstream waves and particles, *Space Sci. Rev.*,

- 34, 155, 1983.
- Samson, J. C., B. G. Harrold, J. M. Ruohoniemi, R. A. Greenwald, and A. D. M. Walker, Field line resonances associated with MHD waveguides in the magnetosphere, *Geophys. Res. Lett.*, 19, 441, 1992a.
- Samson, J. C., L. R. Lyons, P. T. Newell, F. Creutzberg, and B. Xu, Proton aurora and substorm intensifications, *Geophys. Res. Lett.*, 19, 2167, 1992b.
- Samson, J. C., L. L. Cogger, and Q. Pao, Observations of field line resonances, auroral arcs, and auroral vortex structures, *J. Geophys. Res.*, 101, 17373, 1996a.
- Samson, J. C., A. K. MacAulay, R. Rankin, P. Frycz, I. Voronkov, and L. L. Cogger, Substorm intensifications and resistive shear flow - ballooning instabilities in the near-Earth magnetotail. in *Proceedings of the Third International Conference on Substorms (ICS-3)*, 399, ESA SP-389, Versailles, 1996b.
- Samson, J.C., R. Rankin, and I. Voronkov, Field line resonances, auroral arcs, and substorm intensifications, in *Encounter Between Global Observations and Models in the ISTP Era*, Amer. Geophys. Union, Washington, in press, (accepted July 20, 1997), 1998.
- Sandholt, P. E., and A. Egeland, *Electromagnetic Coupling in the Polar Clefts and Caps*, Dordrecht, Kluwer, 1989.
- Schindler, K., A theory of the substorm mechanism, *J. Geophys. Res.*, 79, 2803, 1974.
- Sergeev, V. A., N. P. Dmitrieva, and E. S. Barkova, Triggering of substorm expansion by the IMF directional discontinuities: time delay analysis, *Planet. Space Sci.*, 34, 1109, 1986.

- Sergeev, V. A., D. G. Mitchell, C. T. Russell, and D. J. Williams, Structure of the tail plasma/current sheet at  $\sim 11 R_E$  and its changes in the course of a substorm, *J. Geophys. Res.*, **98**, 17345, 1993.
- Smith, P. N., and R. A. Hoffman, Ring current particle distributions during the magnetic storms of December 16-18, 1971, *J. Geophys. Res.*, **78**, 4731, 1973.
- Southwood, D. J., Some features of field line resonances in the magnetosphere, *Planet. Space Sci.*, **22**, 483, 1974.
- Southwood, D. J., and W. J. Hughes, Theory of hydromagnetic waves in the magnetosphere, *Space Sci. Rev.*, **35**, 301, 1983.
- Steen, Å., and P. N. Collis, High time-resolution imaging of auroral arc deformation at substorm onset, *Planet. Space Sci.*, **36**, 715, 1988.
- Størmer, C., Résultats des mesures photogrammétriques des aurores boreales observées dans la Norvège méridional de 1911 à 1922, *Geofys. Publikasjoner*, **4**, 5, 1927.
- Streltsov, A., and W. Lotko, The fine structure of dispersive, nonradiative field line resonance layers, *J. Geophys. Res.*, **101**, 5343, 1996.
- Streltsov, A. V., and W. Lotko, Dispersive, nonradiative field line resonances in a dipolar magnetic field geometry, *J. Geophys. Res.*, **102**, 27121, 1997.
- Sundaram, A. K., and D. H. Fairfield, Localized tearing modes in the magnetotail driven by curvature effects, *J. Geophys. Res.*, **100**, 3563, 1995.
- Sundaram, A. K., and D. H. Fairfield, Stability of resistive MHD tearing and ballooning modes in the tail current sheet, *J. Geophys. Res.*, **102**, 19913, 1997.
- Tajima, T., W. Horton, P. J. Morrison, J. Schutkeker, T. Kamimura, K. Mima,

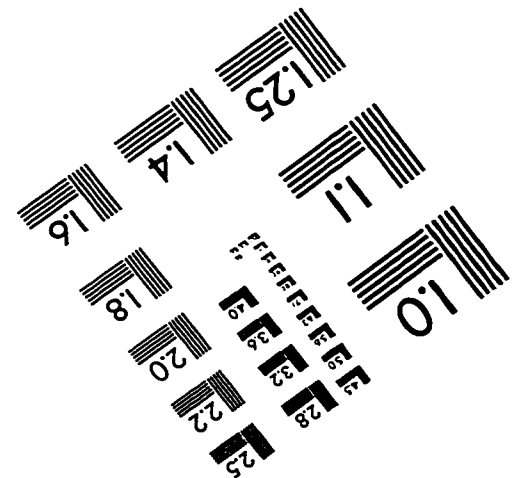
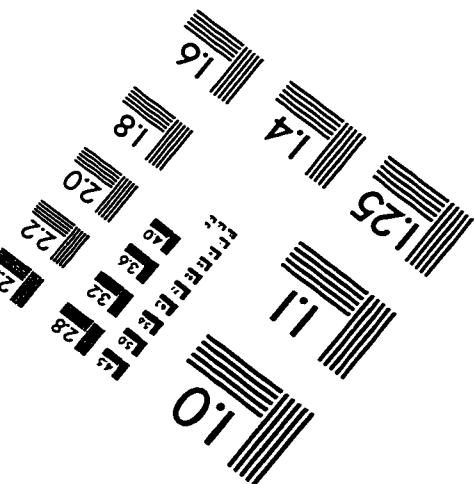
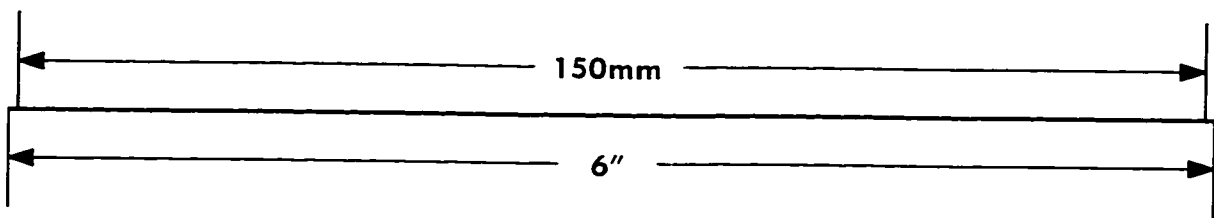
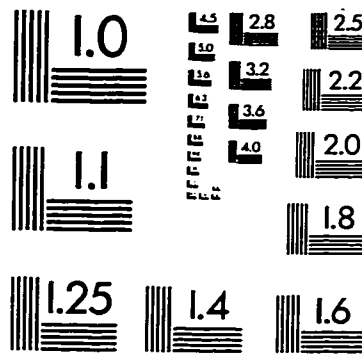
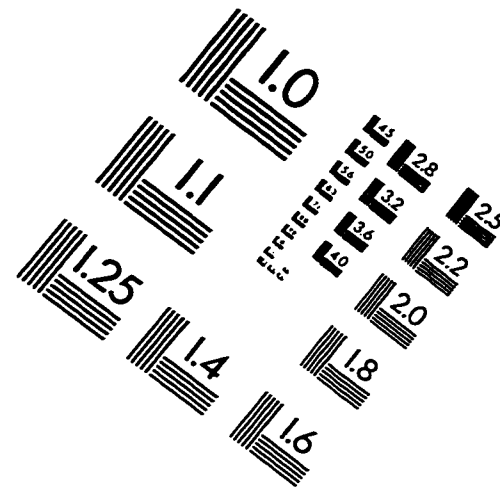
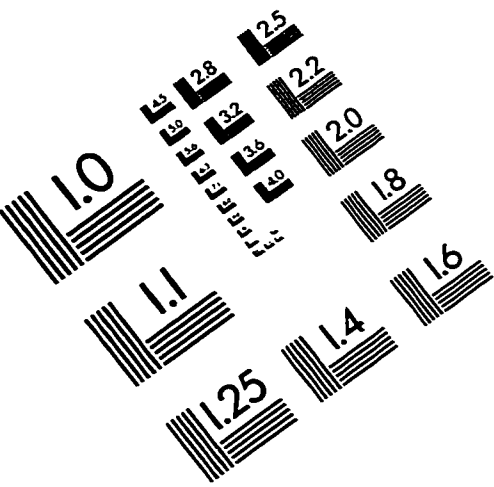
- and Y. Abe, Instabilities and vortex dynamics in shear flow of magnetized plasmas, *Phys. Fluids B*, **3**, 938, 1991.
- Thomas, V. A., and D. Winske, Kinetic simulations of the Kelvin-Helmholtz instability at the magnetopause, *J. Geophys. Res.*, **98**, 11425, 1993.
- Thomas, V. A., Three-dimensional kinetic simulation of the Kelvin-Helmholtz instability, *J. Geophys. Res.*, **100**, 19429, 1995.
- Tian, M., T. K. Yeoman, M. Lester, and T. B. Jones, Statistics of Pc 5 pulsation events observed by SABRE, *Planet. Space Sci.*, **39**, 1239, 1991.
- Tikhonchuk, V. T., R. Rankin, P. Frycz,, and J. C. Samson, Nonlinear dynamics of standing shear Alfvén waves, *Phys. Plasmas*, **2**, 501, 1995.
- Tiwari, M. S., and G. Rostoker, Field-aligned currents and auroral acceleration by non-linear MHD waves, *Planet. Space Sci.*, **32**, 1497, 1984.
- Trakhtengertz, V. Yu., and A. Ya. Feldstein, Quite auroral arcs: Ionosphere effect of magnetospheric convection stratification, *Planet. Space Sci.*, **32**, 127, 1984.
- Trakhtengertz, V. Yu., and A. Ya. Feldstein, Turbulent Alfvén boundary layer in the polar ionosphere 1. Excitation conditions and energetics, *J. Geophys. Res.*, **96**, 19363, 1991.
- Trondsen, T. S., and L. L. Cogger, High-resolution television observations of black aurora, *J. Geophys. Res.*, **102**, 363, 1997.
- Trondsen, T. S., L. L. Cogger, and J. C. Samson, Asymmetric multiple auroral arcs and inertial Alfvén waves, *Geophys. Res. Lett.*, **24**, 2945, 1997.
- Trondsen, T. S., and L. L. Cogger, A survey of small-scale spatially periodic distortions of auroral forms, *J. Geophys. Res.*, **103**, 1998, in press.



- Tsyganenko, N. A., Effects of the solar wind conditions on the global magnetospheric configuration as deduced from data-based field models. in *Proceedings of the third international conference on substorms (ICS-3)*, 181, ESA SP-389, Versailles, 1996.
- Verzariu, P., Reflection and refraction of hydromagnetic waves at the magnetopause, *Planet. Space Sci.*, *21*, 2213, 1973.
- Vetoulis, G., and L. Chen, Global structures of Alfvén-ballooning modes in magnetospheric plasmas, *Geophys. Res. Lett.*, *21*, 2091, 1994.
- Viñas, A. F., and T. R. Madden, Shear flow-ballooning instability as a possible mechanism for hydromagnetic fluctuations, *J. Geophys. Res.*, *91*, 1519, 1986.
- Voronkov, I., R. Rankin, P. Frycz, V. T. Tikhonchuk, and J. C. Samson, Coupling of shear flow and pressure gradient instabilities. *J. Geophys. Res.*, *102*, 9639, 1997a.
- Voronkov, I., R. Rankin, V. T. Tikhonchuk, and J. C. Samson, Nonlinear shear Alfvén resonances in a dipolar magnetic field. *J. Geophys. Res.*, *102*, 27137, 1997b.
- Walker, A. D. M., and R. A. Greenwald, Statistics of occurrence of hydromagnetic oscillations in the Pc5 range observed by the STARE auroral radar, *Planet. Space Sci.*, *29*, 293, 1981.
- Wright, A. N., Dispersion and wave coupling in homogeneous MHD waveguides, *J. Geophys. Res.*, *99*, 159, 1994.
- Xu, B.-L., J. C. Samson, W. W. Liu, F. Creutzberg, and T. J. Hughes, Observations of optical aurora modulated by resonant Alfvén waves. *J. Geophys. Res.*, *98*, 11531, 1993.
- Zmuda, A. J., and J. C. Armstrong, The diurnal variations of the region with vector magnetic field changes associated with field-aligned currents. *J. Geophys. Res.*, *79*,

2501, 1974.

# IMAGE EVALUATION TEST TARGET (QA-3)



APPLIED IMAGE, Inc  
1653 East Main Street  
Rochester, NY 14609 USA  
Phone: 716/482-0300  
Fax: 716/288-5989

© 1993, Applied Image, Inc., All Rights Reserved